Title

Probing Cosmic Dawn: Observations of High-redshift Galaxies UsingGravitational Lensing

Author

Strait, Victoria

Publication Date

2021

Probing Cosmic Dawn: Observations of High-redshift Galaxies Using Gravitational Lensing

By

VICTORIA BELLINGER STRAIT

DISSERTATION

Submitted in partial satisfaction of the requirements for the degree of

DOCTOR OF PHILOSOPHY

in

Physics

in the

OFFICE OF GRADUATE STUDIES

of the

UNIVERSITY OF CALIFORNIA

DAVIS

Approved:

Professor Maruša Bradač, Chair

Professor Tucker Jones

Professor Andrew Wetzel

Committee in Charge

2021

Contents

List of Figures

List of Tables

ABSTRACT OF THE DISSERTATION

Probing Cosmic Dawn: Observations of High-redshift Galaxies Using Gravitational Lensing

The *Epoch of Reionization* or *Cosmic Dawn* is the period of time between the Dark Ages, when the universe was mainly comprised of neutral hydrogen and there were few sources of light, and around $z \sim 6$ (or ~ 1 billion years after the big bang) by which time the universe's hydrogen had been completely reionized. This period in time in which the first sources of light emerged was one of the most significant changes that the universe experienced: not only for the intergalactic medium, but also for galaxy and structure formation. Despite its importance and impact on the history of the universe, today, the timing and process of reionization remain largely unconstrained. There are several barriers to placing constraints on the Epoch of Reionization. One of the largest ones is that neutral hydrogen precludes the observation of the most accessible emission line, Lyα, making it difficult to observe past $z \sim 6$. In addition, the faintest galaxies, which are likely the main drivers of reionization, are far beyond the detection limit of current telescopes in blank fields.

Gravitational lensing has a long history of aiding in the discovery of high-redshift galaxies by magnifying them to a brighter apparent magnitude, making them observable with limited telescope time. In this dissertation, I use gravitational lensing to probe some of the faintest galaxies ever observed during the Epoch of Reionization. I begin in Chapter 2 by detailing a lens model of a well-studied galaxy cluster, Abell 370. In order to model its mass and magnification distribution with the ultimate goal of correcting high-redshift galaxies residing behind the cluster for magnification, I use *Hubble Space Telescope* imaging of singly and multiply imaged galaxies as constraints, and a free-form lens modeling code called Strong and Weak Lensing United. I compare my results to other lens models of the cluster and discuss the systematic differences. This work is an important contribution to the high redshift galaxy community, as it adds a lens model which uniquely does not assume that light traces mass, and solves for a best fit model non-parametrically.

In Chapters 3 and 4, I focus on the high-redshift galaxy population behind a different set of galaxy clusters: the 41 clusters from the Reionization Lensing Cluster Survey (RELICS).

In Chapter 3, I discuss the highest-redshift candidates from the Lyman-break selected sample, all at or above $z \sim 8$. In Chapter 4, I detail the entire $z \geq 5.5$ sample. An important component in both chapters is the use of imaging from the *Spitzer Space Telescope* to constrain the rest-frame optical spectrum of the galaxy candidates. I go into depth using two methods of spectral energy distribution fitting and discuss systematic uncertainties. In both chapters, I discuss several exciting candidates for follow-up with current and future telescopes. These include a spatially resolved $z \sim 10$ arc, a galaxy with a likely evolved stellar population at $z \sim 8$, and a galaxy likely containing extreme [OIII]+Hβ emission.

In Chapter 5, I discuss the observation and discovery of an extreme Lyman-α emitting galaxy at $z \sim 7$, also from the RELICS sample, named the Dichromatic Primeval Galaxy at $z \sim 7$ (DP7). In this Chapter, I raise several questions about DP7's physical properties and highlight it as an exciting galaxy for followup with *JWST* and ALMA. Along with strong (> 200Å rest-frame equivalent width) and spatially-resolved Lyman-α, DP7 shows signs of a red UV β slope (~ -1) and possibly multiple components in the UV.

In Chapter 6, I summarize: with imaging from *Hubble Space Telescope* and *Spitzer Space Telescope* and spectroscopy from the Keck Telescopes to study lensed galaxies at high-redshift, I have been able to address questions about the Epoch of Reionization through observations of galaxies, focusing mainly on constraining properties of galaxies at the EoR, with an eye towards constraining their effect on the intergalactic medium with future telescopes.

ACKNOWLEDGMENTS

The first person that I have to acknowledge, and one of the two people who quite literally needed to exist for this thesis to have happened, is my dad. Thanks, dad, for always being interested in what I was learning, for having infectious curiosity, humility, try-hard and stoke. Equally so, thank you to my mom, whose unconditional love I'm convinced cannot be matched. Thank you also for teaching me important qualities such as resilience, grit, and tenacity; no one makes it through a PhD thesis without those. I owe endless thanks to my little sister Sarah, who has never let the fact that I am the older sister get in the way of her being the wiser one. Thanks, Sarah, for reminding me to rest and to eat, and for being an excellent 2-years-younger-than-me role model. Thanks to my little brother, who has, in his own quiet way, been the best supportive cheerleader I could have asked for. Thanks, Seth, for the funny gifts and time spent on breaks over the years. I have a large extended family, but one person sticks out as particularly important and supportive over the last 6 years: Aunt Mary. Thank you, Aunt Mary, for all of your motherly support, advice, and for modeling independence and vulnerability.

Thank you to Jordan, who during the course of the last two years of my PhD went from acquaintance to fiancee, for being a calming and supportive presence. My quality of life, both in and out of grad school, changed for the better when I met you. Thank you to countless friends that I made at Davis: Nastya, Jenna, Ariadna, Chase, Jessie, Azalee, Cameron, Rose, Imran, James, Adam, Chris, Morgane, Isaiah, Patty, Pratik, Alex, Antonio, and so many others. The best memories I have from grad school are climbing, playing, biking, eating, and laughing, with you all.

"Thank you" isn't enough for my two main mentors: my official PhD advisor, Maruša Bradač, and my "other" PhD advisor, Brian Lemaux. Thank you, Maruša for... so many things. You modeled how to be a different type of human than I had ever met: someone who takes enough time to play and be happy while still being generally amazing and very successful. You single-handedly increased my self-confidence by a factor of 100 since starting grad school, and believed in me much, much more than I believed in myself most of the time. Thank you for teaching me all about high redshift galaxies, and also about how to exist in a world I was totally unfamiliar with, for answering all of my questions about what to wear at a conference, how to navigate academic relationships, how to give a talk, how to read and write a paper, how to speak up in a conversation, how to be a kind and respected leader. I learned a lot from watching you. And thank you to Brian, who served as Maruša's foil in the story of my PhD. Thank you for spending way too much time with me on the nitty-gritty details of SED fitting. Thank you for all of the conversations that have taught me so much of what I now take for granted as knowledge that I have, and for the creative times we have had together writing papers and proposals. Thank you for your stoke, enthusiasm, emotional support, vulnerability, and kind words, which helped keep me afloat during difficult times. Thank you for teaching me all about observing. Thank you for being really really excited about skiing with me. Maruša and Brian, I owe most of my success in grad school to you.

There have been so many other mentors worth mentioning: Andrew Wetzel, who wrote recommendation letters, consulted with me on projects, and served on my thesis committee, Dan Coe, who became a major mentor in the last few years and from whom I have learned a lot about science and writing, Tucker Jones, Chris Fassnacht, Lori Lubin, and all of the other faculty at UC Davis who have been wonderful community members and mentors at different times; thank you. The postdocs senior grad students at UC Davis were essential to my success, and as is so often the case, served as my cooler and smarter older academic siblings: Sam Schmidt, Debora Pelliccia, Austin Hoag, Sarah Loebman, Adam Tomczak, Ryan Sanders, thank you for your science mentorship and your friendship.

Thank you to so many teachers I've had throughout the years. Ones that stick out are Ms. Ashley Holmes in middle school, Dr. Kevin Sandusky in high school, and Drs. D'Amato, Baker, and Moffett in college. Thanks to folks who made my first undergraduate research experiences possible, Martin Snow, Rena Zieve, Tony Tyson, Sam Schmidt. Thanks to all of my lovely collaborators, many of whom I have never met in person. Thanks in general to the UCD astro group: for pizza lunches, roof beers, and fun times in the office. And thanks to my dog, Callie, who has sat quietly next to me during many of the hours I spent working on this dissertation.

Chapter 1

An Introduction to Galaxies at Cosmic Dawn

1.1 The Epoch of Reionization and Open Questions

Some of the most fundamental questions that we as humans are asked to wrestle with straddle the line of science and philosophy, and begin with the closest thing to the beginning of time that we can wrap our minds around: the Big Bang. Questions like How did we get here? Is there other life somewhere else? Why is anything the way that it is? It is not a coincidence that astronomy has been a large part of not only science, but religion and philosophy for centuries. The philosophical appeal is the reason that so many young scientists, including myself, are drawn to the field. While the more philosophical questions cannot be answered within the confines of observational astrophysics and cosmology, the scientific fields provide a well-defined basis to think about the history of the universe in a physical sense, and this framework has helped at least one human relate to the meaning of time, space, and existence.

1.1.1 A Brief History of Time

A brief version of our current theoretical understanding of the universe is as follows: the first few minutes in the life of the universe consisted of an extremely fast and energetic expansion of matter and radiation, eventually culminating in a hot soup of free electrons and atomic nuclei coupled to photons. Around 370,000 years later, the universe was cool enough for electrons and protons to bond, forming neutral hydrogen and allowing photons to stream freely as the universe became transparent for the first time. As this was the last time photons scattered before streaming out isotropically into space, its location is often referred to as the "surface of last scattering". We can still see the radiation left over from this event today as the Cosmic Microwave Background (CMB), our oldest observation of the universe.

Beginning at the last scattering, and extending for likely between 100-400 million years, the universe consisted of mainly neutral atoms and dark matter. As overdensities in the CMB converged into dense clumps, the first dark matter halos were formed. Within them, the first stars, and eventually galaxies, formed from neutral hydrogen and helium (and other trace elements). Over the next few hundred million years, the majority of the neutral hydrogen in the universe was (re-)ionized by radiation from the stars and galaxies. The questions this dissertation addresses begin when stars and galaxies began forming, and end when the reionization of the hydrogen in the universe was completed, during what we call *The Epoch of Reionization* or *Cosmic Dawn*.

1.1.2 Open Questions about the Epoch of Reionization

Although the Epoch of Reionization (EoR) was one of the universe's major phase changes, and the last major phase change of hydrogen, the timing and nature of the process of reionization are largely unconstrained. Questions include: When did reionization begin? What objects were mainly responsible for ionizing the intergalactic medium (IGM)? How patchy was the process? How did the first galaxies form and influence their immediate environments? Because reionization is closely tied to the nature of the first sources of light and early galaxy evolution, these high-level questions in turn depend on more detailed questions like What physics was involved in the production and escape of ionizing radiation from galaxies and active galactic nuclei (AGN) during the EoR? and What are the diversity of properties of high redshift galaxies?

The question of the precise timeline of reionization has been approached in several independent ways. The first observational evidence for reionization was by Gunn & Peterson (1965) who measured absorption troughs in high-z quasars, noting that even a small amount of neutral hydrogen along the line of sight has a large effect on the spectrum of their quasars. Later, Fan et al. (2006) measured this effect in quasars out to $z \sim 6$, where the

Gunn-Peterson trough saturates and the method is no longer a sensitive probe to reionization. Relatedly, there have been a few somewhat controversial analyses of Lyman-α (1216Å Lyα) damping wings of high-redshift quasars used as a probe for the high-redshift neutral hydrogen environment (e.g., Totani et al., 2016; Wang et al., 2020). A similar probe of the timeline of reionization is the Lyα emitter (LAE) fraction test (e.g., Hoag et al., 2019; Mason et al., 2019). Through an inference using cosmological simulations and observations of high-redshift Lyman break galaxies, one can use the fraction of observed LAEs to infer the neutral fraction past $z \sim 6$. Results from this test have shown that the universe is likely ∼88% neutral at $z \sim 7.5$ (Hoag et al., 2019), although other results have shown some disagreement (Jung et al., 2020).

Observations of polarization anisotropies in the CMB have also helped constrain the reionization timeline via the optical depth parameter, τ: Thomson scattering of CMB photons off of free electrons from hydrogen becoming ionized during reionization suppresses the anisotropies and allows for a measure of opacity. However, because this is a globally averaged signal integrated over the entire timeline of reionization and a model for reionization must be assumed to interpret it, it does not provide all of the constraints necessary for the timing of reionization. Planck Collaboration et al. (2016) suggested that due to the observed Thomson optical depth, an instantaneous reionization model would have to have occurred at a redshift of 7.8-8.8, depending on the model assumed (Planck Collaboration et al., 2016), which places a constraint on early star formation. This constraint is used in many models of the timeline of reionization, including Robertson et al. (2015) and Finkelstein et al. (2019).

The 21 cm line, the hyperfine transition of the 1s state of neutral hydrogen, is also a signal intimately tied to reionization as it is produced by neutral hydrogen. A detection during the course of this disseration from EDGES (Bowman et al., 2018) revealed an absorption that may be consistent with the 21 cm signal at $z \sim 17$; this places an upper limit on the beginning of reionization and suggests that there was star formation as early as $\sim$ 200Myr after the Big Bang. However, to explain the signal completely, there must be a steepening of the UV luminosity function at high redshifts (Mirocha et al., 2018), which is at odds with other observations. This detection is the first of its kind, and is far from accepted. There have been other, similar experiments to EDGES that have been unable to detect a signal, including the Precision Array for Probing the Epoch of Reionization (PAPER, Parsons et al., 2010), Low-Frequency Array (LOFAR, Patil et al., 2017), the Murchison Wide-Field Array (MWA, Beardsley et al., 2016), and the Giant Meterwave Radio Telescope (GMRT, Paciga et al., 2013). Future facilities including the Square Kilometer Array (SKA, Mellema et al., 2013) and Hydrogen Epoch of Reionization Array (HERA, DeBoer et al., 2017) promise to increase sensitivity and confirm or deny the EDGES detection, as well as fully map the 21cm tomography.

Lastly, the inferred ages of early galaxies can act as a probe for the beginning of reionization. The age for at least one galaxy observed at Cosmic Dawn ($z = 9.1096 \pm 0.0006$) has been shown to be > 275 Myr (Zheng et al., 2012; Bradač et al., 2014; Huang et al., 2016b; Hoag et al., 2018; Hashimoto et al., 2018). Since the age of the universe at $z \sim 9.1$ is only 540 Myr, this age estimate implies that stars would have had to start forming $\sim$250 Myr after the big bang. Evolved candidate high redshift galaxies have been found by several others as well (e.g., Tamura et al., 2019; Strait et al., 2020a; Bakx et al., 2020; Roberts-Borsani et al., 2020, including Chapter 3 of this Dissertation), and some were recently confirmed with various spectrographs (Laporte et al., 2021).

1.1.2.1 Sources of Reionizing Photons

The question of what objects are responsible for reionization has been hotly debated over the last decades; some studies claim that because AGN and bright galaxies are powerful enough to emit large numbers of ionizing photons, that they are likely significant drivers of reionization (e.g., Finkelstein et al., 2019). However, others have shown that the number density of AGN is too low at high-redshift for this to be possible, and argue that rather the small, faint galaxies at high redshift which come in high numbers are likely responsible (Robertson et al., 2015; Bouwens et al., 2016; Parsa et al., 2018).

Measurements at high-redshift are difficult due to the increasing effect of the IGM: as redshift increases, so does the amount of neutral hydrogen, which easily scatters the most accessible emission line, Lyα. While the consensus has seemingly settled on galaxies driving reionization, the answer will depend on precision statistical measurements of ionizing production and escape of these faint galaxies. Much of this work is being done on low redshift analogs, where data are easier to come by and the IGM is not an issue (e.g., Izotov et al., 2016b,a; Vanzella et al., 2016; Izotov et al., 2018b,a; Fletcher et al., 2019; Rivera-Thorsen et al., 2019; Tang et al., 2019; Wang et al., 2019; Chisholm et al., 2020; Izotov et al., 2021), with only a few at high-z (e.g., Matthee et al., 2017a; Sobral et al., 2018), until the *James Webb Space Telescope* (*JWST*) flies. With powerful high-z rest-frame optical capabilities, *JWST* is expected to provide more precise constraints on ionizing production (and to some degree escape) in the EoR.

While the process of reionization has been modeled in the past as smooth in simple simulations, it has come to be understood that the process is indeed patchy to some degree, due to the nature of ionizing sources existing in overdensities (Pentericci et al., 2014; Becker et al., 2015; Furlanetto et al., 2006; McQuinn et al., 2007; Weinberger et al., 2018; Endsley et al., 2020b). The question of exactly how patchy will depend on exact ionized bubble sizes at high-redshift. Bubble sizes have been constrained for some galaxies at high redshift (e.g., Matthee et al., 2018), but these studies are observationally biased towards the brightest, most powerful galaxies, and more observations of bubbles around faint, characteristic high-z galaxies' environments are needed to properly address this question.

This dissertation will discuss two valuable ways to gather information about galaxies at Cosmic Dawn: through a large number of imaging observations of galaxies at high-redshift, targeting galaxy cluster fields which act as natural cosmic telescopes that aid in the ability to observe faint, characteristic galaxies (Chapters 2, 3 and 4), and through a detailed case study of an interesting galaxy with spectroscopy (Chapter 5). I will introduce the idea of using gravitational lensing as a tool for high redshift galaxy discovery in Section 1.2. I will follow with sections describing galaxy discovery and measuring properties with imaging (Section 1.3) and spectroscopic followup (Section 1.4).

1.2 Cosmic Telescopes and Gravitational Lensing

The first major work presented in Chapter 2 focuses on the modeling and analysis of a gravitational lensing model of a massive galaxy cluster. Gravitational lensing, the natural property of the universe that describes the warping and magnification of the fabric of space-time near a massive object, has been used for decades to aid in the discovery of high redshift galaxies (e.g., Franx et al., 1997; Postman et al., 2012; Bouwens et al., 2014; Bradač et al., 2014; Ryan et al., 2014; Huang et al., 2016a; Merlin et al., 2016; Castellano et al., 2016a; Lotz et al., 2017; Di Criscienzo et al., 2017; Santini et al., 2017; Shipley et al., 2018; Bradač et al., 2019; Coe et al., 2019). As some of the most massive gravitationally-bound objects in the universe at $\sim 10^{14-15} M_{\odot}$, galaxy clusters serve as natural telescopes, allowing us to observe intrinsically faint objects that would, without magnification, be below the detection limit of current telescopes.

High-redshift galaxies exist in a *source plane*, defined by the distance to the source, and appear magnified and stretched to us in the *lens plane* of the galaxy cluster. In order to properly correct for the magnification factor of these high redshift galaxies, one must build a model of the mass and magnification of the galaxy cluster field. This is not a straightforward process, as most of the mass in a galaxy cluster exists in the form of "invisible" dark matter. These models are usually constrained using the locations and redshifts of strongly lensed galaxies, which are galaxies lying behind the cluster that appear more than once in the lens plane due to their position relative to the cluster. There are a variety of computational methods to find a best-fit model from a set of strong lensing constraints, including parameterized methods (e.g., Jullo & Kneib, 2009; Oguri, 2010; Zitrin et al., 2013) and "free-form" methods (e.g., Bradač et al., 2005, 2009; Diego et al., 2018). These types of models each have strengths and weaknesses: while parametric models always produce smooth distributions parameterized by some profile or combination of profiles of dark matter halos and smaller galaxy halos, they are limited to shapes their models allow. Bradač et al. (2005) pioneered the use of "non-parametric" or "free-form" models, and also included weakly lensed galaxies as constraints in a lens model for the first time. The code, which we describe in Chapter 2, is called Strong and Weak Lensing United (SWUnited), and uses a grid-based approach to find a best-fit mass and magnification distribution for a cluster, and can reconstruct arbitrary mass distributions free of assumptions (e.g., that light from galaxies traces mass, which in galaxy clusters is not necessarily the case). SWUnited also uses weak lensing to constrain the outer radii of clusters, unique to lens modeling codes. Because there are many systematic uncertainties associated with lens models, it is important to explore several methods and sets of assumptions when using lens models to correct for magnification. These uncertainties are now well-studied, as there have been many studies which investigate these systematic errors and assumptions, including Chapter 2 of this dissertation.

1.3 Measuring galaxy properties

The second and third major works in this dissertation detail the process of modeling the properties of high redshift galaxies with imaging data. Preceding this type of analysis, galaxies must first be discovered. The detection and study of high-z galaxies has exploded in the last two decades thanks to the *Hubble Space Telescope*. The field went from having only a handful of $z > 6$ galaxies confirmed in 2000 to now (in 2021) having hundreds confirmed, due in large part to the Wide Field Camera 3 on *Hubble*. Having a large sample of galaxies at our disposal is important for understanding the global and statistical properties of galaxies in the universe, as well as for selecting the most exciting candidates for more detailed follow-up.

1.3.1 High-redshift galaxy discovery

Discovery of high-redshift galaxies is generally done using multi-wavelength imaging. Compared to spectroscopy, imaging takes much less time and is in general, a more efficient way to get a cursory look at a field. Several surveys have used the *Lyman-break method* to search for high-z galaxies, pioneered by Steidel et al. (1996). In this method, one selects for high-z galaxies by looking for a combination of a characteristic break either at the Lyman limit (rest-frame 912Å) or at rest-frame 1216Å due to IGM opacity at high redshifts ($z \gtrsim 6$), and a blue UV β slope (~ -2), where β is defined as the slope of the UV continuum of a galaxy parameterized as $f_\lambda \propto \lambda^\beta$. Often, another class of objects are serendipitously selected with these criterion: brown dwarf stars. These objects, which for our purposes are considered contaminants, must be removed during a visual inspection.

Although the Lyman-break method is the main method for high-z galaxy discovery used throughout this dissertation, there are other methods of discovery. The narrow-band method to search for Lyα emitters has been used extensively to search for a boost in narrow-band imaging where Lyα resides (e.g., Nilsson et al., 2007; Cuby et al., 2007; Zheng et al., 2019). And the search for dusty galaxies, which are completely overlooked in the Lyman break method, is mostly carried out in the IR/sub-mm (see Casey et al., 2014 for a review).

1.3.2 SED Fitting

Chapters 3 and 4 of this dissertation detail the measurement of galaxy properties using imaging from the *Hubble Space Telescope* which operates in the UV and infrared (0.1150 to 2 μm) and the *Spitzer Space Telescope* which operates in the infrared (3.6-160μm, although only 3.6-4.5 μm have been recently operational). Together, these telescopes probe the rest-frame UV and optical wavelengths of $z \gtrsim 6$ galaxies' spectra. With just $\sim$7 bands of *HST* imaging and 2 bands of *Spitzer* imaging, we can constrain a galaxy's stellar mass, star formation rate (SFR), age, and sometimes dust, with spectral energy distribution (SED) fitting. SED fitting, in its most basic form, compares a library of galaxy templates calculated using stellar evolution models to multiwavelength imaging observations, and finds a distribution of parameters that best fit the data. In recent years, SED fitting methods have become more sophisticated, allowing for the inclusion of spectroscopic data, and using complex Bayesian techniques to constrain galaxy properties (e.g., BAGPIPES, Carnall et al., 2018).

The uncertainties on basic galaxy properties from SED fitting can be large for a single galaxy: for the deepest Hubble imaging (when combined with *Spitzer* to constrain the rest-optical), stellar mass can be constrained to $\sim$ 0.1 dex, and for moderate depth imaging, $\sim$ 0.5 dex at $z \gtrsim 6$, when considering only statistical uncertainties. However, there are several important systematic uncertainties which should be considered with SED fitting, including but not limited to star formation history, initial mass function, effects of dust and metallicity, and general astrophysical noise. These are discussed in detail in Chapters 3 and 4. Even so, SED fitting is an excellent tool to get an understanding of the properties of a population of galaxies as a whole and for selecting galaxies with potentially exciting stellar populations for more detailed observational followup.

One of the main goals of measuring properties with imaging is to be able to confidently select interesting and promising galaxies for further observation. Two interesting types of galaxies that can be selected for using imaging, that I focus on in this dissertation, are 1) galaxies with "evolved" stellar populations (evolved in this case meaning older than 200Myr, since the age of the universe at $z \sim 6$ is $\lesssim 1$ Gyr) and 2) galaxies with extreme nebular emission, signifying intense star formation. The former is in search of more evidence that stars formed early in the universe, and the latter is in search of galaxies with potential for high ionization output and possibly large escape fracions. Both can be identified using imaging and SED fitting, as both types of galaxies contain features that are strong enough to affect a medium- or narrow-band image. The signature of a stellar population with an evolved component is the Balmer/4000Å break, where light from old stars builds up around 4000Å rest-frame. This can be seen in $z \gtrsim 6$ galaxies with an excess of flux in *Spitzer* 3.6μm and 4.5μm imaging bands. The signature of an extreme line emitter is also seen as an excess in *Spitzer* imaging bands, although the nebular lines generally only contaminate one band or the other, depending on the galaxy's precise redshift. By selecting for galaxies with *Spitzer* colors of a certain magnitude, we can find the most exciting candidates for follow-up.

1.4 Follow-up with Spectroscopy

While having a general sense of the statistical properties of a population of galaxies is helpful, it is mainly 1) a statistical tool and/or 2) a tool for identifying interesting galaxies for more detailed observations and study. In order to know a galaxy's precise redshift, detection of part of the galaxy's spectrum is needed. At high redshift, this is usually in the form of an emission line. The most accessible emission line for $z \gtrsim 6$ galaxies is the Lyα 1216Å $n = 2 \rightarrow 1$ hydrogen transition. Lyα, when seen, is often very strong in emission; for this reason, Lyα has been used widely for spectroscopic confirmation of galaxies' redshifts (e.g., Pentericci et al., 2018; Hoag et al., 2019; Jung et al., 2020). However, because the IGM becomes increasingly neutral at higher redshifts and Lyα photons scatter easily off of neutral hydrogren atoms, the visibility of Lyα drops considerably at $z \gtrsim 6$. While this fact has been taken advantage of to constrain the neutral fraction of the universe at various redshifts (e.g., Hoag et al., 2018), it hinders the ability to use Lyα to measure galaxies' redshifts at $z \gtrsim 6$. In the case that Lyα cannot serve to confirm redshift, other emission lines can be used, including the rest-frame UV CIII] 1907,1909Å doublet with near-IR spectroscopy, and the [CII]158μm and [OIII]88μm fine structure lines in radio wavelengths. When the *James Webb Space Telescope* launches, many more lines in the rest-frame optical will be available for redshift confirmation.

In addition to redshift confirmation, emission lines are used to do detailed and illuminating science on galaxies, including precise stellar population studies, and studies of ionizing bubble sizes, and kinematics (Huang et al., 2016b; Matthee et al., 2017a,b, 2018, 2019, 2020; Sobral et al., 2015; Sobral & Matthee, 2019). When the rest-frame optical spectrum of high redshift galaxies is observable with *JWST*, more will be possible, including precise constraints on metallicity, ionization parameters, escape fractions and ionizing production of galaxies.

1.5 This disseration

This dissertation focuses on using gravitational lensing to search for high-z galaxies, using SED fitting to derive their properties, and selecting the most exciting candidates for more detailed follow-up with existing and future telescopes, including Keck, *JWST*, and ALMA. Chapter 2 is from a paper published in 2018 detailing the process of modelling a galaxy cluster's mass and magnification (Strait et al., 2018), for the purpose of more accurately modeling the intrinsic properties of the high-z galaxies behind the cluster. The cluster discussed is Abell370, one of the most famous and longest-known galaxy clusters, and a part of the Hubble Frontier Fields survey. This survey is marked by its incredible depth of imaging and has allowed for many exciting discoveries.

The third and fourth chapters focus on constraining properties of galaxies from another survey using gravitational lensing, the Reionization Lensing Cluster Survey (RELICS). RELICS took a different approach than HFF; instead of observing extremely deep exposures on a few clusters, RELICS opts for moderate HST imaging of 41 clusters. In Chapter 3, I highlight 8 exciting galaxies for follow-up that have likely redshifts above $z \sim 8$, several of which show strong evidence for evolved stellar populations (Strait et al., 2020b). In Chapter 4, I detail the data reduction and SED fitting process for the entire RELICS sample, which includes over 300 galaxies at $z \geq 5.5$ with *HST* and *Spitzer* imaging. I discuss the properties of the sample as a whole, and highlight more exciting galaxies for follow-up, including a potential extreme line emitter.

In Chapter 5, I discuss a galaxy that came out of the RELICS sample and was observed with Keck/LRIS to have an extreme Lyα equivalent width (Pelliccia et al., 2020). This galaxy, the Dichromatic Primeval Galaxy at $z \sim 7$, was found to have a much more extreme emission than other galaxies at its epoch. I explore the possible physics of the emission and the implications of the ionizing source in DP7. In Chapter 6, I summarize and discuss my path forward.

Chapter 2

The Mass and Light of Galaxy Cluster Abell370

This chapter is an adapted version of the article titled *Mass and Light of Abell370: A Strong and Weak Lensing Analysis* which was published in Volume 868 of the Astrophysical Journal Letters (Strait et al., 2018).

We present a new gravitational lens model of the Hubble Frontier Fields cluster Abell 370 ($z = 0.375$) using imaging and spectroscopy from *Hubble Space Telescope* and ground-based spectroscopy. We combine constraints from a catalog of 909 weakly lensed galaxies and 39 multiply-imaged sources comprised of 114 multiple images, including a system of multiply-imaged candidates at $z = 7.84 \pm 0.02$, to obtain a best-fit mass distribution using the cluster lens modeling code Strong and Weak Lensing United. As the only analysis of A370 using strong and weak lensing constraints from Hubble Frontier Fields data, our method provides an independent check of assumptions on the mass distribution used in other methods. Convergence, shear, and magnification maps are made publicly available through the HFF website[1]. We find that the model we produce is similar to models produced by other groups, with some exceptions due to the differences in lensing code methodology. In an effort to study how our total projected mass distribution traces light, we measure the stellar mass density distribution using Spitzer/Infrared Array Camera imaging. Comparing our total mass density to our stellar mass density in a radius of 0.3 Mpc, we find a mean

---

[1] http://www.stsci.edu/hst/campaigns/frontier-fields

projected stellar to total mass ratio of $\langle f* \rangle = 0.011 \pm 0.003$ (stat.) using the diet Salpeter initial mass function. This value is in general agreement with independent measurements of $\langle f* \rangle$ in clusters of similar total mass and redshift.

2.1 Introduction

Cluster lens modeling has been used for decades as a tool to retrieve intrinsic properties of lensed sources for various types of scientific study. For example, investigation into properties of high redshift ($z > 6$) galaxies plays an essential role in understanding early galaxy evolution and the reionization of the universe. By measuring the number counts of high-redshift sources as a function of magnitude, we can obtain the ultraviolet luminosity function (UV LF), which allows us to infer properties such as star formation rate density, an essential piece to understanding the role that galaxies played in the reionization of the universe (e.g., Schmidt et al., 2014; Finkelstein et al., 2015; Mason et al., 2015; Robertson et al., 2015; Castellano et al., 2016b; Livermore et al., 2017; Bouwens et al., 2017; Ishigaki et al., 2018). At lower redshifts ($z = 0.7 - 2.3$), it is possible to measure spatially resolved kinematics and chemical abundances for the brightest sources (e.g., Christensen et al., 2012; Jones et al., 2015; Wang et al., 2015; Vulcani et al., 2016; Leethochawalit et al., 2016; Mason et al., 2017; Girard et al., 2018; Paterno-Mahler et al., 2018). Probing the faint end of both of these samples is challenging with the detection limits associated with blank fields. Using the gravitational lensing power of massive galaxy clusters, fainter sources can be studied in greater detail. To infer many of these sources' intrinsic properties (e.g., star formation rate and stellar mass), magnification maps are needed. Using strongly lensed sources and weakly lensed galaxies as constraints, lens models produce magnification and mass density maps.

Abell 370 ($z = 0.375$, A370 hereafter) was the first massive galaxy cluster observed for the purposes of gravitational lensing, initially alluded to by Lynds & Petrosian (1986) with follow-up by Lynds & Petrosian (1989). The cluster was also studied in depth by Soucail (1987); Hammer & Rigaut (1989) because of the giant luminous arc in the south, which led to the first lens model of A370 by Hammer (1987). Richard et al. (2010) provided one of the first strong lensing models of A370 which used data from HST imaging campaigns of the cluster, and weak lensing analyses followed soon after (Umetsu et al., 2011; Medezinski et al., 2011).

Since then, deeper imaging data have been taken of A370 by the Hubble Frontier Fields program (HFF: PI Lotz #13495, Lotz et al., 2017), an exploration of six massive galaxy clusters selected to be among the strongest lenses observed to date. Spectroscopic campaigns such as the Grism Lens-Amplified Survey from Space (GLASS) (Schmidt et al., 2014; Treu et al., 2015) and the Multi-Unit Spectroscopic Explorer Guaranteed Time Observations (MUSE GTO, Lagattuta et al., 2017) have obtained spectroscopic redshifts for nearly all of the strongly lensed systems discovered by HFF data. In this work we use 37 spectroscopically confirmed strongly lensed background galaxies and 2 with robust photometric redshifts, totalling 39 systems, as constraints for our lens model (see Section 2.3.3 for details). It has been shown by e.g., Johnson & Sharon (2016) that the most important parameter in constraining cluster lens models is the fraction of high quality (i.e. spectroscopically confirmed) multiply imaged systems to total number of systems. The 37 spectroscopically confirmed strongly lensed systems out of a total 39 combined with high quality weak lensing data in A370 has led to some of the most robust lens models of any cluster to date.

Several modeling techniques have been used to make magnification and total mass density maps of A370 (Richard et al., 2014; Johnson et al., 2014; Kawamata et al., 2018; Lagattuta et al., 2017; Diego et al., 2018), each making various assumptions about the mass distribution. For example, Richard et al. (2014); Johnson & Sharon (2016); Kawamata et al. (2018) produce high resolution maps using parametric codes to constrain the mass distribution using a simple Bayesian parameter minimization and an assumption that mass traces light. Other techniques use adaptive grid models, such as Diego et al. (2018) and the model presented here (although Diego et al. (2018) assumes that mass traces light and our method does not do so beyond the choice of initial model). These have the potential to test for systematic errors that arise from assumptions about the mass distribution. A robust measurement of error using a range of magnification maps becomes essential for any measurement made at high magnification ($\mu > 20$). For example, Bouwens et al. (2017) showed that at the faint end of the UV LF (which cannot yet be probed without lensing and where sources are more likely highly magnified), magnification errors become large. In addition, Meneghetti et al. (2017) has shown that the error in magnification is proportional to magnification. In response to the need for a wide range of lens models for each cluster being studied, magnification maps from several teams, including ours, are publicly available on the Hubble Frontier Fields website.[2]

While our method does not produce the highest resolution maps, we include both strong and weak lensing constraints and, apart from the initial model, make no assumptions about total mass distribution. Stellar mass can be independently measured using the observed stellar light, allowing total mass density maps of galaxy clusters to be compared to stellar mass density in order to obtain a stellar mass density to total mass density ratio ($f*$). This provides an independent way to see how light does or does not trace total mass in our model. In this paper, we present magnification, convergence, stellar mass density and $f*$ maps of A370.

The structure of the paper is as follows: we present a description of imaging and spectroscopic data in Section 2, a description of our gravitational lens modeling code, constraints we use in our model, and a description of our stellar mass measurement in Section 3. Following this, we present a stellar mass density to total mass density map in Section 4 and conclude in Section 5. Throughout the paper, we will give magnitudes in the AB system (Oke, 1974), and we assume a ΛCDM cosmology with $h = 0.7$, $\Omega_m = 0.3$, and $\Omega_\Lambda = 0.7$.

2.2 Observations and Data

2.2.1 Imaging and Photometry

A combination of programs from *Hubble Space Telescope* (HST), *Very Large Telescope*/High Acuity Wide-field K-band Imager (VLT/HAWK-I), and *Spitzer*/InfraRed Array Camera (IRAC) contribute to the broadband flux density measurements used in this paper. HST imaging is from HFF as well as a collection of other surveys (PI E. Hu #11108, PI K. Noll #11507, PI J.-P, Kneib #11591, PI T. Treu #13459, PI R. Kirshner #14216), and consists of deep imaging from the Advanced Camera for Surveys (ACS) in F435W (20 orbits), F606W (10 orbits), and F814W (52 orbits) and images from the Wide Field Camera 3 (WFC3) in F105W (25 orbits), F140W (12 orbits), and F160W (28 orbits). These images were taken from the Mikulski Archive for Space Telescope[3] and were also used for visual inspection of

---

[2] http://www.stsci.edu/hst/campaigns/frontier-fields

[3] https://archive.stsci.edu/

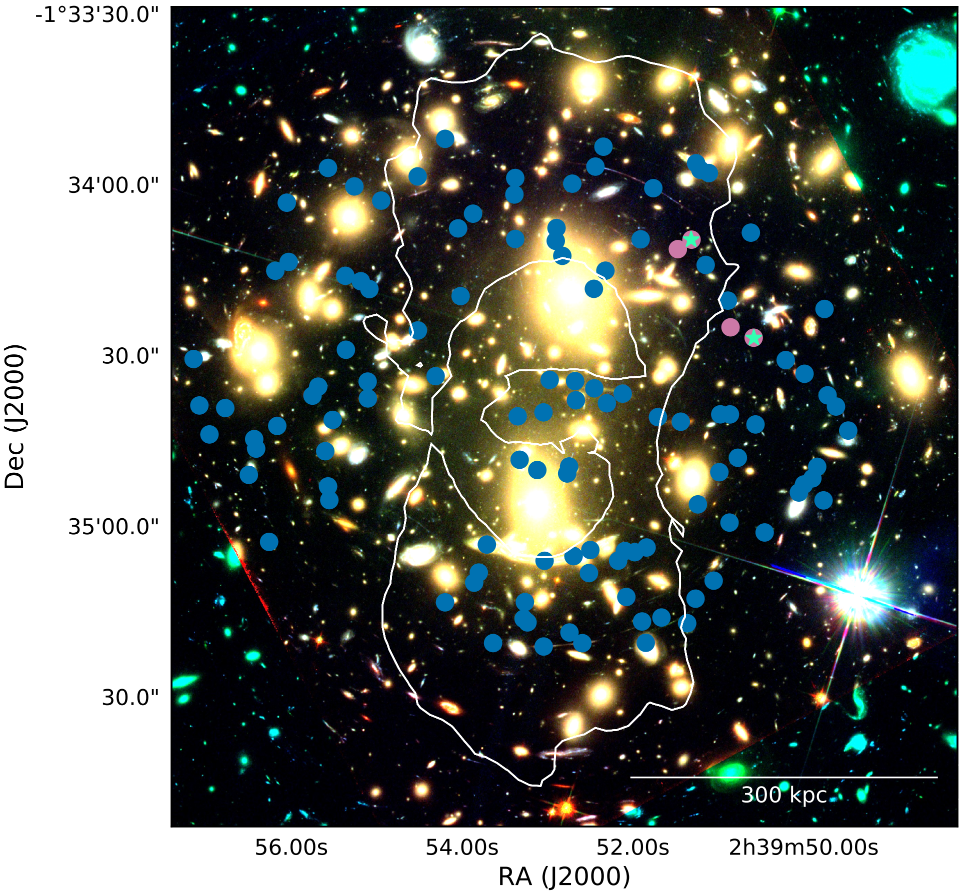

Figure 2.1: The critical curve at $z = 7.84$, the redshift of multiply imaged system 11, for our model with multiple images marked as circles. Blue circles correspond to systems with spectroscopic redshifts (more secure) and magenta circles have photometric redshifts. We show the multiple images in system 11 as cyan stars. The color image is a combination of HST filters: F105W, F606W, F814W. The orientation is north up, east to the left.

multiply-imaged systems.

Ultra-deep Spitzer/Infrared Array Camera (IRAC) images come from Spitzer Frontier Fields (PI T. Soifer, P. Capak, Lotz et al., 2017, Capak et al. in prep.)[4] and are used for photometry and creation of a stellar mass map. These images reach 1000 hours of total exposure time of the 6 Frontier Fields clusters and parallel fields in each IRAC channel. All reduction of the Spitzer data follows the routines of Huang et al. (2016b). In addition to HST and Spitzer, we use data from K-band Imaging of the Frontier Fields ("KIFF", Brammer et al., 2016), taken on VLT/HAWK-I, reaching a total of 28.3 hours exposure time for A370.

---

[4] http://irsa.ipac.caltech.edu/data/SPITZER/Frontier/

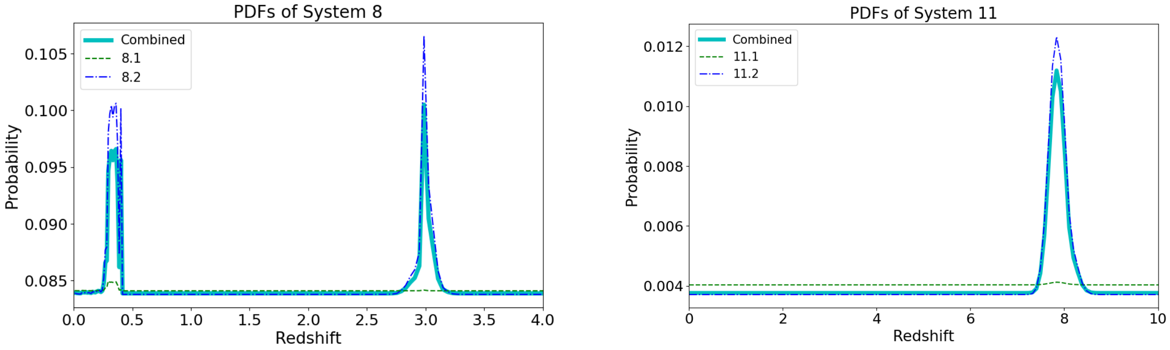

Figure 2.2: Normalized probability distribution functions for multiple image systems 8 (top) and 11 (bottom), the two systems without a spectroscopic redshift. Image 8.1 is most likely contaminated by cluster members, and shows a peak near the cluster redshift. However, there is a small peak at $z \sim 3$. Because the multiple images in systems 8 and 11 have similar morphologies, surface brightnesses, and colors, we use all images as constraints in our model. Peak redshifts and 68% confidence intervals are listed in Table 3.2.

2.2.2 Spectroscopy

Spectra are obtained from a combination of MUSE GTO observations and the Grism Lens Amplified Survey from Space (GLASS, PI Treu, HST-GO-13459, Schmidt et al., 2014; Treu et al., 2015), and are used for obtaining secure redshifts for our strong lensing constraints. Spectroscopic redshifts for systems 1-4, 6, and 9 in Table 3.2 are provided by Diego et al. (2018), which were originally obtained from GLASS[5] spectra. Data from MUSE (Lagattuta et al., 2017), provide confirmations of these as well as 31 other systems, totalling 39 spectroscopically confirmed systems, consisting of 114 multiple images. These are listed in Table 3.2, along with quality flags as defined in Diego et al. (2018). These range from 4 (best, determined by multiple high S/N emission lines) to 1 (worst, determined by one tentative, low S/N feature). The vast majority of the systems used in this work are quality flag (QF) 3, with only one image in one system with QF=1 (see Section 2.3.3 for details).

2.3 Analysis

2.3.1 Photometry

For photometry of systems that do not have any spectroscopic constraints, we follow the procedure for the ASTRODEEP catalogs described by Merlin et al. (2016); Castellano et al.

---

[5] http://glass.astro.ucla.edu/

(2016a); Di Criscienzo et al. (2017). Using the seven HFF wideband filters (F435W, F606W, F814W, F105W, F125W, F140W, F160W), HAWK-I K-band imaging (Brammer et al., 2016), and Spitzer/IRAC [3.6] and [4.5] channels (Capak et al., in prep.), the ASTRODEEP catalogs include subtraction of intracluster light (ICL) and the brightest foreground galaxies from the images. ICL subtraction is done using T-PHOT (Merlin et al., 2015), designed to perform PSF-matched, prior-based, multi-wavelength photometry as described in Merlin et al. (2015, 2016). This is done by convolving cutouts from a high resolution image (in this case, F160W) using a low resolution PSF transformation kernel that matches the F160W resolution to the IRAC (low-resolution) image. T-PHOT then fits a template to each source detected in F160W to best match the pixel values in the IRAC image.

After all fluxes are extracted, colors in HST and IRAC images are calculated and used to estimate a probability density function (PDF) for each source using the redshift estimation code Easy and Accurate Redshifts from Yale (EAZY, Brammer et al., 2008), which compares the observed SEDs to a set of stellar population templates. Using linear combinations of a base set of templates from Bruzual & Charlot (2003, BC03), EAZY performs χ^2 minimization on a user-defined redshift grid, in our case ranging from $z = 0.1 - 12$ in linear steps of $\delta z = 0.1$, and computes a PDF from the minimized χ^2 values.

To combine PDFs for images belonging to the same system, we follow the hierarchical Bayesian procedure introduced by Wang et al. (2015); Dahlen et al. (2013), which determines a combined $P(z)$ from individual $P_i(z)$ by accounting for the probability that each measured $P_i(z)$ may be incorrect (p_{bad}). In short, the method inputs the individual $P_i(z)$ if it is reliable, and uses a uniform $P_i(z)$ otherwise. Then, assuming a flat prior in p_{bad} for $p_{bad} \leq 0.5$, we marginalize over all values of p_{bad} to calculate the combined $P(z)$. This method can introduce a small non-zero floor on the PDF, but this does not affect the peak in the distribution.

2.3.2 Weak Lensing Catalog

Using ACS F814W observations of A370 from the HFF program, ellipticity measurements of 909 galaxies are identified as weak lensing constraints. To produce and reduce this catalog, we use the pipeline described by Schrabback et al. (2018) which utilizes the Erben et al. (2001) implementation of the KSB+ algorithm (Kaiser et al., 1995; Luppino & Kaiser, 1997;

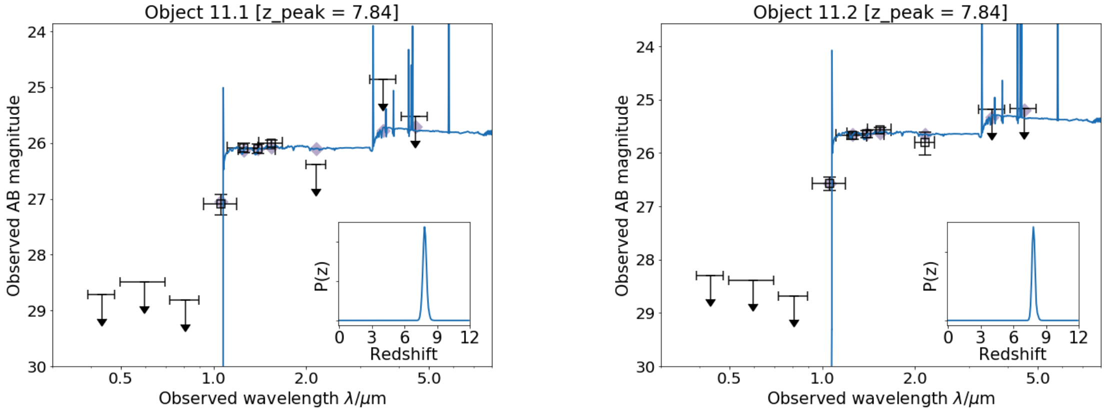

Figure 2.3: The SEDs and best-fit template for the multiple images in system 11. The IRAC fluxes were extracted from T-PHOT, and the SED fitting was done with the redshift-fitting code EAZY as described in Section 2.3.1. Error bars and upper limits shown are 1-σ. The combined PDFs of the multiple images are shown in Figure 2.2.

Hoekstra et al., 1998) for galaxy shape measurements as detailed by Schrabback et al. (2007). In addition, the pipeline employs pixel-level correction for charge-transfer inefficiency from Massey et al. (2014) as well as a correction for noise-related biases, and does temporally and spatially variable ACS point-spread function (PSF) modeling using the principal component analysis described by Schrabback et al. (2010). Schrabback et al. (2018) and Hernández-Martín et al. (in prep.) have extended earlier simulation-based tests of the employed shape measurement pipeline to the non-weak shear regime of clusters (for $|g| \leq 0.4$ where g is shear), confirming that residual multiplicative shear estimation biases are small ($|m| \lesssim 5\%$). Weak lensing galaxies extend to the edge of the ACS field of view and are individually assigned a photometric redshift from the ASTRODEEP photometry catalogs discussed in Section 2.3.2. Individual redshifts are used for all galaxies in the catalog as constraints on the lens model. The weak lensing catalog is publicly available along with the lens model products on the HFF archive.[6]

2.3.3 Multiple Images

Sets of multiple image candidates were visually inspected using HST color images by six independent teams in the HFF community, including ours, and are ranked based on the availability of a spectroscopic redshift and similarity of the images in color, surface bright-

---

[6] https://archive.stsci.edu/pub/hlsp/frontier/abell370/models/

ness, and morphology. Six independent teams inspect and vote on each image on a scale of 1-4, 1 meaning the image has a secure redshift and 4 meaning the redshift measurement is poor and the image is difficult to visually associate with a system. Votes are averaged to represent the quality of the image. In this paper we use only systems containing a majority of images with an average score of 1.5 or less. This translates to multiply imaged systems that either have a spectroscopic redshift for each image in the system, or images that have PDFs in agreement to 1-σ. Alternatively, the system has at least one spectroscopically confirmed image and other images have convincingly similar colors, morphologies, and surface brightnesses. Our numbering scheme is adopted from Lagattuta et al. (2017); of our 39 multiply-imaged systems, 37 are spectroscopically confirmed (systems labeled "z-spec" in Table 3.2, blue points in Figure 2.1).

These systems' spectroscopic redshifts have been collected over time, starting with systems 1 (Kneib et al., 1993), 2 (Soucail, 1987), and 3 (Richard et al., 2014). These, in addition to 10 unconfirmed systems, were used by Richard et al. (2014). With GLASS spectroscopy, Diego et al. (2018) confirmed these as well as systems 4, 6, 9, and 15. Finally, Lagattuta et al. (2017) confirmed 10 additional systems (5, 7, 14, 16, 17, 18, 19, 20, 21, and 22). Following the lead of Diego et al. (2018) and Lagattuta et al. (2017), we treat system 7 (named systems 7 and 10 in Lagattuta et al. (2017) and systems 7 and 19 in Diego et al. (2018)) as a single system due to the fact that all images appear to be from the same source galaxy at the same spectroscopic redshift (measured by Lagattuta et al., 2017). We use all 39 systems as constraints in our model, including one that is lensed by a smaller cluster member on the outskirts of the field (system 37) and two others that are not spectroscopically confirmed (systems 8 and 11; see Figure 2.2). This is summarized in Table 3.2.

2.3.4 System 11

We note in particular system 11, a set of sources we believe to be multiply imaged, with photometric redshifts both peaking at $z = 7.84 \pm 0.02$ (Figure 2.3). This system was found to be at $z = 5.9$ in Richard et al. (2014); Diego et al. (2018), and $z = 4.66$ in Lagattuta et al. (2017). In previous versions of our model, system 11 was found to be at $z \sim 4$. This redshift was obtained from HST only photometry, which has since been improved to include better ICL subtraction and *Spitzer*/IRAC fluxes, as described in Section 2.3.1. The photometric redshift of both images are now preferred at $z = 7.84 \pm 0.02$. For a multiply imaged system such as system 11, which contains two images of opposite parity and similar surface brightnesses, the critical curve should appear between the images, approximately equidistant from each. Based on the critical curve placement near system 11, the new redshift is in broad agreement with all models of A370, and these results are consistent with photometric results presented by Shipley et al. (2018).

We show the SED and best-fit template from EAZY in Figure 2.3, where all error bars and upper limits shown are 1-σ. In object 11.1, the covariance index is found to be ~ 1.24 for both IRAC channels. The covariance index is defined as the ratio between the maximum covariance of the source with its neighbors over its flux variance, which serves as an indicator of how strongly correlated the source's flux is with its closest or brightest neighbor. Generally, a high covariance index (> 1) is associated with more severe blending and large flux errors (Laidler et al., 2007; Merlin et al., 2015), so we treat these fluxes with caution. Because of the high confidence in visual detection of the object and its multiple image, we include the flux upper limits in our SED fit. However, when EAZY is run without these flux values included, the best-fit SED template and $z \sim 8$ solution remains, with a slightly broader PDF. The combined photometric redshift probability distributions are shown in Figure 2.2.

The unlensed absolute magnitudes of the images are $-18.68^{+0.10}_{-0.08}$ and $-18.16^{+0.07}_{-0.08}$ for 11.1 and 11.2, respectively, where photometric errors in AB flux measurement and statistical errors in magnification are included. While these values are not in statistical agreement, the uncertainty in magnification close to the critical curve is larger than the statistical uncertainty in our model. While our model predicts positions of the sources well, we do not use brightness of sources as constraints. Ultimately, spectra will be needed to confirm or deny the redshift of the sources. Both images in system 11 fall outside of the coverage of the MUSE GTO program (Lagattuta et al., 2017), but were observed by GLASS and with the Multi-Object Spectrometer for Infra-Red Exploration (MOSFIRE) instrument on Keck. However, these data do not constrain any noticeable spectroscopic features and therefore do not constrain the spectroscopic redshift Hoag et al. (2018).

While the images in system 11 are observed as relatively bright objects, they are intrinsically faint, which offers a unique chance to study a more representative example of a $z \sim 8$ galaxy. The source being multiply imaged will allow for better statistics on the properties inferred about it. This makes the source an ideal target for *James Webb Space Telescope*, as emission lines at this observed brightness will likely be detectable.

2.3.5 Lens Modeling Procedure

The lens modeling code used in this work, Strong and Weak Lensing United (SWUnited, Bradač et al., 2005, 2009), uses an iterative χ^2 minimization method to solve for the gravitational potential on a grid. The method constructs an initial model assuming a range of profiles (we use the non-singular isothermal ellipsoid as our initial model here) and uses multiple images reconstructed in the source plane as constraints. A χ^2 is calculated upon each iteration using gravitational potential values on a set of non uniform grid points on an adaptive grid. The grid uses higher resolutions near areas where there are many constraints and is determined by a set of user-created refinement regions, which consist of circles of given radii that appoint levels of resolution. We optimize the model using a χ^2 defined as:

$$\chi^2 = \chi^2_{\mathrm{SL}} + \chi^2_{\mathrm{WL}} + \eta R, \tag{2.1}$$

where χ^2_{SL} is a strong lensing term in the source plane, χ^2_{WL} is a weak lensing term that uses ellipticies of weakly lensed galaxies as constraints, and η is a regularization parameter of the regularization function R that penalizes small-scale fluctuations in the gravitational potential. After finding a minimum χ^2, the code produces convergence (κ), shear (γ), and magnification (μ) from the best-fit solution.

Our method differs from other parameterized codes in that we do not make any assumptions regarding light tracing mass. It is parameterized in that there are parameters which are obtained via minimization, i.e. the gravitational potential in each cell, but they are kept as general as possible and the minimization is done on a non-uniform grid, while other codes compare strong nd weak lensing constraints in parameter space using a Bayesian approach and assuming simple parameterized models. In addition, we include weak lensing constraints that extend to the center of the cluster. While the method employed by Diego et al. (2018)

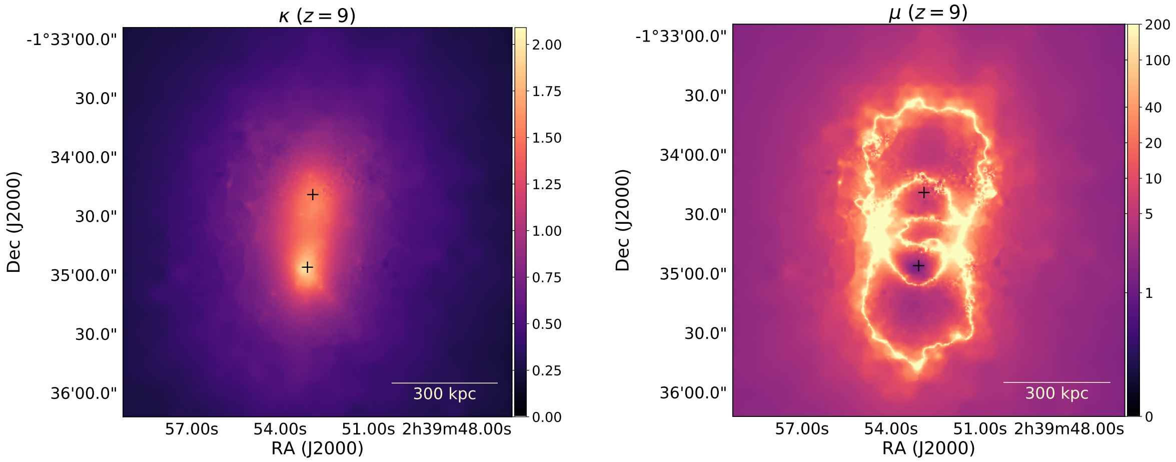

Figure 2.4: Left: Convergence (κ) map of Abell 370 produced by our lens model for a source at $z = 9$. BCG centers are shown as crosses. Two dominant peaks in mass density near the location of the BCGs are shown, with a small offset between the southernmost BCG and mass density peak. **Right:** Magnification (μ) map of Abell 370 for a source at $z = 9$. The yellow contour corresponds to maximum magnification values; a highly elliptical and extended critical curve is revealed, similar in shape to those found by other groups (e.g., Diego et al. (2018); Lagattuta et al. (2017) and other groups on the HFF archive. Orientation is the same as in Figure 2.1.

has the ability to use weak lensing constraints, they do not do so for A370, and no other groups from the HFF campaign use weak lensing constraints on this cluster.

2.3.6 Stellar Mass Map

Rest-frame K-band flux has been shown to estimate stellar mass well due to its insensitivity to dust within the observed cluster (Bell et al., 2003) and lack of dependence on star formation history (Kauffmann & Charlot, 1998). Since IRAC channel 1 (3.6μm, [3.6] hereafter) is the closest band corresponding to rest-frame K-band of the cluster, we use it to estimate stellar mass of A370 using flux in cluster members in this channel. Cluster members are selected using the red sequence (F435W and F814W magnitudes), visually inspected to remove the obvious outliers, and redshifts are verified to be within ± 0.1 of the mean cluster redshift ($z = 0.375$) with GLASS spectroscopy.

Following the procedure described by Hoag et al. (2016), we create a mask of cluster members from an F160W segmentation map of the field, convolve the map with the IRAC channel 1 PSF, and resample onto the IRAC pixel grid. We then apply this mask to the IRAC channel 1 image in order to get a [3.6] map containing only light (to a good approximation) from cluster members. After smoothing the IRAC surface brightness map with a Gaussian kernel of $\sigma = 3$ pixels, we calculate luminosities of the cluster members using [3.6] flux, and apply a K-correction of -0.33 to bring them to K-band for the mean cluster redshift. We then multiply the map by a mass to light ratio, $M*/L = 0.95 \pm 0.26 M_\odot/L_\odot$, obtained in Bell et al. (2003) assuming the diet Salpeter IMF. This choice contains 70% the mass of the Salpeter IMF for the same photometry, and is used here for comparison of our results to previous results (Wang et al., 2015; Hoag et al., 2016; Finney et al., 2018).

Since IMF can change $\langle f^* \rangle$ by as much as 50%, this choice introduces our largest error in estimating stellar mass. Additional sources of error include our calculation of stellar mass using a single mass to light ratio and choice of template used to calculate the K-correction instead of deriving stellar mass from SED fitting. When comparing stellar mass calculations of both methods in clusters similar to A370, we find that this choice produces a 0.05 dex bias, which translates to a 10% underestimate in stellar mass using our method. Other errors include statistical errors and an underestimation of stellar mass due to not accounting for stars in the ICL. Montes & Trujillo (2018) found A370 to have $4.9 \pm 1.7\%$ of total light within a radius of R_{500} residing in the ICL. However, these errors are all sub-dominant and negligible compared to the uncertainty related to the choice of IMF (Burke et al., 2015).

2.4 Results

2.4.1 Mass and Magnification

Convergence κ and magnification μ maps for a source at $z = 9$ are shown in Figure 2.4, displaying two dominant peaks. The southernmost brightest cluster galaxy (BCG) is roughly aligned with the convergence peak, however the northernmost κ peak is significantly less concentrated and shows a small offset from the stellar mass. There are less significant peaks in the κ map around the cluster members in the northeast and a bright cluster member in the southwest. The yellow contour in the magnification map is the critical curve, where the magnification is at a maximum. Magnification reaches up to $\mu \sim$ 10-20 within 1-2 arcseconds from the critical curve, while typical values of magnification range from $\mu \sim$ 2-5 near the edges of the HST field.

In the absence of an ability to compare our model to truth, a comparison of parametric, free-form, and grid-based modeling codes is helpful to properly account for the systematic uncertainties of each method that can produce this spread. When comparing our magnification map to previous models of A370, we only compare to models updated since the last data release. Group names are: Glafic (Oguri, 2010; Kawamata et al., 2018), CATS (Lagattuta et al., 2017), Diego (Diego et al., 2018), Keeton, Merten, Sharon, and Williams. More information about each method can be found on the HFF archive[7]. As shown in Figure 2.5, our critical curves are approximately of the same ellipticity and extent, with a larger radial region compared to many of the groups. With the exception of the Williams map which has a boxy shape, the overall shapes are comparable. The critical curve at $z = 7.84 \pm 0.02$ (the redshift of System 11) for our model is shown in Figure 2.1 and at $z = 9$ in Figure 2.4. On smaller scales, the magnification levels differ greatly from group to group, particularly very close to the critical curves. The black stars in Figure 2.5 correspond to the multiple images in System 11, and we find that the critical curves of all models fall in a reasonable place to be consistent with the new redshift. Explicitly, Lagattuta et al. (2017) finds that model constraints allow a range of $2.5 < z < 10$ when the redshift of this system is varied as a free parameter, consistent with a $z = 7.84 \pm 0.02$ solution.

In Figure 2.6 we compare surface mass density (κ) distributions. There are obvious differences, such as clear high residuals over cluster members in the groups who use lensing codes that assume light traces mass (Sharon, CATS, Glafic, Keeton, Diego). There is also a large residual in the south of the Williams map, where the Williams model differs from most other models. Compared to Diego et al. (2018) and Lagattuta et al. (2017), we have smaller κ values in the northeast.

2.4.2 Stellar to Total Mass Ratio

To study the difference in stellar mass from cluster members and total cluster mass, we look at the stellar mass to total mass fraction, $f*$. We obtain an $f*$ map by dividing the total stellar mass density in a 0.3 Mpc radius by the total projected mass density in the same radius, after adjusting the resolution (i.e. by smoothing) and pixel scale of the stellar mass density map to match that of the total mass density map, which was determined by the refinement region discussed in Section 3 (see Hoag et al. (2016) for details on this procedure). The resulting $f*$ map is shown in Figure 2.7. There is considerable variation

---

[7] https://archive.stsci.edu/pub/hlsp/frontier/abell370/models/

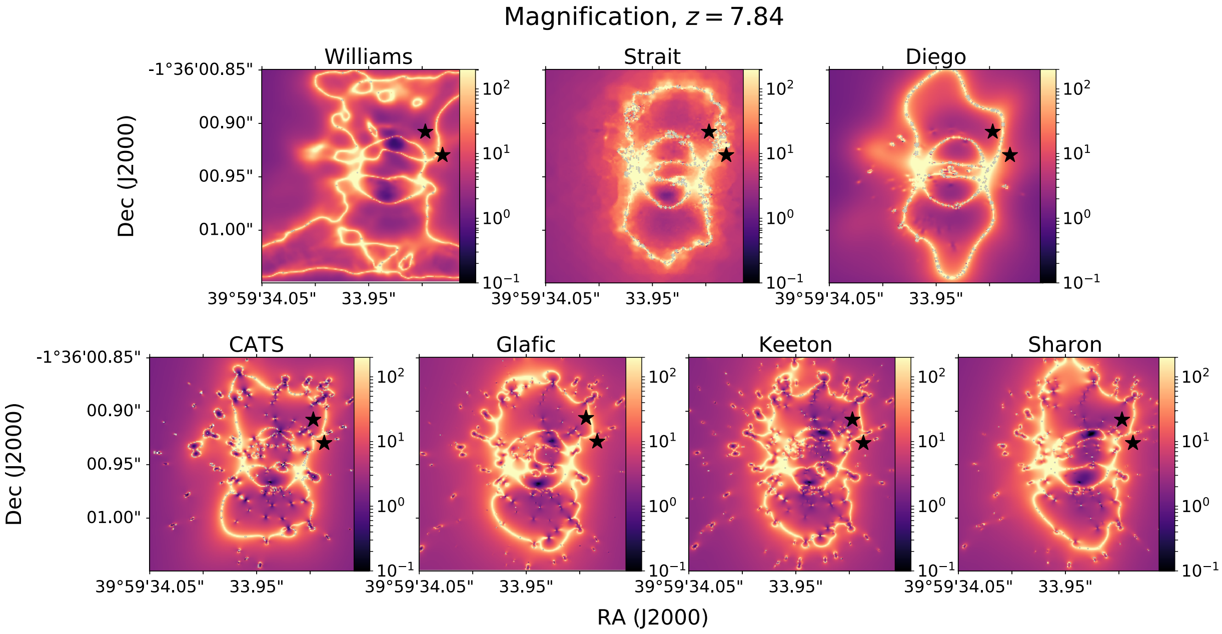

Figure 2.5: Critical curves at $z = 7.84$, the photometric redshift of the images in System 11. Black stars mark the position of the multiple images. The CATS and Sharon groups use lenstool, which uses individual galaxies and other large parameterized mass components. Keeton and Glafic teams are also parametric models, and Diego uses a non-parametric lensing code but a light traces mass assumption. The Williams team along with ours make no such assumptions. All teams but ours used strong lensing constraints only. While shapes of critical curves vary, all groups, including ours (see Figure 2.1), show good agreement for the images at $z = 7.84$.

throughout the map, reaching values near 0.03-0.04 on top of the northern BCG. The stellar mass and f^* map reflects what is expected, with higher values around the cluster members in the northeast and to the west over a particularly bright galaxy. There is a peak in stellar mass on top of both BCGs, as expected, but the northernmost peak is higher and offset by a modest amount from the stellar mass peak caused by the BCG. The high offset peak in combination with a less significant peak in the total mass on the northern BCG creates the highest peak in the f^* map.

We find that average f^* in a circular aperture of radius 0.3 Mpc is $\langle f^* \rangle = 0.011 \pm 0.003$, when centered over a midpoint in between the BCGs. We select BCG centers using flux peaks in F160W images, however we cannot include details of how centers were chosen in other analyses presented here, as that information was not publicly available. If re-calculated using a radius of the same size centered on the southern and northern BCG, we find a value

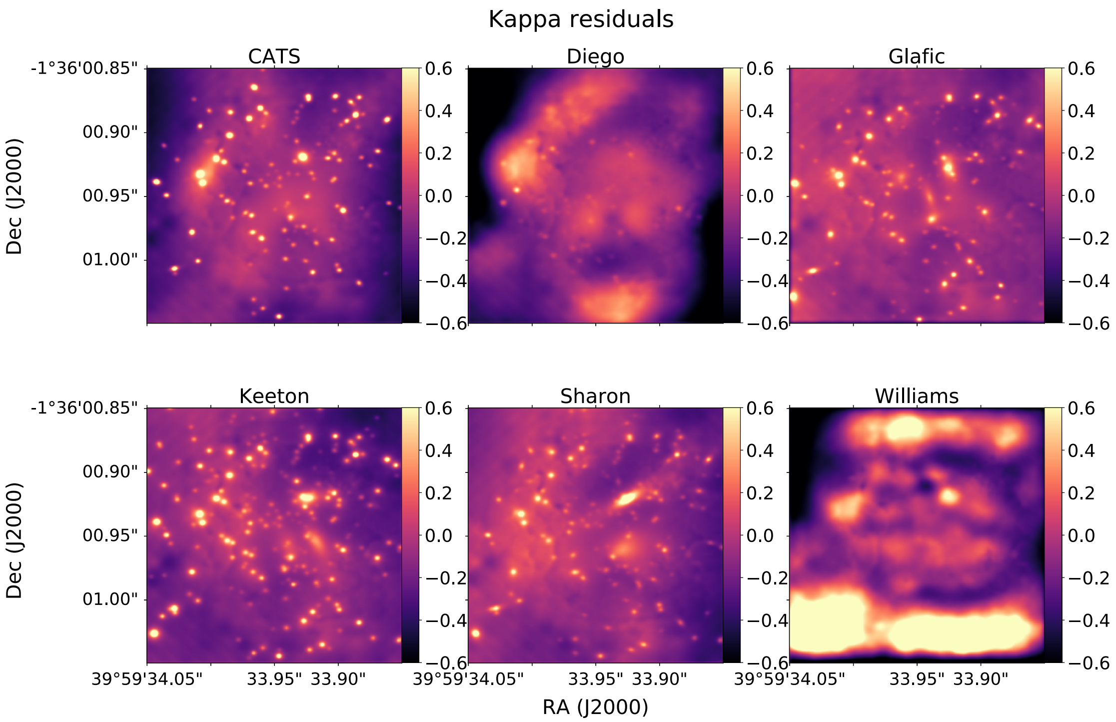

Figure 2.6: Kappa residuals ($(\kappa_i - \kappa_{VS})/\kappa_{VS}$), where κ_i are convergence maps from six models and κ_{VS} is the convergence map presented here, smoothed with a Gaussian filter of $\sigma = 10$. See caption of Figure 2.5 and Section 2.4.1 for a description of the groups and lens modeling methods.

of $\langle f^* \rangle = 0.011 \pm 0.003$ and $\langle f^* \rangle = 0.012 \pm 0.003$, respectively. As was the case with the stellar mass map, the choice of IMF is the largest source of error by an order of magnitude, with the ability to change our value of $\langle f^* \rangle$ by as much as 50%.

In comparing our average value of stellar to total mass to clusters of similar mass and redshift, we find good agreement. Average f^* obtained for a radius of 0.3 Mpc around MACSJ0416 ($z = 0.396$) in Hoag et al. (2016) is $\langle f^* \rangle = 0.009 \pm 0.003$, and Finney et al. (2018) obtain a value of $\langle f^* \rangle = 0.012^{+0.003}_{-0.005}$ for MACS1149 ($z = 0.544$). Both calculations use SWUnited maps and a diet Salpeter IMF. Similarly, using the SWUnited maps produced by Wang et al. (2015) for Abell 2744 ($z = 0.308$), we find a value of $\langle f^* \rangle = 0.003 \pm 0.001$. In another analysis of MACS0416, Jauzac et al. (2016) find a value of $\langle f^* \rangle = 0.0315 \pm 0.0057$ using a Salpeter IMF and a radius of 200 kpc. When re-calculated using the diet Salpeter IMF, we get a value of 0.0221 ± 0.0057 for MACSJ0416. In a study of 12 clusters near $z \sim 0.1$ with masses greater than $2 \times 10^{14} M_\odot$, Gonzalez et al. (2013) found a value of $\langle f^* \rangle$ to be 0.0015-0.005 in a radius of 1.53 ± 0.08 Mpc. Bahcall & Kulier (2014) find a similar

Table 2.1. Comparison of $\langle f^* \rangle$ to values in iterature

$\langle f^* \rangle$	Object	Redshift	Radius	IMF	Reference
0.011 ±0.003	A370	0.375	0.3 Mpc	diet Salpeter	This paper
0.009 ± 0.003	MACS0416	0.396	0.3 Mpc	diet Salpeter	Hoag et al. (2016)
$0.012^{+0.003}_{-0.005}$	MACS1149	0.544	0.3 Mpc	diet Salpeter	Finney et al. (2018)
0.0015-0.005	12 clusters	~ 0.1	1.5 3Mpc	Salpeter	Gonzalez et al. (2013)
0.003 ± 0.001	A2744	0.308	0.3 Mpc	diet Salpeter	Wang et al. (2015)
0.0221 ± 0.0057	MACS0416	0.396	200 kpc	Salpeter	Jauzac et al. (2016)
0.010 ± 0.004	MaxBCG clusters	0.1-0.3	> 200 kpc	Chabrier	Bahcall & Kulier (2014)

value of 0.010 ± 0.004 on all scales larger than 200 kpc, when examining f^* for more than 13,823 clusters in the redshift range $0.1 < z < 0.3$, selected from the MaxBCG catalog (Koester et al., 2007); however, they use SDSS i-band to calculate stellar mass and assume a Chabrier IMF. When re-calculated using a diet-Salpeter IMF, we obtain $f^* = 0.012 \pm 0.005$ for this sample. These results are summarized in Table 2.1.

In general, we find that stellar mass traces total mass in the center of the cluster reasonably well, with the exception of a small offset near the northern BCG. This could be due to the cluster's bimodal distribution which indicates a possible merger. In comparing to the smoothed light maps presented in Lagattuta et al. (2017), we see a similar distribution over each BCG and the "crown" of galaxies in the north. Our total mass over those cluster members, however, is lower than theirs, as seen in the peak in the northeast of the f^* map (Figure 2.7). This is also reflected in the positive residual seen in the CATS panel of Figure 2.6.

The differences in total mass in the central part of the cluster mentioned in Section 2.4.1 also appear in the critical curve placement, which can be seen in Figure 2.1. The critical curve shown in Figure 2.1 is for $z \sim 7.84$ but crosses the radial system 7 ($z = 2.75$), meaning there is likely a higher κ and a larger critical curve in that region. This results in a lack of ability to recreate the system 7 images, but can be improved upon by adding a peaky mass clump to the center of the lens model. Diego et al., 2018 showed that adding a mass clump

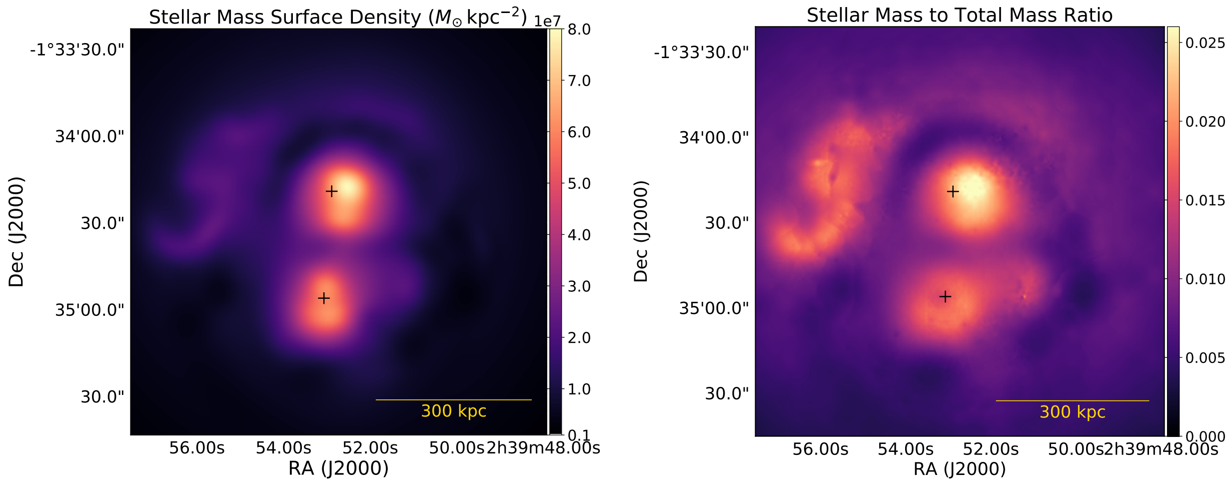

Figure 2.7: Left: Stellar surface mass density in units of $M_\odot$ kpc^{-2}, produced from an IRAC [3.6] image as described in Section 3.4. **Right:** Stellar to total mass ratio (f^*), produced by matching the resolution of the stellar mass map to the adaptive grid from the total mass map and dividing. The center of BCGs are shown as crosses. The largest peak in this figure is over the northernmost BCG where there are high values of stellar mass due to a bright BCG and low values of total mass, from the lens model. The black crosses are centered over the peak in light from each BCG as determined from the HST image.

respresenting stellar mass improves their model in the central region of the cluster, where system 7 resides. Similarly, this addition of mass in the center of the two BCGs improves our model's prediction of system 7 images to sub-arcsecond precision. While Diego et al. (2018) find that this addition of mass causes high $f*$ values $(30-100\%)$ in the center of the BCGs, our model predicts a more moderate value of $f* \sim 3\%$.

2.5 Conclusions

A370 is a cluster located at $z = 0.375$ that acts as a powerful gravitational lens, behind which deep HST images have revealed 39 multiply-imaged source galaxies consisting of 114 images. Using spectroscopic redshifts from MUSE and GLASS, we produce a total projected mass density and magnification map with the grid-based lens modeling code SWUnited. Using IRAC [3.6] images, we calculated stellar mass and f^*, the stellar to total mass density fraction in the field. Our main results are as follows:

1. Using 37 multiply-imaged systems that have spectroscopically confirmed redshifts and 2 systems with photometric estimates, we constrain the total mass density distribution using lens modeling code SWUnited. The convergence (κ) and magnification (μ) maps

that we produce broadly agree with other models in ellipticity and size. There are discrepancies in the exact placement of the critical curves, producing variations in magnification levels in regions of high magnification, but there is agreement elsewhere. Our κ map shows two dominant peaks, the northernmost peak being more diffuse than that of the southern BCG.

2. There is a multiply imaged system consisting of two images, both with photometric redshifts peaking at $z = 7.84 \pm 0.02$. This result comes from ASTRODEEP-like photometry and is in agreement with photometry by Shipley et al. (2018). The unlensed absolute magnitudes of the images are not consistent with that of an individual multiply imaged source at the 3-σ level, when considering only statistical errors. In order to be consistent with the same source, an additional systematic must be present, most likely in the magnification ratio.

3. The f^* map that we produce using an IRAC 3.6μm image shows considerable variation throughout the field of view. There are expected dominant peaks in the f^* map near the BCGs, with higher values in the northern BCG. This is due to a modest offset in total mass and stellar mass in the northern part of the cluster, possibly due to a merger process.

4. We obtain a value of stellar to total mass ratio within 0.3 Mpc of $f* = 0.011 \pm 0.003$ (stat.), with the largest systematic error due to our choice of IMF. This value agrees broadly with clusters of similar size and redshift, and with values found for large scale (> 1 kpc) cluster environments.

Acknowledgements

Support for this work was provided by NASA through an award issued by JPL/Caltech (for SURFS UP project) and by HST /STScI HST-AR-13235, HST-AR-14280, and HST -GO-13177. Support for the Grism Lens-Amplified Survey from Space (GLASS) (HST-GO-13459) was provided by NASA through a grant from the Space Telescope Science In- stitute (STScI). This work utilizes gravitational lensing models produced by PIs Bradac, Richard, Natarajan & Kneib (CATS), Sharon, Williams, Keeton, and Diego. This lens modeling was partially funded by the HST Frontier Fields program conducted by STScI. STScI is operated by the Association of Universities for Research in Astronomy, Inc. under NASA contract NAS 5-26555. Lens models were obtained from the Mikulski Archive for Space Telescopes (MAST). B.V. acknowledges the support from an Australian Research Council Discovery Early Career Researcher Award (PD0028506). T.T. and X.W. acknowledge support by NASA through HST grants HST-GO-13459 and HST-GO-14280.

Chapter 3

Stellar Properties of Galaxies at $z \gtrsim 8$

This chapter was originally published as an article with the title *Stellar Properties of* $z \gtrsim 8$ *Galaxies in the Reionization Cluster Lensing Survey*, which was published in Volume 888 of the *Astrophysical Jornal.*

Measurements of stellar properties of galaxies when the universe was less than one billion years old yield some of the only observational constraints of the onset of star formation. We present here the inclusion of *Spitzer*/IRAC imaging in the spectral energy distribution fitting of the seven highest-redshift galaxy candidates selected from the *Hubble Space Telescope* imaging of the Reionization Lensing Cluster Survey (RELICS). We find that for 6/8 *HST*-selected $z \sim 8$ sources, the $z \sim 8$ solutions are still strongly preferred over $z \sim$1-2 solutions after the inclusion of *Spitzer* fluxes, and two prefer a $z \sim 7$ solution, which we defer to a later analysis. We find a wide range of intrinsic stellar masses ($5 \times 10^6 M_\odot - 4 \times 10^9\ M_\odot$), star formation rates (0.2-14 $M_\odot \mathrm{yr}^{-1}$), and ages (30-600 Myr) among our sample. Of particular interest is Abell1763-1434, which shows evidence of an evolved stellar population ($\sim$ 500 Myr) at $z \sim 8$, implying its first generation of star formation occurred $<$ 100 Myr after the Big Bang. SPT0615-JD, a spatially resolved $z \sim 10$ candidate, remains at its high redshift, supported by deep *Spitzer*/IRAC data, and also shows some evidence for an evolved stellar population. Even with the lensed, bright apparent magnitudes of these $z \gtrsim 8$ candidates (H = 26.1-27.8 AB mag), only the *James Webb Space Telescope* will be able to exclude the possibility that abnormally strong nebular emission, large dust content, or some combination

thereof, and confirm the presence of evolved stellar populations early in the universe.

3.1 Introduction

High-z galaxies are key sources in the epoch of reionization, and to understand the contributions of the $z \sim 8-10$ population by way of ionizing photon production, we need measurements of star formation rate (SFR) and stellar mass. However in practice, robust constraints on physical properties of $z \sim 8-10$ galaxies are difficult to place. Surveys using lensing and blank fields to target high-z galaxies in recent years have rapidly grown the sample (for a review of theoretical models compared to most observations to date, see Dayal & Ferrara, 2018). In particular, measurements of ages of galaxies in the high-z universe have provided one of the few observational probes of the onset of star formation (e.g., Egami et al., 2005; Richard et al., 2011; Huang et al., 2016b). The most recent spectroscopically confirmed example by Hashimoto et al. (2018) (see also Zheng et al., 2012; Bradač et al., 2014; Hoag et al., 2018) implies first star formation at ~ 250 Myr after the Big Bang as evidenced by an old stellar population in the galaxy MACS1149-JD.

There are also a number of galaxies that are not yet spectroscopically confirmed and show signs of a possible evolved stellar population at high-z. At $z \sim 8$, spectral energy distribution (SED) results are heavily influenced by near-IR fluxes, since the Balmer/$D_n(4000)$ break (hereafter Balmer break) falls into *Spitzer* channel 1 (3.6μm, [3.6] or ch1 hereafter) from $z \sim 7-10$, requiring *Spitzer* fluxes for robust measurements of stellar mass, SFR, and age. Complicating the problem, strengths of nebular emission lines and dust content at these redshifts are unknown, creating a degeneracy between emission lines and the Balmer break that is difficult to disentangle with the currently available near-IR broadband observations. When a spectroscopic redshift is available, it is sometimes possible to disentangle the degeneracy if the emission lines fall outside of a broadband, as in Hashimoto et al. (2018). While the *James Webb Space Telescope* (JWST) will ultimately be able to break most of these degeneracies, identifying candidates with broadband photometry for follow-up and an initial investigation of their stellar properties are important scientific goals.

So far, there have been 100-200 $z \gtrsim 8$ candidates identified in *Hubble Space Telescope* (*HST*) surveys that utilize gravitational lensing by massive galaxy clusters and in blank field surveys (e.g., Bradley et al., 2014; Bouwens et al., 2015b; Finkelstein et al., 2015; Oesch et al., 2015; Ishigaki et al., 2018; Morishita et al., 2018; Bouwens et al., 2019; De Barros et al., 2019). Photometric redshifts of this sample are largely based on rest-frame UV + optical photometry (*HST* + *Spitzer*/IRAC), and only a small subset are spectroscopically confirmed. Without a spectroscopic confirmation, *Spitzer* fluxes can aid in removing low-redshift interlopers from these samples. Even with a spectroscopic confirmation, *Spitzer*/IRAC (rest-frame optical) fluxes are essential for robust measurements of stellar properties (González et al., 2011; Ryan et al., 2014; Salmon et al., 2015).

Here we use *HST* and *Spitzer*/IRAC imaging data from the Reionization Lensing Cluster Survey (RELICS, PI Coe) and companion survey, *Spitzer*-RELICS (S-RELICS, PI Bradač) to probe rest frame optical wavelengths of seven $z \gtrsim 8$ candidates originally selected with *HST*. Details of the *HST*-selected high-z candidates can be found in Salmon et al. (2018, 2020) (hereafter S18, S20). We present measurements of stellar mass, SFR, and age inferred from *HST* and *Spitzer* broadband fluxes.

In §3.2 we describe *HST* and *Spitzer* imaging data and photometry. In §3.3 we discuss the lens models used in our analysis. In §3.4 we describe our photometric redshift procedure, SED modeling procedure and calculation of stellar properties. We present our SED fitting and stellar properties results in §3.5 and we conclude in §3.6. Throughout the paper, we give magnitudes in the AB system (Oke, 1974), and we assume a ΛCDM cosmology with $h = 0.7$, $\Omega_m = 0.3$, and $\Omega_\Lambda = 0.7$.

3.2 Observations and Photometry

HST reduced images and catalogs are publicly available on Mikulski Archive for Space Telescopes (MAST[1]) and *Spitzer* reduced images on NASA/IPAC Infrared Science Archive (IRSA[2]). Details of the survey can be found in Coe et al. (2019). Here we focus on the six clusters with $z \gtrsim 8$ candidates (Abell 1763, MACSJ0553-33, PLCKG287+32, Abell S295, RXC0911+17, and SPT0615-57, Figure 3.1).

---

[1] https://archive.stsci.edu/prepds/relics/

[2] https://irsa.ipac.caltech.edu/data/SPITZER/SRELICS/

Table 3.1. $z \gtrsim 8$ galaxy candidates and selected photometry

Object ID	R.A. (deg.)	Dec. (deg.)	$F160W$[1] (mag)	Ks (mag)	[3.6][2] mag	$R_{3.6}$[3]	[4.5][2] (mag)	$R_{4.5}$[3]
Abell1763-0460	203.8249758	+41.0091170	27.8 ± 0.2		>25.9	0.37	24.5 ± 0.2	0.39
Abell1763-1434	203.8333744	+40.9901793	26.1 ± 0.1		25.5 ± 0.4	0.29	24.5 ± 0.2	0.28
AbellS295-0568	41.4010242	-53.0405184	26.3 ± 0.1		>26.2	0.16	>26.3	0.14
MACS0553-33-0219	88.3540349	-33.6979484	27.2 ± 0.2		25.0 ± 0.3	0.34	25.5 ± 0.6	0.34
PLCKG287+32-2032	177.7225936	-28.0850703	26.7 ± 0.2	26.6 ± 0.3	>26.6	0.53	>26.4	0.59
RXC0911+17-0143	137.7939712	+17.7897516	26.5 ± 0.1		>26.4	0.05	>26.1	0.04
SPT0615-JD	93.9792550	-57.7721477	25.8 ± 0.1		26.0 ± 0.6	1.43	25.4 ± 0.4	1.13

[1] Total lensed magnitude (`FLUX_ISO`)

[2] *Spitzer/IRAC* Channels 1 and 2 magnitudes measured with the same aperture as HST magnitudes and 1-σ error. If detection is < 1-σ, 1-σ lower limit is reported.

[3] Covariance index for *Spitzer*/IRAC channels (Section 3.2.2)

3.2.1 *HST*

Each cluster was observed with two orbits of WFC3/IR imaging in F105W, F125W, F140W, and F160W and with three orbits in ACS (F435W, F606W, F814W), with the exception of Abell1763 which received seven additional WFC3/IR orbits. In this work, we use the catalogs based on a detection image comprised of the 0.06″/pix weighted stack of all WFC3/IR imaging, optimized for detecting small high-z galaxies, described in Coe et al. (2019).

3.2.2 Spitzer Data and Photometry

Each cluster was observed with *Spitzer*/IRAC by a combination of RELICS programs (PI Soifer, #12123, PI Bradač #12005, 13165, 13210) and archival programs. PLCKG287+32, Abell 1763 and SPT0615-57 were observed for 30 hours each in [3.5] and [4.6] channels, including archival data (PI Brodwin #80012). Abell S295 was observed for 5 hours in each channel, including archival data (PI Menanteau #70149). MACS J0553-33 was observed for 5.2 hours in each channel including archival data (PI Egami #90218). RXC0911+17 was observed for 5 hours with archival data only (PI Egami #60032). In addition to *Spitzer* and *HST* fluxes, we include Ks imaging from VLT-HAWK-I (#0102.A-0619, PI Nonino) for

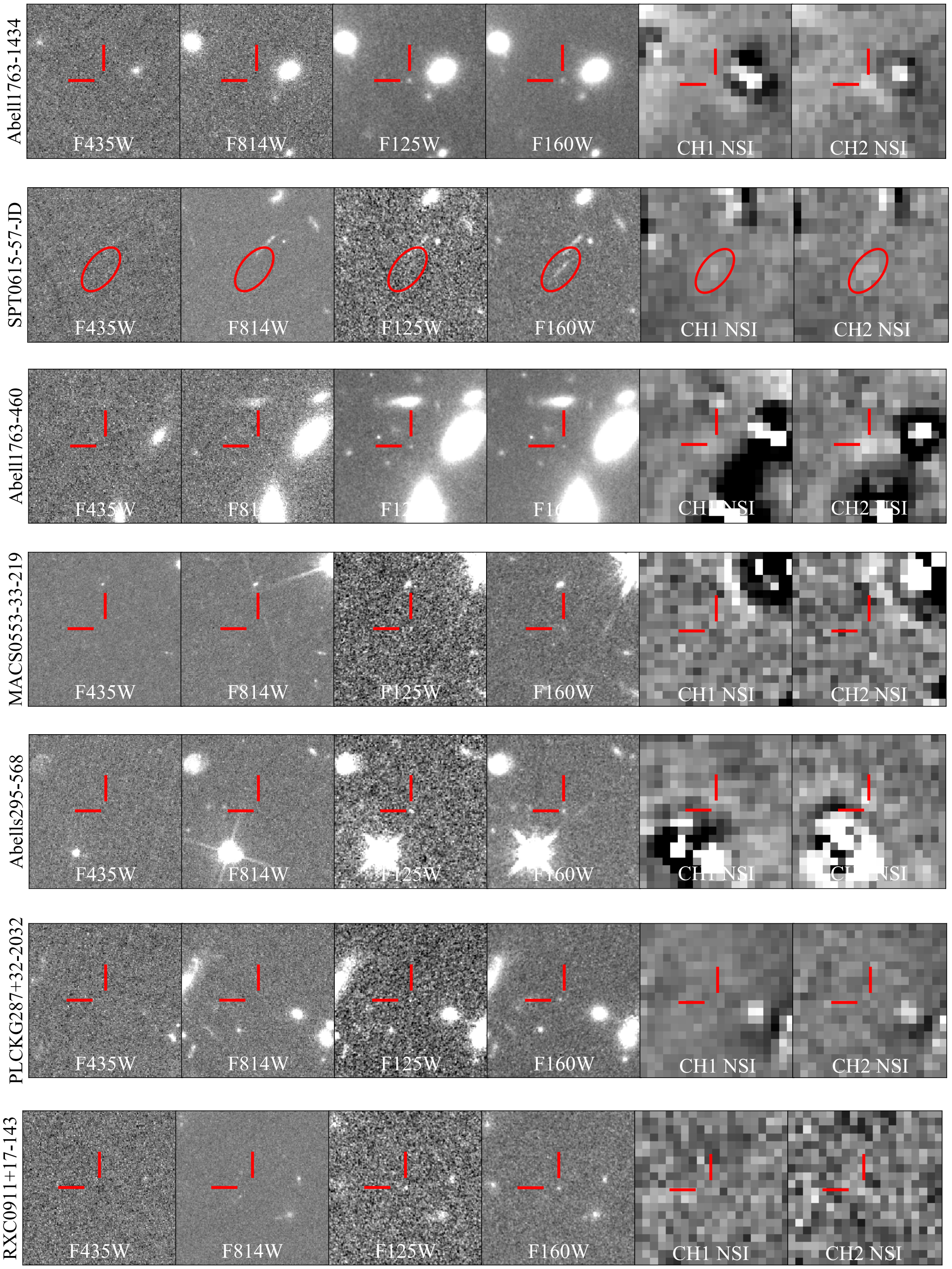

Figure 3.1: Image stamps for each candidate, $12'' \times 12''$, of two ACS bands (F435W and F814W), two WFC3 bands (F125W and F160W), *Spitzer*/IRAC Ch1 ([3.6]) and Ch2 ([4.5]). The *Spitzer* cutouts are neighbor-subtracted images (NSI), i.e., everything in the field is subtracted except the high-z source. Red lines mark the location of the source.

PLCKG287+32 (other clusters do not have such data at present). Reduction details for **the Ks imaging** will be detailed in Nonino et al. (2019, in prep.).

Spitzer data reduction and flux extraction is similar to that of the *Spitzer* UltRa-Faint Survey Program (SURFSUP, Huang et al., 2016b). Full details, including treatment of ICL, will be described in detail in an upcoming catalog paper (Strait et al., 2019 in prep). Due to the broad point spread function (PSF) and low resolution ($0.6''$/pixel) of *Spitzer* images, we extract fluxes using T-PHOT (Merlin et al., 2015), designed to perform PSF-matched, prior-based, multi-wavelength photometry as described in Merlin et al. (2015, 2016). We do this by convolving a high resolution image (in this case, F160W) using a low resolution PSF transformation kernel that matches the F160W resolution to the IRAC (low-resolution) image and fitting a template to each source detected in F160W to best match the pixel values in the IRAC image.

We assess the trustworthiness of the output fluxes using diagnostic outputs $R_{3.6}$ and $R_{4.5}$ (see Table 3.1), defined as the ratio between the maximum value in the covariance matrix for a given source (i.e., the covariance with the object's closest or brightest source) and the source's own flux variance. Covariance indices $R_{3.6}$ and $R_{4.5}$ are indicators of whether a source is experiencing confusion with a nearby source. In the case of severe confusion and a high covariance index ($R_{3.6}$, $R_{4.5} > 1$), we perform a series of tests involving the input of simulated sources of varying brightnesses to test the confusion limit of that pair of sources. The only source with $R_{3.6}$, $R_{4.5} > 1$ in our sample is SPT0615-JD, and as described in S18, we find that simulated magnitudes brighter than ~ 25 can be safely recovered, and sources fainter than that have an additional 0.5 magnitude uncertainty. After testing the inclusion of this additional uncertainty, we conclude that the upper 1-σ bounds of SPT0615-JD are trustworthy as lower limits in magnitude (i.e., the flux of the source could be fainter than the extracted fluxes but not brighter).

3.2.3 Sample Selection

The selection criteria of all high-redshift ($z_{\text{peak}} \geq 5.5$) *HST*-selected RELICS objects is described in S20 **($z \sim 6 - 8$ candidates) and S18 ($z \sim 10$ candidate SPT0615-JD)**. This paper focuses on $z \sim 8$ candidates from the S20 sample and the $z \sim 10$ candidate from S18, that, when *Spitzer* fluxes are included in their photometry, still have $z_{\rm peak} \geq 7.5$. We find that the $z \sim 10$ candidate from S18 and six of the eight $z \sim 8$ candidates in S20 remain likely to be at $z \geq 7.5$ upon inclusion of *Spitzer* fluxes (Table 3.1). The other two $z \sim 8$ candidates from S20 (SPT0615-57-1048 and PLCKG287+32-2013) were moved into the $z \sim 7$ bin. We will explore these candidates in a future work.

3.3 Lens Models

In order to correct for magnification from lensing, relevant for SFRs and stellar masses, we use lens models created by the RELICS team. We use three lens modeling codes to produce the models for the clusters described here: `Lenstool` (Jullo & Kneib, 2009) for MACS0553-33 and SPT0615-57, Glafic (Oguri, 2010) for RXC0911+17, and a light-traces-mass method (LTM, Zitrin et al., 2013) for Abell S295, PLCKG287+32, and Abell 1763. Full details of the SPT0615-57 `Lenstool` model can be found in Paterno-Mahler et al. (2018), and the LTM models for Abell S295 and PLCKG287+32 are described in detail by Cibirka et al. (2018) and Zitrin et al. (2017), respectively.

The remaining three clusters will have details available in the future, and all models are available on MAST[3]. Our `Lenstool` model of MACS0553-33 uses nine multiply-imaged systems as constraints, three of which are spectroscopically confirmed including Ebeling et al., 2017 arc system 1, and our Glafic model of RXC0911+17 uses three multiply imaged systems with photometric redshifts as constraints.

We find no clear multiple image constraints in Abell 1763, but are able to make an approximate model for the cluster using the LTM method, which relies on the distribution and brightness of cluster galaxies. One should be cautious in interpreting magnifications in this field, however, because in the case of Abell 1763 where there are no visible constraints, we adopt a range of mass-to-light normalization using typical values from other clusters. Median magnifications for the high-z candidates are listed in Table 3.2, and treatment of their statistical uncertainties is described in §3.4.3.

---

[3] https://archive.stsci.edu/prepds/relics/

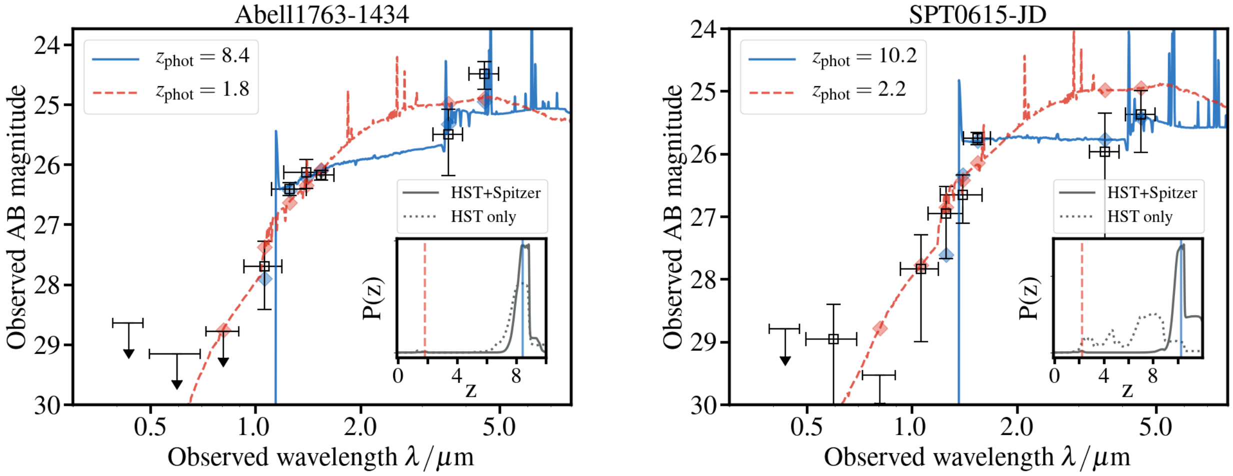

Figure 3.2: Best fit SEDs for Abell1763-1434 and SPT0615-JD, fit to BC03 templates assuming a constant star formation history (CSF), $0.02Z_\odot$ metallicity (m32), Lyman-α escape fraction $f_{\rm esc} = 20\%$, and small magellenic cloud dust law (SMC). Solid blue lines show best fit templates and dashed red lines show templates best fit at the associated low redshift peak in $P(z)$. Translucent blue diamonds show expected photometry for best fit and translucent red diamonds show expected photometry for low redshift fit. Inset: $P(z)$ calculated from EAzY while allowing for linear combinations of default base set of BC03 templates is shown. Solid gray line shows probability with HST and *Spitzer* fluxes, dotted gray shows probability with HST only fluxes. Vertical lines correspond to best fit and low redshift best fit solutions.

3.4 SED Fitting

3.4.1 Photometric Redshifts and Stellar Properties

To obtain a probability distribution function (PDF) and peak redshift, we use Easy and Accurate Redshifts from Yale (EAzY, Brammer et al., 2008), a redshift estimation code that compares the observed SEDs to a set of stellar population templates. For redshift fitting, we use the base set of seven templates from (Bruzual & Charlot, 2003, BC03), allowing linear combinations. EAzY performs a χ^2 minimization on a redshift grid, which we define to range from $z = 0.01 - 12$ in linear steps of $\Delta z = 0.01$, and computes a PDF from the minimized χ^2 values, where we assume a flat prior.

To calculate stellar properties of our candidates, we use a set of ~2000 stellar population synthesis templates, also from BC03, this time not allowing linear combinations. We assume a Chabrier initial mass function (Chabrier, 2003) between 0.1 and $100M_\odot$, metallicity of $0.02Z_\odot$, and constant star formation history. We allow age to range from 10 Myr to the age

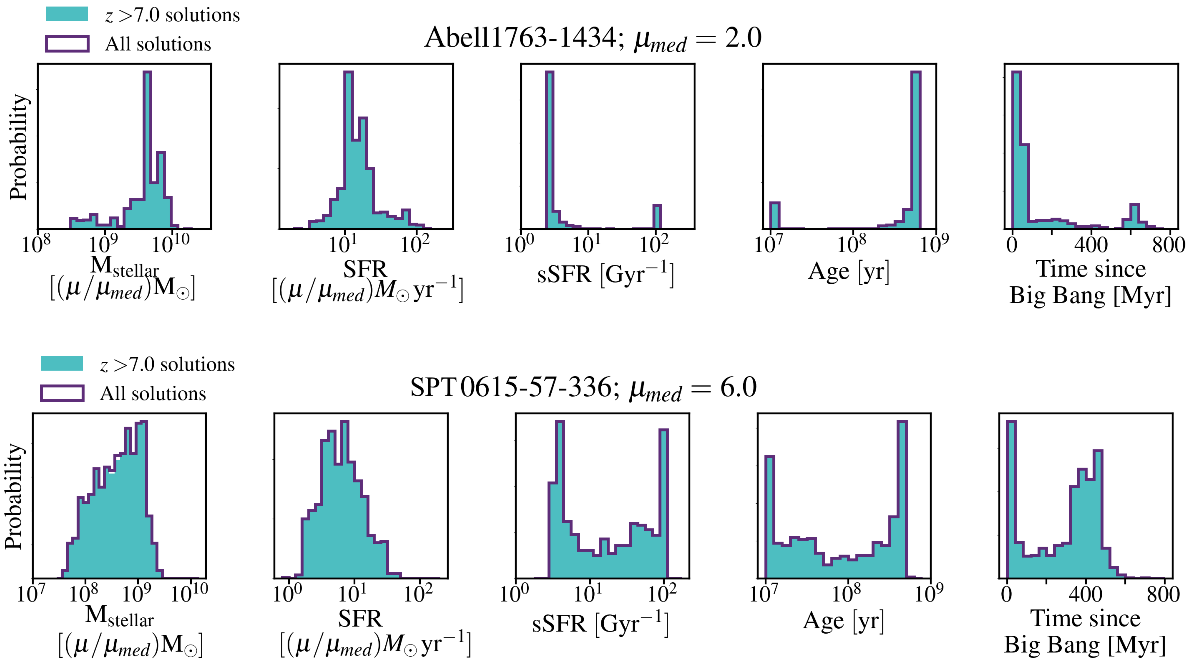

Figure 3.3: Distributions of stellar properties for Abell1763-1434 (top) and SPT0615-JD (bottom) explored by Monte Carlo simulation described in §3.4.3. From left to right, each panel shows stellar mass, star formation rate, specific star formation rate ($\mathrm{SFR}/M_{\mathrm{stellar}}$), age, and time since the Big Bang until the onset of star formation. High-redshift solutions are shown in turquoise and all solutions, including low redshift ones, are shown in purple outline. There is no significant distinction between the two as probability for low redshift is small. The redshifts explored by the MC simulation reflect the shapes of respective PDFs for each object in Figure 3.2.

of the universe at the redshift of the source. We assume the Small Magellanic Cloud dust law with $E_\star(B-V)$=$E_{\mathrm{gas}}(B-V)$ with step sizes of $\Delta E(B-V) = 0.05$ for $E(B-V) = 0 - 0.5$ mag and $\Delta E(B-V) = 0.1$ for $E(B-V) = 0.5 - 1$ mag.

Since it has been shown that nebular emission can contribute significant flux to broadband photometry (e.g., Schaerer & de Barros, 2010; Smit et al., 2014), we add nebular emission lines and continuum to the BC03 templates using strengths determined by nebular line ratios in Anders & Fritze-v. Alvensleben (2003) for a metallicity of $0.02Z_\odot$, where we calculate hydrogen recombination line strength using the relation from Leitherer & Heckman (1995), scaling from integrated Lyman-continuum flux. In addition, we include Ly-α, with expected strengths calculated using the ratio of H-α to Ly-α photons calculated for Case B recombination (high optical depth, $\tau \sim 10^4$) in Brocklehurst (1971), assuming a Ly-α escape fraction of 20%. While this is, perhaps, an overestimate at these redshifts (e.g., Hayes et al., 2010, though see Oesch et al., 2015 and Stark et al., 2017), we conservatively adopt this value to allow for a higher contribution from the Ly-α line. We describe calculation of statistical uncertainties with a Monte Carlo simulation in §3.4.3.

3.4.2 Biases and Systematic Uncertainties

Star formation history and initial mass function are known to introduce large systematic biases in age and SFR (Lee et al., 2009), although at high-z this is alleviated to some degree due to the fact that at $z \sim 8$, the universe is only ~750 Myr old (Pacifici et al., 2016). Since SFHs of our sources are not a known a priori, we made a choice to use a simple constant star forming model. Importantly, this may not be the most appropriate for high-redshift, star forming galaxies, so we also run our analysis using a suite of delayed tau models, which include an exponential component, for comparison. We find that there are no significant biases in age, and a 0.5 dex bias towards smaller stellar masses and SFRs when adopting a delayed tau SFH.

There is also a well-known degeneracy between dust, age, and metallicity parameters, so a lack of constraints on dust attenuation can lead to a large uncertainty (~0.5-1 dex) on SFR and stellar mass (Huang et al., 2016b). This is a particularly difficult degeneracy to break for objects at $z \sim 8$ because the SED near the UV slope is not well-sampled. We explore a subset of these biases in our own sample, largely finding what is reflected in the literature. We find that changing the assumed dust attenuation law from one with the shape of the SMC or Milky Way extinction law biases stellar masses and SFRs higher by ~ 0.5 dex. On the other hand, large changes in the metallicity ($0.02Z_{\odot}$ - $Z_{\odot}$) introduce subdominant systematic errors on SFR, stellar mass, or age ($\lesssim 0.1$ dex).

An additional uncertainty is the equivalent width distribution of nebular emission lines at high-z, particularly [OIII] + Hβ, which falls in *Spitzer*/IRAC [4.5] at $z \sim 8$. Strong emission lines ($\gtrsim 1000$Å) have the potential to boost broadband fluxes, as much or more than a strong Balmer break can boost the flux, potentially biasing stellar mass, sSFR and age (Labbé et al., 2013). While we do not fully explore the effects of this degeneracy, we do adopt standard assumptions with regards to emission lines (§3.4.1).

Table 3.2. Photometric Redshift and Stellar Population Modeling Results

Object ID	$z_{\rm peak}$[1]	$\mu_{\rm med}$[2]	M$_{\rm stellar}$[3] ($10^9 M_\odot$)	SFR[3] ($M_\odot {\rm yr}^{-1}$)	Age[4] (Myr)	sSFR[5] (Gyr^{-1})	E(B − V)[6] (mag)	M$_{1600}$[7] (mag)
Abell1763-0460*	$8.9^{+0.2}_{-0.8}$	$2.9^{+0.9}_{-1.0}$	$0.3^{+4.3}_{-0.2}(^{+0.2}_{-0.1})$	$1.2^{+10.4}_{-0.6}(^{+0.6}_{-0.3})$	510^{+60}_{-500}	$2.9^{+102.1}_{-0.3}$	$0.00^{+0.25}_{-0.00}$	$-18.4^{+0.3}_{-0.2}(^{+0.3}_{-0.5})$
Abell1763-1434	$8.2^{+0.6}_{-0.2}$	$2.0^{+0.5}_{-0.4}$	$4.3^{+2.4}_{-2.1}(^{+1.1}_{-0.7})$	$13.7^{+9.1}_{-4.0}(^{+3.4}_{-2.3})$	510^{+60}_{-190}	$2.9^{+1.5}_{-0.3}$	$0.10\pm^{0.05}_{0.00}$	$-20.2^{+0.2}_{-0.3}(^{+0.2}_{-0.2})$
AbellS295-0568*	$8.1^{+0.3}_{-0.7}$	$4.0^{+1.5}_{-0.4}$	$0.07^{+0.03}_{-0.02}(^{+0.01}_{-0.01})$	$2.4^{+2.2}_{-0.4}(^{+0.3}_{-0.7})$	28^{+13}_{-16}	$41.2^{+47.3}_{-11.9}$	$0.00^{+0.50}_{-0.00}$	$-19.4^{+0.2}_{-0.1}(^{+0.3}_{-0.1})$
MACS0553-33-219	$8.2^{+0.2}_{-2.4}$	$6.5^{+0.7}_{-0.6}$	$0.6^{+0.9}_{-0.5}(^{+0.1}_{-0.1})$	$1.8^{+2.5}_{-1.3}(^{+0.2}_{-0.2})$	570^{+240}_{-320}	$2.6^{+2.9}_{-0.7}$	$0.20^{+0.10}_{-0.20}$	$-17.9^{+0.8}_{-0.2}(^{+0.1}_{-0.1})$
PLCKG287+32-2032	$7.9^{+0.5}_{-0.9}$	36^{+12}_{-6}	$0.005^{+0.003}_{-0.002}(^{+0.001}_{-0.001})$	$0.2^{+2.5}_{-0.1}(^{+0.0}_{-0.1})$	31^{+9}_{-11}	$36.9^{+18.4}_{-7.7}$	$0.05^{+0.10}_{-0.05}$	$-16.5^{+0.4}_{-0.3}(^{+0.3}_{-0.2})$
RXC0911+17-0143	$8.1^{+0.4}_{-0.6}$	$1.5^{+0.2}_{-0.2}$	$0.2^{+0.8}_{-0.1}(^{+0.0}_{-0.0})$	$5.6^{+10.6}_{-1.4}(^{+0.9}_{-0.7})$	34^{+200}_{-20}	$33.9^{+71.0}_{-28.0}$	$0.00^{+0.05}_{-0.00}$	$-20.3^{+0.2}_{-0.1}(^{+0.1}_{-0.2})$
SPT0615-JD	$10.2^{+1.1}_{-0.5}$	$6.0^{+2.7}_{-1.7}$	$0.4^{+0.7}_{-0.3}(^{+0.2}_{-0.1})$	$6.2^{+6.9}_{-3.2}(^{+2.5}_{-1.9})$	80^{+320}_{-70}	$15.4^{+73.0}_{-11.9}$	$0.05^{+0.05}_{-0.05}$	$-19.8^{+0.2}_{-0.6}(^{+0.4}_{-0.4})$

---

[1] Peak redshift and 68% CL in PDF described in Section 3.2

[2] Median magnification factor found using corresponding lens model. $\mu_{\rm med}$ is assumed in SFR and M$_{\rm stellar}$ calculations.

[3] **Intrinsic stellar mass and SFR, assuming $\mu = \mu_{\rm med}$. Uncertainties include statistical 68% CLs from photometry and redshift. To use a different magnification value, multiply the quantity by $1/f_\mu$, where $f_\mu \equiv \mu/\mu_{\rm med}$.** In parentheses, 68% CLs from magnification only, assuming median M$_{\rm stellar}$ or SFR value.

[4] Time since the onset of star formation assuming a constant SFR

[5] Specific SFR, sSFR $\equiv M_{stellar}/$SFR

[6] Dust color excess of stellar emission. SMC dust law assumed.

[7] **Rest-frame 1600 Å magnitude assuming $\mu_{\rm med}$, derived from the observed F160W mag including a small template-based k-correction. Uncertainties include statistical 68% CLs from photometry and redshift. To use a different magnification value, use $\mathrm{M}_{(1600)} - 2.5\log(\mathrm{f}_\mu)$. In parentheses, 68% CLs from magnification only, assuming median F160W mag and $z_{\rm peak}$.**

* **Bright neighboring galaxy may cause additional uncertainty in *Spitzer* fluxes.**

3.4.3 Statistical Uncertainties

To understand the statistical uncertainties from photometry and redshift in the stellar properties, we perform a Monte Carlo (MC) simulation on each object. For each iteration, we sample from the redshift PDF **(calculated using EAzY default templates allowing linear combination, as described in §3.4.1)** and recompute the photometry for each band by Gaussian sampling from the estimated errors (Table 3.1). In the case of upper limits, we do not perturb the fluxes. For each of 1000 iterations we use EAzY to find a best fit template (from the template set for stellar properties described in §3.4.1) for the photometry, fixing the redshift to that which was sampled from the PDF on each iteration. The uncertainties on stellar properties reflect only statistical uncertainties and do not include systematic uncertainties associated with choices in initial mass function, star formation history, metallicity, dust law, or the Balmer break vs. emission line degeneracy.

Regarding the effect of magnification uncertainties on our stellar properties, since statistical uncertainties often underestimate the true uncertainties in magnification due to differences in model assumptions. Median systematic uncertainties from CLASH clusters are typically ∼20%, (Zitrin et al., 2015), although differences may be larger at larger magnifications (Meneghetti et al., 2017). We calculated the differences between models for the only cluster with multiple models available, SPT0615-57, and found that for SPT0615-JD, $\mu_{\rm med}$ ranged from 2.5-6.3. We report μ-scalable $M_{\rm stellar}$, SFR, and M_{1600} assuming our median magnification μ_{med}, with uncertainties from magnification on the quantity in parentheses in Table 3.2. To use a different magnification than is listed, one can multiply the appropriate μ-scalable value by $1/f_\mu$, where $f_\mu \equiv \mu/\mu_{med}$.

3.5 Results

The results from SED fitting and MC simulations are listed in Table 3.2 as the median and 1-σ statistical uncertainty on stellar properties for all objects. The redshift PDFs for all sources reflect that the high-redshift solution is preferred significantly more often than the low redshift solution in each case $(P(z < 7) < 1\%)$. We find a wide range of intrinsic stellar masses ($5 \times 10^6 M_\odot - 4 \times 10^9\ M_\odot$), star formation rates (0.2-14 $M_\odot$yr^{-1}), and ages (30-600 Myr) among the sample, and highlight, in particular, two objects showing a preference for an evolved stellar population, Abell1763-1434 and SPT0615-JD.

3.5.1 Abell1763-1434

The SED fitting and MC simulation results are shown in Figures 3.2 and 3.3. We find that Abell1763-1434 is a relatively massive galaxy with an evolved stellar population (∼500 Myr). Using the assumptions outlined in §3.4.1, we find a median intrinsic stellar mass of $4.3^{+2.4}_{-2.1} \times 10^9 M_\odot$ and median age of 510^{+60}_{-190} Myr (see Table 3.2 for uncertainties from μ). The distribution of the time since the Big Bang until the onset of star formation in that galaxy is shown in the rightmost panel of Figure 3.3, and implies that the oldest stars in this galaxy started forming < 100 Myr after the Big Bang. Abell1763-1434 prefers the oldest possible solution the large majority of the time: 73% of solutions prefer first star formation $<$100 Myr after the Big Bang, though we cannot exclude the possibility that abnormally strong nebular emission, large dust content, or some combination thereof could serve to decrease the estimated age.

We detect this source in *Spitzer*/IRAC [3.6] and [4.5] at 2-σ and 5-σ, respectively. In [4.5], the detection is significantly discrepant with the predicted photometry (∼2-σ) for the high-z solution (blue diamond in Figure 3.2). This could be indicative of a second, younger stellar population, high levels of dust, strong [OIII] emission, or some combination thereof. Assuming the boost in [4.5] is from strong [OIII]+Hβ, we increase the rest-frame equivalent width from our best-fit value of $\sim$ 215Å to ($\sim$ 1000Å). This exercise yields a 0.54 magnitude boost in [4.5], roughly the amount needed to match the detection. Thus, even with extreme [OIII]+H-β equivalent widths, we still require a significant Balmer break to fit the photometry well. We are not able to fully break this degeneracy with our current data, but possible improvements include sampling the UV slope with more broad/medium-band filters (e.g., Whitaker et al., 2011) to understand dust content, a spectroscopic redshift to mitigate redshift uncertainty, and a constraint on [OIII] equivalent width, perhaps using other emission lines such as CIII] (e.g., Maseda et al., 2017; Senchyna et al., 2017). Ultimately, *JWST* will allow us to measure continuum and emission lines to resolve the degeneracy.

3.5.2 SPT0615-JD

We find that SPT0615-JD is a typical galaxy with intrinsic stellar mass of $4.4^{+6.8}_{-3.1} \times 10^8 \mathrm{M}_\odot$, SFR of $6.2^{+6.9}_{-3.2} \mathrm{M}_\odot\ \mathrm{yr}^{-1}$, and a bimodal age distribution preferring either the oldest age solution possible or a younger population with first star formation ∼400 Myr after the Big Bang.

Assuming $z = 10.2$, the IRAC bands are uncontaminated by [OIII] + Hβ. The Balmer break, however, still remains fairly unconstrained due to confusion-limited *Spitzer* fluxes. We report a PDF with a small secondary peak, noting an insignificant probability of a low redshift solution ($< 1\%$). This source has two marginal detections (1–2-σ) in *Spitzer*/IRAC which we plot in Figure 3.2 as 1-σ lower limits in magnitude. These limits are tighter by 0.2 mag in [3.6] and 0.5 mag in [4.5] compared to fluxes reported in S18, a result of deeper data from our program that became available after the S18 analysis. This increases the probability of a high-z solution and strengthens the argument made in S18 that all low-z solutions require brighter *Spitzer* fluxes than our upper limits allow, and all high-z solutions are well-fit with fluxes fainter than the limits.

3.5.3 Other sources

For the remaining five sources, we find a range of masses, with the least massive being PLCKG287+32-2032 at an intrinsic stellar mass of $5^{+3}_{-2} \times 10^6 \mathrm{M}_\odot$. We report 1-$\sigma$ magnitude limits for non-detections in *Spitzer* for MACS0553-33-0219, PLCKG287+32-2032, and RXC0911+17-143 with the exception of a 3-σ detection in [3.6] for MACS0553-33-0219 (Table 3.1).

AbellS295-0568 and Abell1763-0460 are both likely contaminated with bright nearby sources, and their resulting stellar properties could be affected by systematic uncertainties not accounted for in error bars, including effects due to subtraction. The redshift solutions for these two sources are robust to variances in *Spitzer* fluxes, and even to excluding the *Spitzer* fluxes entirely.

3.6 Conclusions

We present SFRs, stellar masses, ages, and sSFRs for seven $z \gtrsim 8$ candidates from RELICS. All candidates have robust high-redshift solutions ($P(z > 7.5) > 0.95$) after the inclusion of *Spitzer*/IRAC [3.6] and [4.5] fluxes and are reasonably bright (≤ 27.8 magnitudes). We highlight, in particular, Abell1763-1434 which shows evidence for an evolved stellar population (~ 500 Myr) at a high best-fit redshift of $z = 8.2^{+0.6}_{-0.2}$, implying the onset of star formation < 100 Myr after the Big Bang. We also present a follow-up analysis of SPT0615-JD, the highest-redshift candidate from the RELICS sample at $z = 10.2^{+1.1}_{-0.5}$, also showing some evidence for an evolved stellar population. In both cases, a younger stellar population with extreme nebular emission, large dust content, or some combination thereof, could also explain the observed fluxes. While we cannot fully disentangle the degeneracies associated with SED fitting at $z \sim 8$, all candidates presented here have interesting stellar properties that would benefit from further study with *JWST*.

Acknowledgements

Based on observations made with the NASA/ESA Hubble Space Telescope, obtained at the Space Telescope Science Institute, which is operated by the Association of Universities for Research in Astronomy, Inc., under NASA contract NAS 5-26555. Observations were also carried out using Spitzer Space Telescope, which is operated by the Jet Propulsion Laboratory, California Institute of Technology under a contract with NASA.

MB and VS acknowledge support by NASA through ADAP grant 80NSSC18K0945, NASA/HST through HST-GO-14096, HST-GO-13666 and two awards issued by Spitzer/ JPL/Caltech associated with SRELICS_DEEP and SRELICS programs.

Chapter 4

Properties of $z \geq 5.5$ Galaxies

This chapter was originally published with the title *Properties of $z \geq 5.5$ Galaxies Inferred from Spitzer and Hubble Imaging, Including a $z \sim 6.8$ Strong [OIII] Emitter* in Volume 910 of *The Astrophysical Journal*.

We present constraints on the physical properties (including stellar mass, age, and star formation rate) of 207 $6 \lesssim z \lesssim 8$ galaxy candidates from the Reionization Lensing Cluster Survey (RELICS) and companion *Spitzer*-RELICS (S-RELICS) surveys. We measure photometry using T-PHOT and perform spectral energy distribution fitting using EAzY and BAGPIPES. Of the 207 candidates for which we could successfully measure (or place limits on) *Spitzer* fluxes, 23 were demoted to likely low redshift ($z < 4$). Among the remaining high redshift candidates, we find intrinsic stellar masses between $1 \times 10^6 \mathrm{M}_\odot$ and $4 \times 10^9 \mathrm{M}_\odot$, and rest-frame UV absolute magnitudes between -22.6 and -14.5 mag. While our sample is mostly comprised of $L_{UV}/L^*_{UV} < 1$ galaxies, there are a number of brighter objects in the sample, extending to $L_{UV}/L^*_{UV} \sim 2$. The galaxies in our sample span approximately four orders of magnitude in stellar mass and star-formation rates, and exhibit ages that range from maximally young to maximally old. We highlight 11 galaxies which have detections in *Spitzer*/IRAC imaging and redshift estimates $z \geq 6.5$, several of which show evidence for some combination of evolved stellar populations, large contributions of nebular emission lines, and/or dust. Among these is PLCKG287+32-2013, one of the brightest $z \sim 7$ candidates known (AB mag 24.9 at 1.6μm) with a *Spitzer* 3.6μm flux excess suggesting strong [OIII] + H-β emission ($\sim$1000Å rest-frame equivalent width). We discuss the possible uses and limits of our sample and present a public catalog of *Hubble* 0.4–1.6μm + *Spitzer* 3.6μm and 4.5μm photometry along with physical property estimates for all 207 objects in the sample. Because of their apparent brightnesses, high redshifts, and variety of stellar populations, these objects are excellent targets for follow-up with the *James Webb Space Telescope.*

4.1 Introduction

Properties of $z \gtrsim 6$ galaxies are interesting not only for piecing together the role of galaxies in reionization, the period of time in the universe when energetic photons ionized neutral hydrogen in the intergalactic medium (IGM), but also as the key building blocks in galaxy formation models. Galaxies in this epoch often reveal characteristics rarely seen in local galaxies. Average stellar properties of galaxies up to $z \sim 4-5$ have been reasonably well characterized; with access to a wealth of information from multiwavelength observations of characteristic galaxies, such as rest-frame optical and infrared (IR) data from Keck and Herchel for $z \sim 2-3$, and the Atacama Large Millimeter Array (ALMA) for $z \sim 1-5$, we have detailed accounts of basic physical properties such as star formation rate (SFR), stellar mass, and age, as well as metal enrichment and dust content for galaxies in this regime (e.g., Sanders et al., 2020; Duncan et al., 2020; Fudamoto et al., 2020). The picture becomes much less clear at higher redshifts, where due to intrinsic faintness of distant galaxies, increased absorption by the IGM, and the difficulty of obtaining red enough data to break degeneracies, we often have to rely on broadband imaging data and spectral energy distribution (SED) fitting for this information.

Broadband photometry and, in particular, *Spitzer*/Infrared Array Camera (IRAC) fluxes play an important role in measuring physical properties of galaxies at $z \gtrsim 6$. Because the rest-frame optical wavelengths are redshifted into the infrared in this regime, *Spitzer*/IRAC 3.6μm and 4.5μm ([3.6] and [4.5] hereafter) observations are necessary for constraints of stellar mass and age until *James Webb Space Telescope* (JWST) is functional.

There have been a multitude of studies using *Spitzer*/IRAC fluxes to probe the rest-frame optical wavelengths of high redshift galaxies. Notable examples include large surveys such as Hubble Frontier Fields (HFF, Lotz et al., 2017; Merlin et al., 2016; Castellano et al., 2016b; Di Criscienzo et al., 2017; Santini et al., 2017; Shipley et al., 2018; Bradač et al., 2019), Hubble Ultra Deep Field (HUDF, Yan et al., 2005; Eyles et al., 2005; Labbé et al., 2010), GOODS Re-ionization Era wide-Area Treasury from Spitzer (GREATS, Stefanon et al., 2019), Cluster Lensing and Supernova Survey with Hubble (CLASH, Postman et al., 2012; Bouwens et al., 2014), and Spitzer UltRa-Faint Survey (SURFSUP, Bradač et al., 2014; Ryan et al., 2014; Huang et al., 2016b). *Spitzer*/IRAC [3.6] and [4.5] broadband imaging has been integral to facilitate and contextualize high-impact discoveries, such as evidence of evolved stellar populations at $z > 8$ (Zheng et al., 2012; Huang et al., 2016b; Hashimoto et al., 2018; Mawatari et al., 2020; Strait et al., 2020b), discovery of the most distant spectroscopically confirmed galaxy, Gnz11 (Oesch et al., 2016), discovery of the highest-redshift Lyman-α detection (Smit et al., 2015; Zitrin et al., 2015; Oesch et al., 2015; Roberts-Borsani et al., 2016; Jung et al., 2020), measurement of nebular emission at $z \sim 4$ (Shim et al., 2011; Stark et al., 2013; Caputi et al., 2017; Bouwens et al., 2016; Faisst et al., 2016, 2019), and later measurement of nebular emission and stellar properties at $z > 5$ (Roberts-Borsani et al., 2016; Huang et al., 2016b; Stefanon et al., 2019; De Barros et al., 2019; Laporte et al., 2014; Bridge et al., 2019).

While the above surveys have established groundwork for observations of bright and faint galaxies at $z \gtrsim 6$, open questions centered around characterizing high-redshift populations remain. Ionization field, dust content, metal enrichment, and ionizing photon production are some examples of still mostly unknown quantities for a "normal" galaxy at $z \geq 5.5$. The answers to these unknowns will require significant spectroscopic followup time with existing and future telescopes.

In this work, we use *Spitzer*/IRAC observations to measure physical properties and identify the most interesting galaxies for future spectroscopic follow-up. Unique to this work is the use of gravitational lensing of a large number of galaxy clusters to probe the most apparently bright but perhaps intrinsically fainter high redshift sources. The Reionization Cluster Lensing Survey (RELICS, PI Dan Coe) and companion survey *Spitzer*-RELICS (S-RELICS), were designed to characterize the population of galaxies at these redshifts, and to attempt to find bright and rare galaxies at these epochs. To this end, these surveys image 41 massive clusters with *Hubble Space Telescope (HST)* imaging data from RELICS for all 41 of these clusters, which was used to select 321 $z \geq 5.5$ candidates (Salmon et al., 2020).

Here we add the S-RELICS *Spitzer*/IRAC imaging to further refine and characterize this sample.

The structure of the paper is as follows: We describe HST and Spitzer imaging data and photometry in Section 4.2, our SED modeling procedure and calculation of stellar properties in Section 4.3, and lens models used for correction to relevant stellar properties in Section 4.4. We present SED fitting results in Section 4.5 and we conclude in Section 4.7. Throughout the paper, we will give magnitudes in the AB system (Oke, 1974), and we assume a ΛCDM cosmology with $h = 0.7$, $\Omega_m = 0.3$, and $\Omega_\Lambda = 0.7$. Equivalent widths are quoted in the rest-frame.

4.2 Observations and Photometry

All imaging data used for this analysis were obtained through a combination of RELICS and archival data. Each cluster was observed with *HST* and *Spitzer* and was reduced in a way that optimizes the search for high-z galaxies. Here we briefly summarize the observing strategy of the survey, but in depth information about observations can be found on the RELICS website[1] and in the RELICS overview paper (Coe et al., 2019). Images of selected *HST* and bands and both *Spitzer* channels for the $z \geq 6.5$, IRAC-detected sample are shown in Figure 4.1.

4.2.1 HST

Each cluster was observed with two orbits of Wide Field Camera 3/ Infrared (WFC3/IR) imaging split among the F105W, F125W, F140W, and F160W filters, and three orbits of Advanced Camera for Surveys (ACS) split among F435W, F606W, and F814W (minus archival optical imaging), for a total of 188 *HST* orbits. Several clusters had archival ACS and/or WFC3 imaging in other filters (F390W, F475W, F555W, F625W, F775W, F850LP, F110W) and some clusters which received additional data from a subsequent proposal. Most clusters reach approximate *HST* 3-σ depths of $\sim$ 27 mag in ACS bands and $\sim$ 26 mag in WFC3 bands.

In this paper, we use the catalogs based on a detection image comprised of the 0.06"/pixel weighted stack of all WFC3/IR imaging (to optimize the search for high-z galaxies), de-

---

[1] https://relics.stsci.edu/

scribed in Coe et al. (2019) and available on MAST[2].

4.2.2 Spitzer Data and Photometry

Spitzer/Infrared Array Camera (IRAC) images for all clusters come from a combination of S-RELICS (*Spitzer*-RELICS, PI Bradač #12005, 13165, 13210), Director's Discretionary Time (PI Soifer #12123), for a total of over 1000 hours of exposure time, and additional archival data. 13 clusters that had promising $z \sim 8$ targets received deeper data via a follow-up proposal, to reach a total of 30 hours exposure time per band (3-σ depth ∼26 mag) in each channel. All clusters reach a total of 5 hours of exposure time (3-σ depth ∼24 mag) in each of IRAC channels 1 and 2 ([3.6] and [4.5]). A complete accounting of *Spitzer* data can be found in Table 4.1 and all shallow images are available on IRSA[3]. All raw data are available for download on the *Spitzer* Heritage Archive (SHA[4]).

---

[2] https://archive.stsci.edu/prepds/relics/

[3] https://irsa.ipac.caltech.edu/data/SPITZER/SRELICS/

[4] https://sha.ipac.caltech.edu/applications/Spitzer/SHA/

Table 4.1. Exposure Times and Programs of Spitzer data

Cluster	RA[1]	Dec[1]	Exposure Time	Program[*]
PLCKG004-19	19:17:4.50	−33:31:28.5	30, 30 hours	13165, 12005, 12123
SPT0615-57	06:15:54.2	−57:46:57.9	30, 30 hours	80012, 12005, 12123, 13210
CL0152-13	01:52:42.9	−13:57:31.0	30, 30 hours	17, 20740, 50726, 70063, 12005, 12123
ACT0102-49	01:02:53.1	−49:14:52.8	30, 30 hours	70149, 12123, 12005, 14017
PLCKG287+32	11:50:50.8	−28:04:52.2	30, 30 hours	12123, 13165, 12005
PLCKG308-20	15:18:49.9	−81:30:33.6	30, 30 hours	12123, 12005, 14017, 14253
MS1008-12	10:10:33.6	−12:39:43.0	30, 30 hours	12005, 12123, 14017
RXS0603+42	06:03:12.2	+42:15:24.7	30, 30 hours	12005, 12123, 14017
SMACS0723-73	07:23:19.5	−73:27:15.6	30, 30 hours	12123, 12005, 14017
Abell1763	13:35:18.9	+40:59:57.2	30, 30 hours	12123, 13165, 12005
MACS0553-33	05:53:23.1	−33:42:29.9	30, 30 hours	90218, 12005, 12123, 14281
MACS0257-23	02:57:10.2	−23:26:11.8	5, 5 hours	60034
RXC0600-20	06:00:09.8	−20:08:08.9	5, 5 hours	12005, 12123, 90218
MACS0025-12	00:25:30.3	−12:22:48.1	5, 5 hours	60034
Abell2163	16:15:48.3	−06:07:36.7	9, 9 hours	50096, 12005, 12123, 14242
Abell1758	13:32:39.0	+50:33:41.8	6, 6 hours	83, 60034
RXC0018+16	00:18:32.6	+16:26:08.4	5, 5 hours	12005, 83, 12123
Abell520	04:54:19.0	+02:56:49.0	10, 10 hours	12005, 12123
MACS0308+26	03:08:55.7	+26:45:36.8	5, 5 hours	12005, 12123
RXC0911+17	09:11:11.4	+17:46:33.5	30, 30 hours	60034, 14281
Abells295	02:45:31.4	−53:02:24.9	30, 30 hours	70149, 12005, 12123, 14281
Abell665	08:30:57.4	+65:50:31.0	7, 5 hours	12005, 12123, 14253
Abell3192	03:58:53.1	−29:55:44.8	5, 5 hours	12123, 12005,
PLCKG209+10	07:22:23.0	+07:24:30.0	5, 5 hours	12123, 12005
Abell2537	23:08:22.2	−02:11:32.4	5, 5 hours	60034, 41011
SPT0254-58	02:54:16.0	−58:57:11.0	5, 5 hours	12123, 12005
RXC0142+44	01:42:55.2	+44:38:04.3	5, 5 hours	12123, 12005
Abell1300	11:31:54.1	−19:55:23.4	7, 5 hours	12005, 12123, 14253, 14242
MACS0159-08	01:59:49.4	−08:50:00.0	7, 5 hours	12005, 12123, 14253

Table 4.1 (cont'd)

Cluster	RA[1]	Dec[1]	Exposure Time	Program[*]
MACS0035-20	00:35:27.0	−20:15:40.3	5, 5 hours	12123, 12005
WHL0137-08	01:37:25.0	−08:27:25.0	7, 5 hours	12123, 12005, 14253
Abell697	08:42:58.9	+36:21:51.1	5, 6 hours	83, 60034, 14130, 14253
PLCKG138-10	02:27:06.6	+49:00:29.9	5, 5 hours	12123, 12005
PLCKG171-40	03:12:56.9	+08:22:19.2	7, 5 hours	12123, 12005, 14253
RXC0032+18	00:32:11.0	+18:07:49.0	5, 5 hours	12123, 12005, 90218
RXC0232-44	02:32:18.1	−44:20:44.9	7, 5 hours	12123, 12005, 14253
RXC0949+17	09:49:50.9	+17:07:15.3	5, 5 hours	12123, 12005
RXC1514-15	15:15:00.7	−15:22:46.7	5, 5 hours	12123, 12005, 14253
RXC2211-03	22:11:45.9	−03:49:44.7	6, 5 hours	90218, 12005, 12123, 14253
Abell2813	00:43:25.1	−20:37:14.8	7, 5 hours	60034, 14253
MACS0417-11	04:17:33.7	−11:54:22.6	5, 5 hours	12123, 12005, 90218

[1] RAs and Decs correspond to cluster centers.

[*] Program IDs included in our reduction. ID #12005, 13165, 14281, 13165, 13210, 14017: PI Maruša Bradač. #12123: PI Tom Soifer, #60034, 90218 PI Eiichi Egami, #14253 PI Mauro Stefanon, #14242 PI Andra Stroe, #50096 PI Paul Martini, #70149 PI Felipe Menanteau, #83 PI George Rieke, #14130 PI Rychard J Bouwens, #17 PI Giovanni Fazio, #20740, 50726, 70063 PI Bradford P Holden, #80012 PI Mark Brodwin

4.2.2.1 Reduction

To reduce and mosaic *Spitzer* images, we closely follow the process described by Bradač et al. (2014) for the SURFSUP survey, which also consists of IRAC images used for a search of high-z galaxies. Briefly, we begin downloading the corrected-basic calibrated data (cBCD) from the SHA. The cBCDs have been processed by the IRAC pipeline to remove instrumental artifacts, and to calibrate into physical units (MJy sr^{-1}). We apply additional mitigation measures using custom scripts; specifically, we correct for the warm-mission column pull-down (using bandcor_warm.c by M. Ashby) and muxstriping (using automuxstripe.pro by J. Surace) that often occurs when bright sources are present (these scripts are located on the

Abell1758-1942

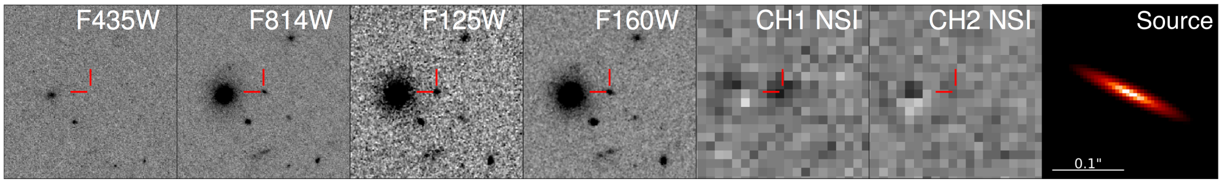

Abell1763-1434

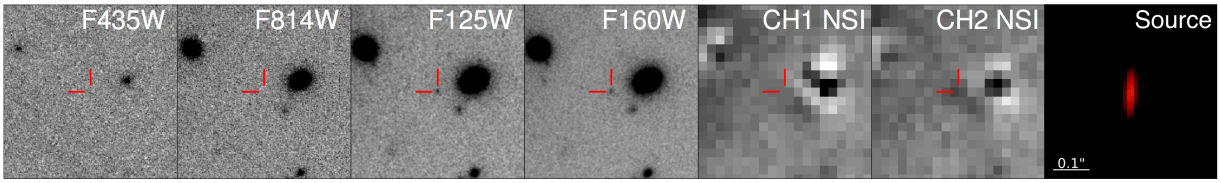

ACT0102-49-2391

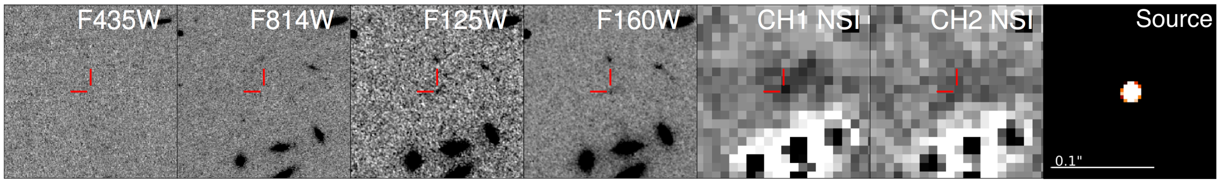

ACT0102-49-2551

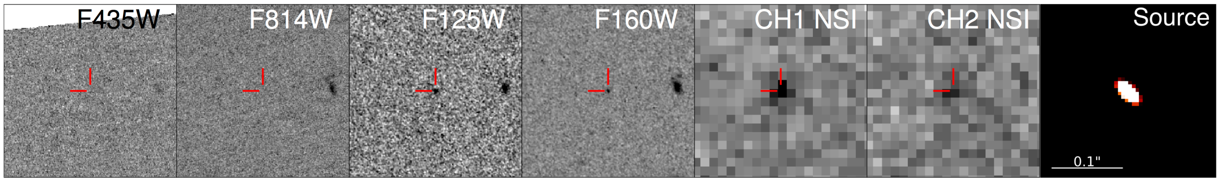

CL0152-13-191

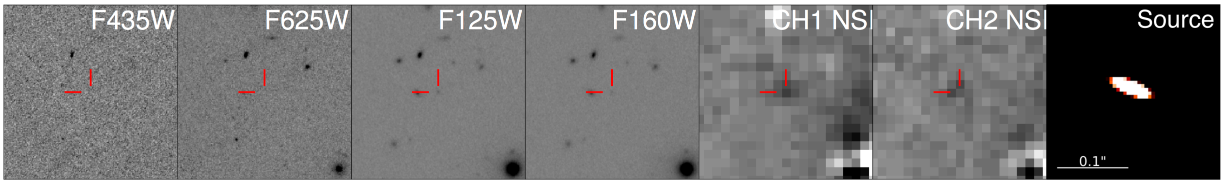

MACS0053-33-219

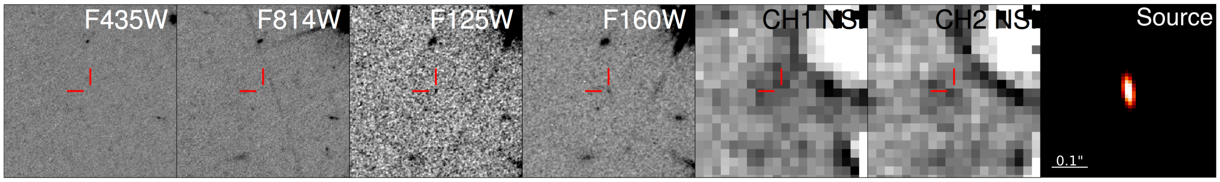

PLCKG287+32-698

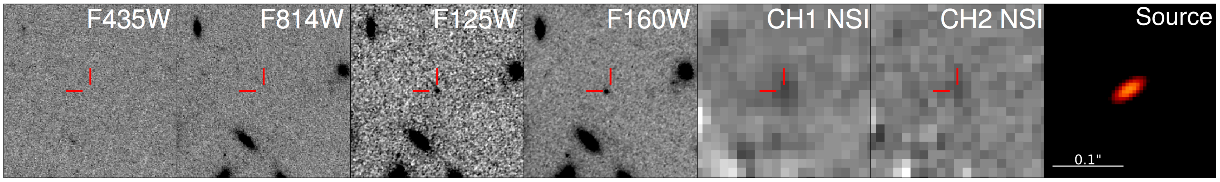

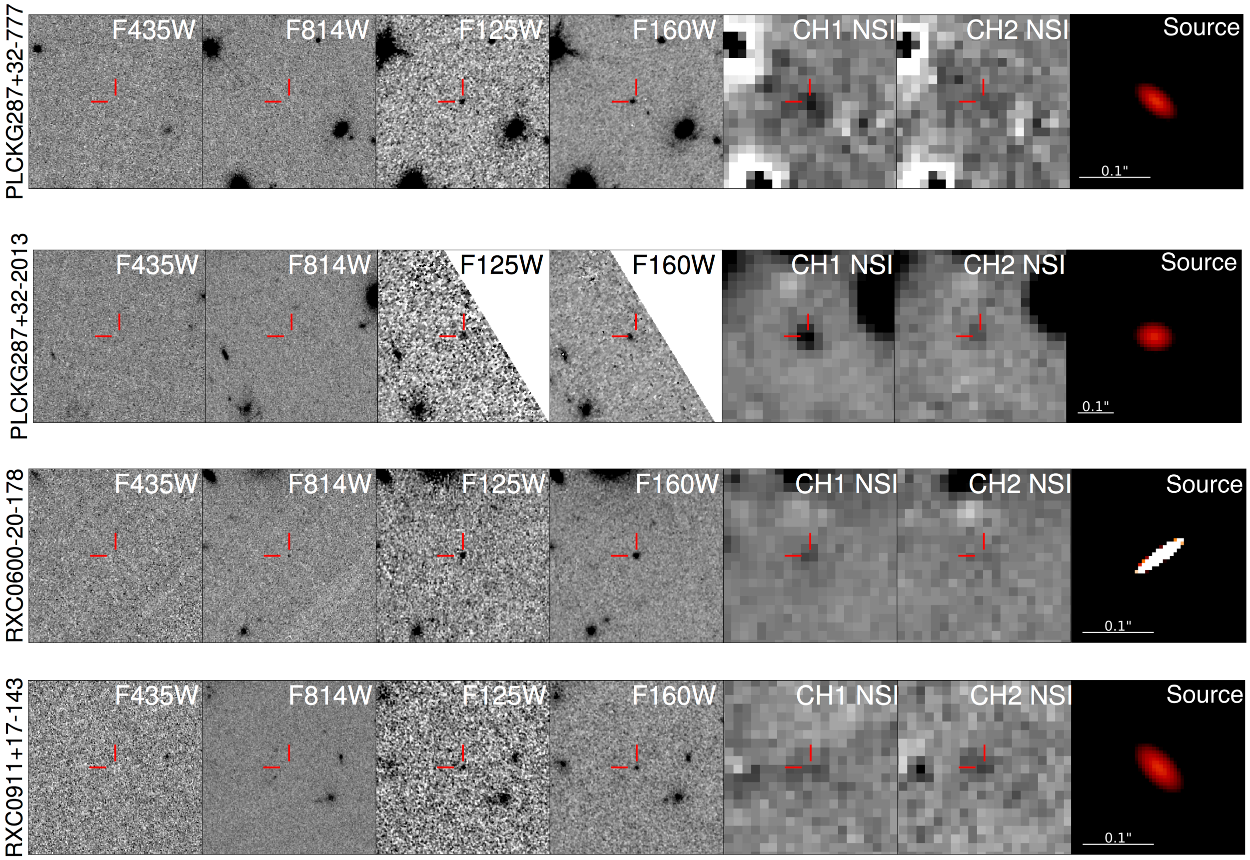

Figure 4.1: *HST* images and *Spitzer*/IRAC neighbor-subtracted images (NSIs) for each of the 11 galaxies that have both a best fit redshift of $z \geq 6.5$ and at least one *Spitzer*/IRAC detection. From left to right, F435W, F814W or F850LP (ACS, where $z > 7$ galaxies should not be detected), F125W, F160W (WFC3/IR), and Ch1, Ch2 of *Spitzer*. The cutouts are 12"x12", and the object is centered near the red tick marks in all but the right-most panel. The rightmost panel is the resulting delensed source in the source plane of the galaxy with a 1" size bar for comparison.

IRAC Cookbook website[5]). To create the mosaic images we use the MOsaicker and Point source EXtractor (MOPEX) command-line tools and largely follow the process described in the IRAC Cookbook for the COSMOS medium-deep data. The corrected frames are background-matched using the overlap.pl routine from MOPEX and then drizzle-combined into a mosaic using the mosaic.pl routine. The final mosaics have a pixel scale of 0.6”pix^{-1} and a pixel fraction of 0.1. As a last step, we use the `Tweakreg` routine from `DrizzlePac`, which compares the positions of bright objects in *Spitzer* and *HST* images, to correct for any shifts in relative astrometry.

4.2.2.2 Flux Extraction and Error Analysis

Intracluster light (ICL) subtraction, background subtraction, and flux extraction is done using T-PHOT (Merlin et al., 2015), designed to perform PSF-matched, prior-based, multi-wavelength photometry on low-resolution imaging as described by Merlin et al. (2015, 2016). This is done by convolving cutouts from a high resolution image (in the case of this work, *HST*/WFC3 F160W) using a low resolution PSF transformation kernel that matches the high-resolution image to the low-resolution (in our case, [3.6] and [4.5]) image. T-PHOT then fits a template to each source detected with HST and convolves the template with a PSF transformation kernel to match the resolution to that of the IRAC image. T-PHOT then solves for the solution where the model image created from the convolved *HST* image best matches the pixel values in the real IRAC image and outputs fluxes for each template. We use the F160W image and WFC3/IR total weighted segmentation map as the priors for T-PHOT. Because T-PHOT takes a template-fitting approach where all templates are solved for simultaneously, an approach designed for blank fields which have a zero mean background, we fit each high-z candidate separately, running T-PHOT on a small FOV centered on the candidate, to account for the changing background and ICL in a cluster field. Within the 12” ($\sim$ 70 kpc for cluster redshift of $z = 0.4$) FOV on which we run T-PHOT, the background shows minimal variation: in most cases, where the object is far from the cluster center, we see no variation in background (i.e., the variation is centered on zero and random), while this can reach as high as $\sim 20\%$ where ICL is denser near the

---

[5] https://irsa.ipac.caltech.edu/data/SPITZER/docs/dataanalysistools/cookbook/

cluster center. For these reasons, and due to the fact that most of our galaxies are far from the cluster center where ICL is not dense, further ICL modeling and subtraction are not necessary in addition to subtracting background.

While T-PHOT is useful for predicting fluxes of objects with potential blending, it does not account for this blending in its output uncertainties. However, it calculates a covariance matrix which includes the covariance between each object and every other object in the image. This can be used to calculate a maximum covariance index ($\mathrm{R}_{[3.6],[4.5]}$), which is the ratio of the covariance of an object with its closest or brightest neighbor and its own variance. If this value is higher than 1, the object is severely blended with a neighbor and caution should be taken interpreting fluxes. We report the $\mathrm{R}_{[3.6],[4.5]}$ values with the fluxes in Table 4.3 and include them in the catalog for all sources in the sample.

In practice, T-PHOT does not work as well near bright sources and the cluster center, creating artifacts in the residual (see several objects in Figure 4.1). For this reason, we only include fluxes in this work for which we believe we are able to reliably extract *Spitzer* fluxes, meaning the residual on top of the high-z candidate is not a residual artifact due to a bright nearby source. To ensure T-PHOT is not underestimating flux uncertainties, we calculate our own statistical uncertainties for each source. In the residual image, we measure background levels 100 times within 3" of each high-z candidate, avoiding artifacts from neighboring objects. The mean should fall close to zero, and we take the standard deviation as the error. In most cases, this error is smaller than the error reported by T-PHOT, however in some cases it is larger. In those cases, we use the larger uncertainty.

The PSF and convolution kernel used to convolve prior HST images to the resolution of IRAC images are important for this process. We create a PSF by stacking point sources, identified with a Source Extractor (Bertin & Arnouts, 1996) run with the following parameters: `DEBLEND_MINCONT` $= 10^{-7}$, `MINAREA` $= 9$, `DETECT_THRESH` $= 2$, and `ANALYSIS_THRESH` $= 2$. We select point sources using the stellar locus in `FLUX_RADIUS` vs. `MAG_AUTO` space for every object in the IRAC image (not just in the *HST* FOV). After the point sources are selected, we further require that their axis ratio is > 0.9 and that they are sufficiently separated from neighbors to have a secure centroid. We recompute the PSF centroids by fitting a Gaussian profile to the inner profile ($r < 4$ pixels), and align the point sources using sinc interpolation.

Table 4.2. Properties of SED Fitting Methods

	Method A	Method B
Software	EAzY	BAGPIPES
Redshift	0 – 12	4 – 11
Formation age	10Myr – age of universe	1 Myr – age of universe
Metallicity	$0.2Z_\odot$	$0.005 - 5\ Z_\odot$
Ionization log(U)	not known *a priori*	-4 – -1
Dust	SMC, E(B-V) = 0 – 1	Calzetti, $A_V = 0 - 3$mag[1]
Templates	BC03+nebular emission	BPASS+CLOUDY nebular emission

[1] 2x more dust surrounding HII regions for their first 10 Myr

At each phase we subtract the local background and normalize the flux of the point source to one. We sigma-clip average the masked, registered, normalized point sources and do one further background correction to ensure the convolutions with T-PHOT are flux conserving. Our stacked PSFs are consistent with the IRAC handbook[6], and each of our clusters' PSFs contains at least 40 point sources per IRAC channel. In practice, the PSF convolution kernel needs to be "sharpened" to produce cleaner residuals. For each individual high-z candidate, we experiment with increasing and decreasing the weight of the core of the PSF to produce the cleanest residual. Most of the time, this means decreasing the weight of the core by a factor of 0.8-0.9.

4.2.2.3 Rejected Objects

Of the 321 HST-selected high-redshift sample, we were able to extract reliable *Spitzer* fluxes for 207 galaxies. The remaining

4.3 Estimating Galaxy Properties

Throughout this work, we will refer to two separate methods for estimating physical properties of galaxies. Method A is our primary routine which we use in order to compare to

---

[6] https://irsa.ipac.caltech.edu/data/SPITZER/docs/irac/iracinstrumenthandbook/

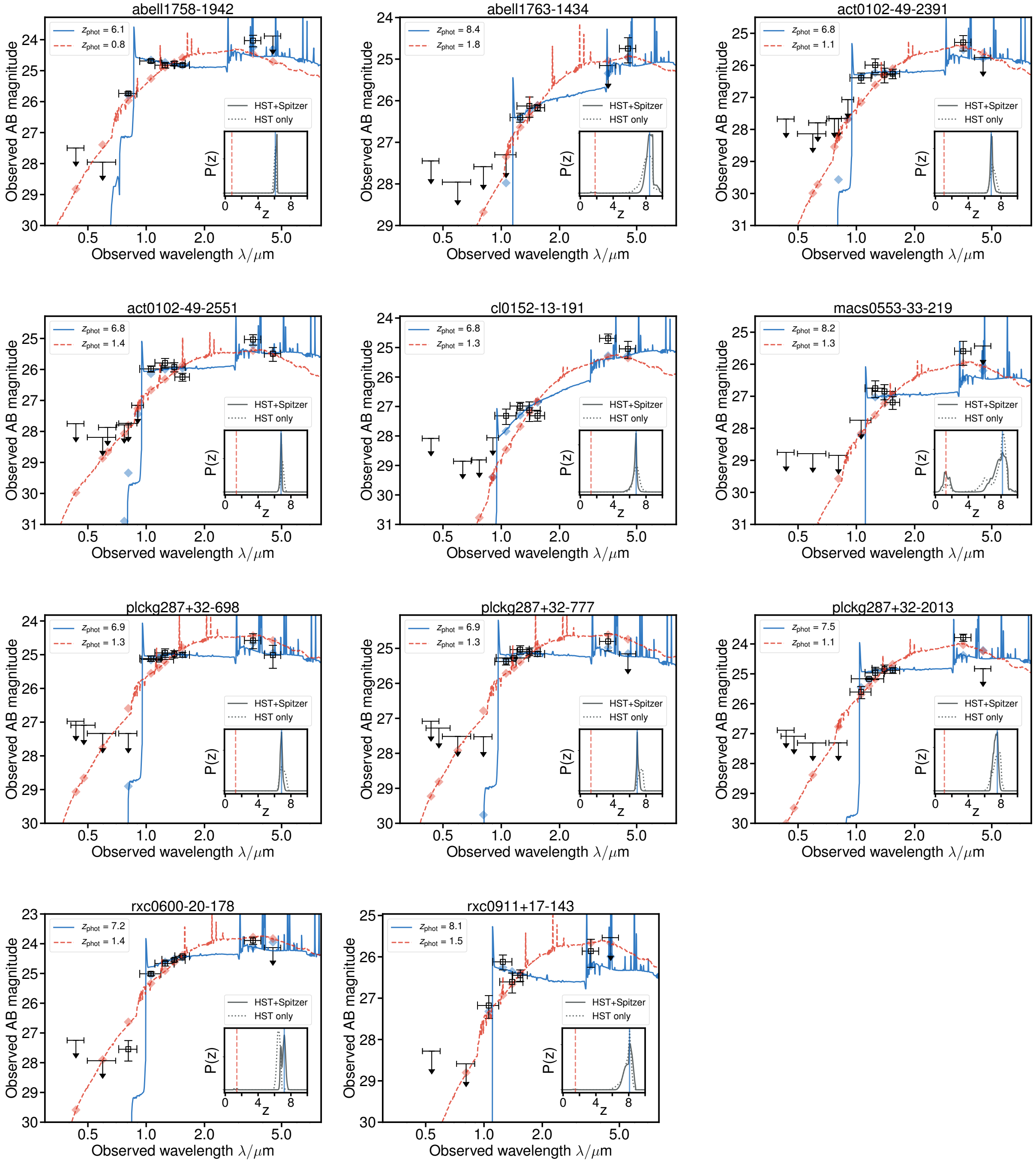

Figure 4.2: The SEDs and best-fit templates from the Method A SED fitting described in Section 4.3 for each of the 11 galaxies which have both $z \geq 6.5$ and at least one detection in *Spitzer*/IRAC. Data are shown as black squares with error bars, and predicted photometry from models are shown as red and blue translucent diamonds. Upper limits for HST and Spitzer are at the 3-σ level. Blue template is the object's best-fit high redshift ($z > 4$) template; red template is the object's best-fit template at the secondary peak in the redshift PDF (or where it would be if there is not one). **Inset:** Redshift PDF; dotted line is using HST only (as in Salmon et al., 2020) and solid line is PDF using *HST* and *Spitzer* fluxes.

previous similar works (e.g., Huang et al., 2016b; Bradač, 2020). We mainly refer to results from Method A in this work (e.g., the values in Table 4.4, results in Figures 4.2 and 4.6). Method B is a secondary routine which we will use for comparison purposes in Figures 4.3 and 4.4, as well as discussion of biases and uncertainties in our analysis (Section 4.3.3), and in the exploration of the six objects we discuss in detail in Section 4.5. We report results from both analyses in the attached catalog (see Section 4.5.2.)

4.3.1 Method A

In our primary SED fitting method, we first fit for redshift, and then use the resultant redshift posterior when fitting for other properties. We start by calculating colors from HST and IRAC imaging to estimate a redshift probability distribution function (PDF) for each source using the redshift estimation code Easy and Accurate Redshifts from Yale (EAzY, Brammer et al., 2008). This code compares the observed SEDs to a set of stellar population templates. Using linear combinations of a base set of templates from Bruzual & Charlot (2003, BC03) and no priors on magnitude, EAzY performs χ^2 minimization on a user-defined redshift grid, which we define to range from $z = 0.1 - 12$ in linear steps of $\delta z = 0.1$, and computes a PDF from the minimized χ^2 values. We use this PDF to calculate best-fit redshift and uncertainties, but opt for a slightly different process to calculate stellar properties.

To calculate stellar properties, we sample from the redshift PDF (we do not fix a redshift) and our photometry assuming a normal error distribution 1000 times, each time finding a best fit template, again with EAzY. In order to be able to extract physical properties associated with each template, we do not allow linear combination of templates during this stage of SED fitting. We use a set of ∼2000 stellar population synthesis templates from the updated BC03 templates from 2016[7], assuming the following: a Chabrier initial mass function (IMF, Chabrier, 2003) between 0.1 and 100 $M_\odot$, a metallicity of 0.2 $Z_\odot$, a constant star formation history (SFH), a Small Magellenic Cloud (SMC) dust law (Prevot et al., 1984) with $\mathrm{E_{stellar}}$(B-V)=$\mathrm{E_{nebular}}$(B-V) with step sizes of ΔE(B-V)=0.05 for 0-0.5 mag and 0.1 for 0.5-1 mag. We allow formation age (the age from when the first stars in the galaxy formed) to range from 10 Myr to the age of the universe at the redshift of the source. In Section

---

[7] http://www.bruzual.org/ gbruzual/bc03/

4.3.3, we discuss the motivations behind these assumptions and the biases and uncertainties that come from our choices.

We also include nebular emission lines and continuum to account for the role these can have in contributing to broadband fluxes (Schaerer & de Barros, 2010; Smit et al., 2014). To do this, we first calculate hydrogen recombination line strength following the relation from Leitherer & Heckman (1995), scaling from integrated Lyman-continuum flux, and then follow the strengths determined with nebular line ratios by Anders & Fritze-v. Alvensleben (2003). We also include Lyman-α, calculating expected strengths using the ratio with H-α and assuming a Case B recombination in Brocklehurst (1971) with a Ly-α escape of 20%.

4.3.2 Method B

For our secondary method of estimating galaxy properties, we use the program Bayesian Analysis of Galaxies for Physical Inference and Parameter EStimation (BAGPIPES, Carnall et al., 2018). Instead of the default BC03 models, we implemented the Binary Population and Spectral Synthesis (BPASS v2.2.1, Eldridge & Stanway, 2009) templates, reprocessed to include nebular continuum and emission lines using the photoionization code `CLOUDY` c17.01 (Ferland et al., 2017). BAGPIPES fits redshift in parallel with physical properties of galaxies using the MultiNest nested sampling algorithm (Feroz & Hobson, 2008; Feroz et al., 2009; Feroz & Skilling, 2013) to navigate the multi-dimensional space of physical parameters. For this work, we implement an exponential SFR with flexibility to rise, stay constant, or decline:

$$SFR(t) \propto e^{-t/\tau}, \tag{4.1}$$

$$\tau = \frac{t_{obs} - t_{form}}{\tan(R\pi/2)}, \tag{4.2}$$

for a galaxy observed at time t_{obs} that began forming stars at time t_{form}. The parameter R dictates the rate of increase, ranging from -1 (maximally old burst), through negative fractional values (declining), 0 (constant), positive (increasing), to $+1$ (maximally young burst). We use the BPASS IMF `imf135_300`: Salpeter slope $\alpha = -2.35$ between 0.5 and 300 $M_{\odot}$ and shallower $\alpha = -1.3$ for lower mass stars 0.1 – 0.5 $M_{\odot}$. Dust in BAGPIPES assumes a functional form described by the Calzetti Law (Calzetti et al., 2000), and we assign twice as much dust around HII regions as in the general ISM in the galaxy's first 10 Myr. We allow dust extinction to range from $A_V = 0$ to 3 magnitudes. We vary metallicity in log space from 0.005 to 5 $Z_\odot$ and allow ages of formation from 1 Myr to the age of the universe. These parameters are summarized in Table 4.2, and biases and uncertainties are discussed in Section 4.3.3.

We reprocess the BPASS stellar continuum spectra using `CLOUDY`. Hydrogen and helium scale factors, as well as other model details, are listed in Eldridge & Stanway (2009). We allow the ionizaton parameter $\log(U)$ to vary from -4 to -1, allowing a very large dynamic range of H-β[OIII]λ4959,5007Å (EW can be $>$ 10000Å for the most extreme ionization conditions).

4.3.3 Biases and Uncertainties

The biases and uncertainties associated with SED fitting have been well-documented (e.g., Papovich et al., 2001; Shapley et al., 2001; Lee et al., 2009; Salmon et al., 2015; Carnall et al., 2018; Leja et al., 2019), and we further explore in this section considerations relevant to properties of our sample presented in this work.

4.3.3.1 Star Formation Histories

While there have been studies on the effect of SFH on inferred galaxy properties at lower redshift ($z < 2$, e.g., Pacifici et al., 2016; Carnall et al., 2018; Leja et al., 2019; Lower et al., 2020), few studies have focused on the very high redshift regime we consider. The lower-redshift studies show that a bias can be introduced in stellar mass, SFR and age from a choice of any parameterized SFH model (e.g., exponential or constant), due to the intrinsically bursty and stochastic nature of star formation. Specifically, Carnall et al. (2019) find that stellar mass, SFR and mass-weighted age vary with the choice of SFH model for mock photometry at $z = 0$ by at least 0.1, 0.3 and 0.2 dex, respectively. Furthermore, they find that, generally, photometric data alone cannot discriminate between SFH models. While the need to constrain SFHs may be somewhat alleviated at very high redshifts, as the universe has only had ~750 Myr to form galaxies at $z \sim 8$, the very beginning of SFHs leave little imprint on a galaxy's SED, making it difficult to fully constrain. For this reason, we distinguish between formation age and mass-weighted age. We define formation age as $t_{obs} - t_{form}$, or the age of a galaxy observed at time t_{obs} since it first started forming stars at time t_{form}. While this is a useful parameter for constraining the beginning of galaxy

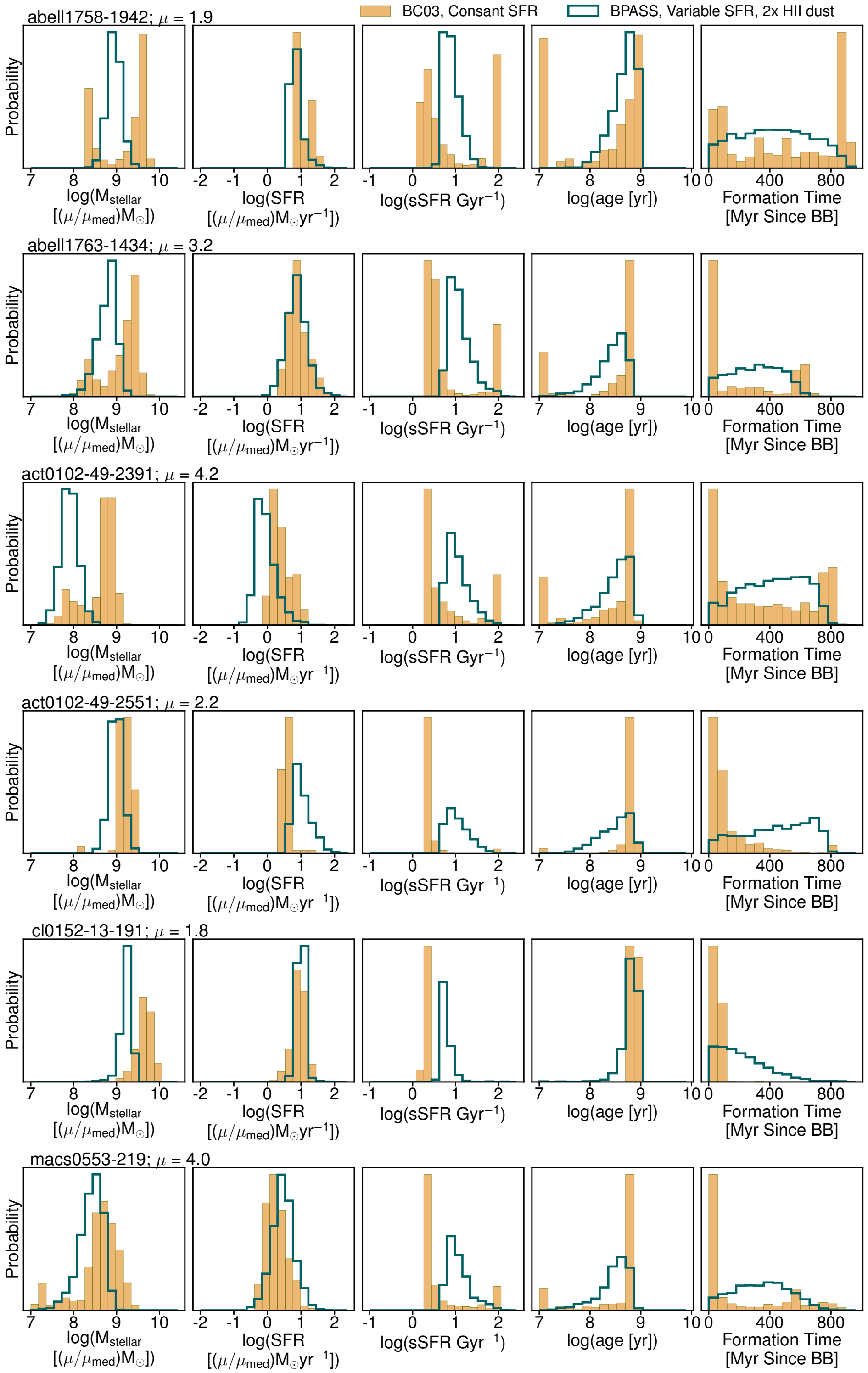

Figure 4.3: Results of SED fitting for the first 6 of 11 objects in the sample which had both a redshift of at least $z \geq 6.5$ and at least one detection in *Spitzer*/IRAC. In yellow/tan filled histograms, the distribution of stellar mass, SFR, sSFR, age, and formation time resulting from Method A, and dark green open histograms show the distribution of the same properties resulting from Method B. These are described in full in Section 4.3.

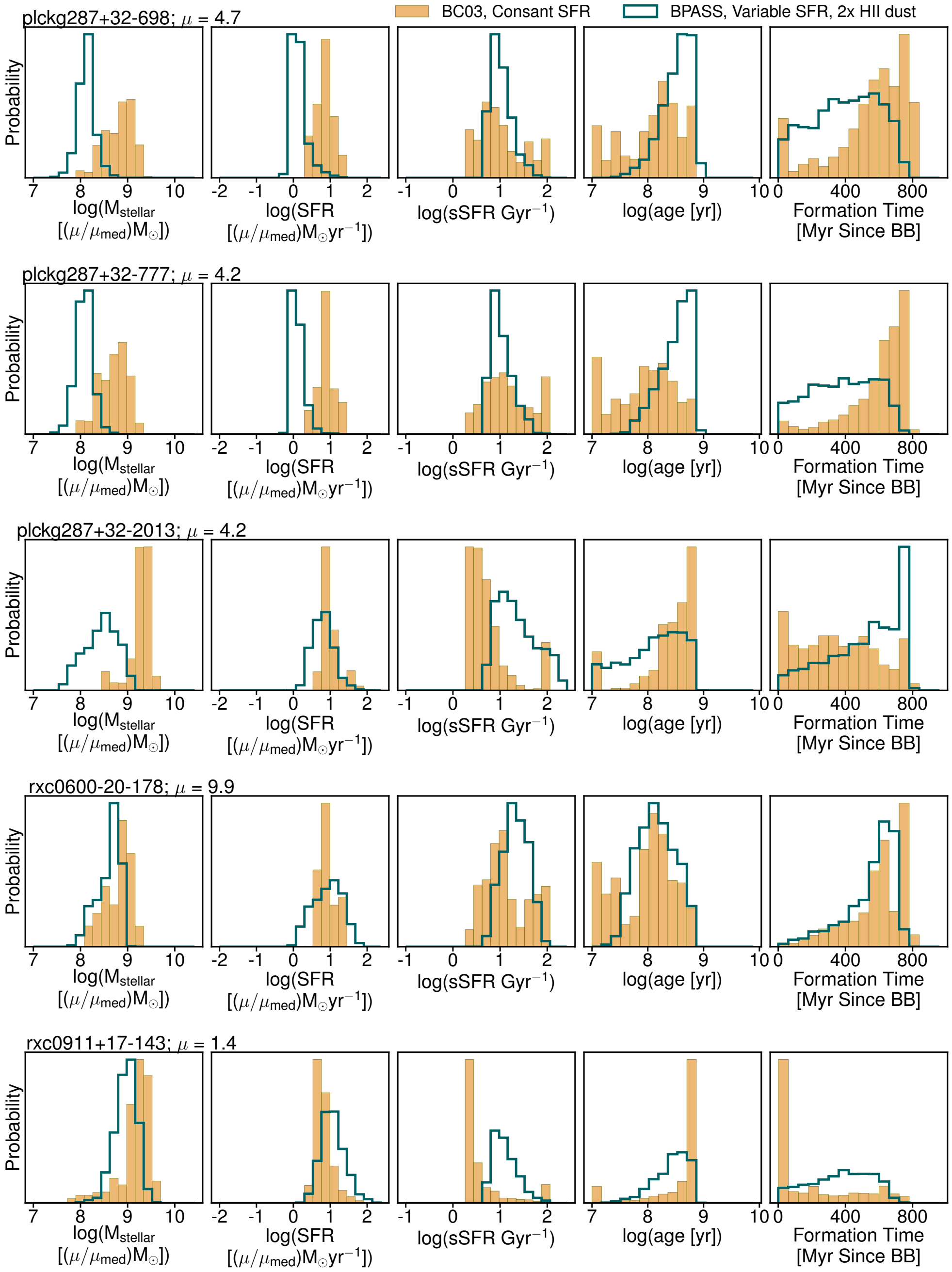

Figure 4.4: Results of SED fitting continued from Figure 4.3 for the last 5 of 11 objects in the sample which had both a redshift of at least $z \geq 6.5$ and at least one detection in *Spitzer*/IRAC.

formation and reionization, we also report mass-weighted age, as this is a more robustly constrained parameter (Leja et al., 2019). Mass-weighted age is defined as:

$$\mathrm{age}_{MW} = t_{obs} - t_{MW} \tag{4.3}$$

$$t_{MW} = \frac{\int_{t_{form}}^{t_{obs}} t\ SFR(t)\ dt}{\int_{t_{form}}^{t_{obs}} SFR(t)\ dt}. \tag{4.4}$$

4.3.3.2 Metallicity and Dust

In our Method A SED fitting template library, we assume a metallicity of $0.2Z_{\odot}$. While there is evidence that this assumption is appropriate for at least some of our sample (Jones et al., 2020), we still test the effects of these biases by fitting our data to templates using several dust laws and metallicities, and find that changing the dust law choice from SMC to Milky Way biases stellar masses high by ~ 0.5 dex, and that even large changes in metallicity introduce subdominant biases, < 0.1 dex. In Method B, we allow a range of metallicities and attenuations in order to remain agnostic to this issue.

4.3.3.3 Nebular Emission

It has been shown that emission lines can contribute significantly to broadband flux, and several recent studies have shown that these emission lines can be more extreme than previously thought. For example, the combination of H-β and [OIII] can sometimes be up to ~ 3000Å in their rest-frame equivalent width (Labbé et al., 2013; Finkelstein et al., 2013; Smit et al., 2015), and are regularly observed to be $\sim$700Å (Endsley et al., 2020a). We have included nebular emission in our templates, as described in Section 4.3. With our observational setup, the most relevant contaminating lines are [OIII] and H-β, as these are the likely strongest emission lines in our observed-frame window. These lines are observed in our templates from Method A to span a dynamic range from 0 to ~ 2000Å in rest-frame equivalent width. This range allows for extreme line emitting galaxies to be identified for all but the rarest objects. However, there is a degeneracy in IRAC colors between extreme line-emitting galaxies at $z \sim 8$ and those with a steep Balmer/$\mathrm{D_n}$(4000Å) break (hereafter, Balmer break), signifying an evolved stellar population. Since we allow for both in our templates in Method A, and allow ionization parameter log(U) to vary to extreme values in

Method B, where [OIII] can have EWs upwards of 10000Å, our approach makes us agnostic to this issue. The degeneracy between a Balmer break and strong [OIII]+H-β emitters, however, cannot be truly disentangled without secure measurements of [OIII]+Hβ EW with *JWST*, and in some cases ($z > 9.1$), with spectroscopic redshifts, to determine in which IRAC band the emission lines fall.

4.3.3.4 Binary Stars

Lastly, it has been shown that the inclusion of binary stars in the creation of stellar population synthesis templates can influence the results (Eldridge et al., 2008). For this reason, we use BPASS templates in Method B. We find that the change from BC03 to BPASS templates alone does not significantly change our results in terms of the average redshifts and stellar properties of our candidates, though considerable changes can be induced for individual candidates.

4.3.3.5 Differences in SED Fitting Methodology

Due to the fact that we are varying assumptions in modeling as discussed above as well as using two different methods of fitting models to our data, the differences must be carefully interpreted. In Method A, we are creating a grid of best-fit solutions after each iteration of sampling from photometry. The results of this method rely heavily on the template set that we have generated – specifically, how age is sampled, and what ionization or dust conditions are allowed. Taking only the best-fit on each iteration may not take into account solutions that are nearly as good as the best fit solution (e.g., the “second-best fit”). In turn, this may affect our results by not including all “good” fits to the data. We believe this may be part of the reason that our results from Method A are, in general, peakier and sometimes bimodal, rather than a broader, unimodal distribution like those seen in Method B.

Method B uses Nested Sampling, which, similar to Markov Chain Monte Carlo techniques, is a robust way to calculate posteriors for distributions that may be multimodal or may have pronounced degeneracies. Rather than sampling from photometry, BAGPIPES explores an n-dimensional parameter space, each time judging the goodness of fit and, taking into account the input priors, outputs a marginalized posterior for all n parameters that are being fit. This means that generally, a smoother distribution of each parameter is found, and nearly all “good” solutions for the data are reported in the posteriors.

While these differences in methodology affect our results for individual galaxies, we note that the overall sample distributions (stellar mass, SFR, sSFR) do not change dramatically, with the exception of formation age (see Section 4.5). This is likely because formation age is a difficult parameter to constrain, and due to our assumption of a constant SFH in Method A.

4.4 Lens Modeling

4.4.1 Magnification Maps

Many of our derived properties are unaffected by lensing, including age, dust extinction, metallicity, sSFR, and emission line strengths. Other properties (stellar mass, SFR, M_{UV}) must be corrected for lensing magnifications. To do so, we use magnification maps provided by RELICS lens modeling teams. The maps we utilize in this work are from one of three types of lens models: `Lenstool` (Jullo & Kneib, 2009), Glafic (Oguri, 2010), and light-traces-mass (LTM, e.g., Zitrin et al., 2013). Several papers have been published describing the lens models (Cerny et al., 2018; Acebron et al., 2018; Cibirka et al., 2018; Paterno-Mahler et al., 2018; Acebron et al., 2019a; Mahler et al., 2019; Acebron et al., 2019b; Okabe et al., 2020). All models used in this work are available on MAST for public use. Not every model has been detailed in a publication, but the general methods are very similar to those described in the papers listed here.

For each method, a routine bootstrapping of lensing constraints is performed to create 50–100 models, each yielding a magnification estimate given a lensed galaxy's position and redshift. We adopt the Method B median redshifts, extract the 50–100 magnification estimates, then take the median as the estimate from each method. For clusters modeled by 2 or 3 methods, we take the average of those median estimates as our final magnification estimate for that galaxy.

The lens models provide magnification estimates for 150 of our 207 high-z candidates. The median of these 150 estimates is $\mu = 2.9$, and 127 (85%) of those have $\mu < 10$. Only 6 have $\mu > 30$, the highest being $\mu = 96$ for plckg287+32-2457, an average of 107 and 85 from GLAFIC and LTM, respectively. We have reason to doubt individual magnification estimates $\mu > 30$ (Meneghetti et al., 2017), but the average of medians lends somewhat more confidence to the few higher estimates reported here.

For some RELICS clusters, no strong lensing models are available, as no multiple images were identified in the *HST* imaging. In those cases, we adopt a nominal magnification of $\mu = 3$ for all high-z candidates. This is roughly the median of the 150 estimates and within a factor of 3 for 125 (83%) of those.

Given magnification estimates for all 207 high-z candidates, we divide our derived mass, SFR, and luminosity by these magnifications before reporting the results in Table 4.4. We also report the 68% confidence limits of each magnification estimate, but we do not add these to the reported uncertainties of the derived properties. This is so that the reader can easily use their own magnification and uncertainty measurements.

The models have varying numbers of multiple-image lensing constraints, making them not all equally reliable. For some clusters, no multiple images were identified for strong lensing analysis. In those cases, we relied on "blind" LTM models (in contrast with the regular LTM models mentioned above where constraints are available) with a mass-to-light normalization typical of other clusters(Zitrin et al., 2012). For these blind LTM models, the (larger) uncertainties follow from the uncertainties in typical mass-to-light normalizations.

4.4.2 Source Plane Modeling

We perform source-plane modeling for the 11 galaxies highlighted in this manuscript, and show the results in Figure 4.1. Closely following the methods of Yang et al. (2020), we use the publicly available code `Lenstruction` (based on `Lenstronomy`[8]) to forward model the high-z galaxies using their appearance in the image plane to predict their morphology and size in the source plane. `Lenstruction` takes into account distortion from lensing and the instrument PSF, and works to estimate pixel noise and remove the background flux level. We assume Glafic global magnification models when modeling each of the galaxies. We modeled each source as a singly-imaged galaxy, and we will explore this work further in Neufeld et al., in prep.

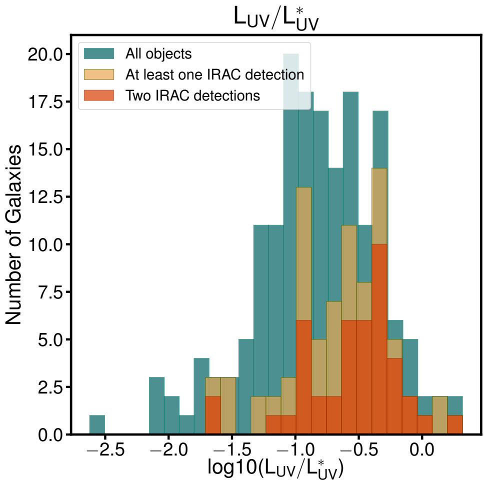

Figure 4.5: The distribution of L_{UV}/L^*_{UV}, intrinsic luminosity normalized by the characteristic luminosity for that object's redshift, for (in teal/blue) all 207 galaxies in the sample, (in tan) galaxies that were detected at least once by *Spitzer*/IRAC, and (in orange) galaxies that were detected twice in *Spitzer*/IRAC. A large majority of all three subsets of the sample are $L_{UV}/L^*_{UV} < 1$, with a few objects at $L_{UV}/L^*_{UV} \sim 2$.

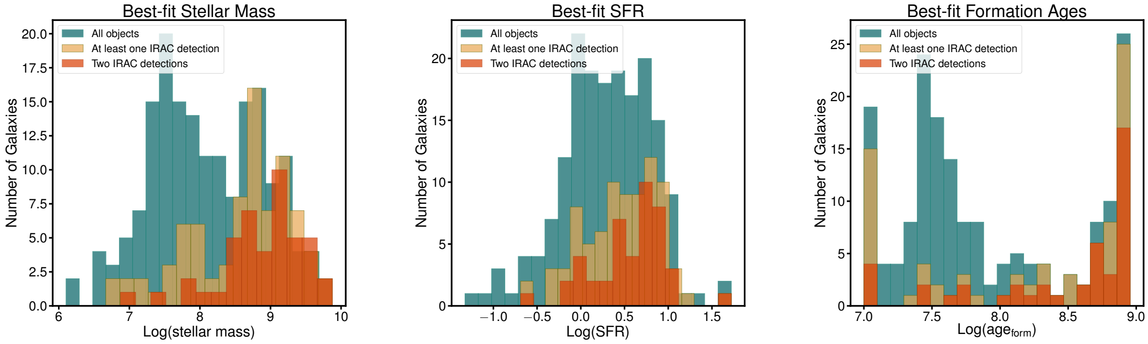

Figure 4.6: Histograms of best-fit physical parameters derived by Method A. In all panels, teal/blue is all 207 galaxies in the sample, tan is galaxies with at least one *Spitzer*/IRAC detection, and orange is galaxies with two *Spitzer*/IRAC detections. **Left:** Best-fit log stellar mass distribution ($M_\odot$). Detected galaxies fall on the higher stellar mass end, showing a bias of *Spitzer* being able to detect higher stellar mass objects due to brighter rest-frame optical fluxes. **Center:** Best-fit log(SFR) distribution ($M_\odot$/yr). Similar to stellar mass, higher SFR galaxies are more often detected than lower SFR (due to a correlation between M* and SFR). **Right:** Best-fit log(age) distribution, where age here is age of formation in years: $t_{obs} - t_{form}$. Galaxies detected in *Spitzer* tend to be older. Since we are assuming a constant SFH, this makes sense because older galaxies will have had more time to form more mass, an effect likely due to both the intrinsic properties of the galaxies we detect and our assumption of a constant SFH, which requires more massive galaxies to be older.

Table 4.3. Spitzer Photometry of Selected Galaxies

Object ID	R.A. (deg.)	Dec. (deg.)	$F160W$[1] (mag)	$[3.6]$[2] (mag)	$R_{3.6}$[3]	$[4.5]$[2] (mag)	$R_{4.5}$[3]
abell1758-1942	203.2001098	50.5185167	24.82 ± 0.05	24.03 ± 0.17	0.1	> 25.08	0.1
abell1763-1434	203.8333744	40.99017930	26.17 ± 0.08	25.74 ± 0.49	0.3	24.75 ± 0.26	0.3
act0102-49-2391	15.72313210	-49.2393723	26.26 ± 0.14	25.29 ± 0.21	0.2	26.03 ± 0.39	0.3
act0102-49-2551	15.72568030	-49.232616	26.25 ± 0.12	25.03 ± 0.16	0.1	25.49 ± 0.205	0.1
cl0152-13-191	28.17164110	-13.9734429	27.31 ± 0.16	24.69 ± 0.15	0.4	25.04 ± 0.25	0.5
macs0553-33-219	88.3540349	-33.6979484	27.19 ± 0.18	25.60 ± 0.31	0.5	26.41 ± 0.65	0.5
plckg287+32-2013	177.6877971	-28.0760864	24.88 ± 0.09	23.79 ± 0.11	0.7	25.24 ± 0.43	0.7
plckg287+32-698	177.7049678	-28.0707102	25.00 ± 0.07	24.58 ± 0.20	0.5	25.01 ± 0.29	0.5
plckg287+32-777	177.7199024	-28.0715239	25.16 ± 0.07	24.80 ± 0.22	0.5	25.48 ± 0.40	0.5
rxc0600-20-178	90.0271054	-20.1202486	24.42 ± 0.04	23.89 ± 0.12	0.2	> 25.32	0.1
rxc0911+17-143	137.7939712	17.7897516	26.45 ± 0.13	25.86 ± 0.29	0.1	25.72 ± 0.36	0.1

[1] Observed (lensed) isophotal magnitude (`MAG_ISO`)

[2] *Spitzer/IRAC* Channels 1 and 2 magnitudes measured using T-PHOT with the same aperture as HST magnitudes and 1-σ error. If detection is $<$ 1-σ, the 1-σ lower limit is reported.

[3] Covariance index for *Spitzer*/IRAC channels (Section 4.2.2.2)

4.5 Results

4.5.1 Sample Selection

The goal of this work is to explore the stellar properties of $z \geq 5.5$ galaxies. We start from the sample defined in Salmon et al. (2020), which consists of 321 *HST*-selected galaxy candidates with a best-fit $z \geq 5.5$. Objects in this sample were required to have a median or peak in photometric redshift $P(z)$ at $z \geq 5.5$ in at least one of the redshift-fitting codes used, a $> 3\sigma$ detection in F160W, stellarity of $< 98\%$ (i.e., excluding point sources), and (Y-J) color > 0.45 (to filter out brown dwarfs). The objects also passed an extensive visual inspection process where they were vetted for diffraction spikes, transients, detector edge

---

[8] https://github.com/sibirrer/lenstronomy

Table 4.4. Photometric Redshift and Stellar Population Modeling Results from Method A of Galaxies detected in [3.6] and/or [4.5] and having a best-fit redshift of $z \geq 6.5$. Full catalog available at victoriastrait.github.io/relics

Object ID	$z_{\rm med}$[1]	$\mu_{\rm med}$[2]	M$_{\rm stellar}$[3] ($10^9 M_\odot$)	SFR[3] ($M_\odot {\rm yr}^{-1}$)	$t_{\rm form}$[4] (Myr)	sSFR[5] (Gyr^{-1})	E(B − V)[6] (mag)	M$_{1600}$[7] (mag)
abell1758-1942	$6.1^{+0.1}_{-0.1}$	$1.9^{+0.4}_{-0.2}$	$2.0^{+1.5}_{-1.8}$	$6.8^{+8.6}_{-0.7}$	404^{+500}_{-394}	$3.6^{+101.4}_{-1.9}$	$0.00^{+0.00}_{-0.00}$	$-22.1^{+0.8}_{-0.7}$
abell1763-1434	$8.4^{+0.4}_{-0.4}$	$3.3^{+2.4}_{-0.7}$	$1.2^{+0.9}_{-1.0}$	$5.4^{+6.9}_{-2.3}$	508^{+62}_{-499}	$2.9^{+102.1}_{-0.3}$	$0.10^{+0.05}_{-0.05}$	$-21.1^{+0.8}_{-0.7}$
act0102-49-2391	$6.9^{+0.2}_{-0.2}$	$4.1^{+0.7}_{-0.7}$	$0.4^{+0.2}_{-0.3}$	$81.5^{+3.2}_{-0.6}$	509^{+210}_{-497}	$2.9^{+85.6}_{-0.8}$	$0.05^{+0.05}_{-0.05}$	$-20.6^{+0.7}_{-0.8}$
act0102-49-2551	$6.8^{+0.1}_{-0.1}$	$2.2^{+0.3}_{-0.3}$	$3.7^{+1.1}_{-1.0}$	$9.5^{+1.2}_{-3.5}$	719^{+0}_{-148}	$2.1^{0.5}_{0.0}$	$0.05^{+0.00}_{-0.05}$	$-20.7^{+0.8}_{-0.7}$
cl0152-13-191	$6.7^{+0.2}_{-0.4}$	$1.8^{+0.1}_{-0.1}$	$3.6^{+1.8}_{-1.3}$	$7.3^{+3.8}_{-2.7}$	719^{+89}_{-0}	$2.1^{+0.0}_{-0.2}$	$0.20^{+0.05}_{-0.05}$	$-19.6^{+0.8}_{-0.7}$
macs0553-33-219	$7.6^{+0.8}_{-6.0}$	$2.4^{+0.3}_{-0.1}$	$0.5^{+0.9}_{-0.4}$	$2.1^{+3.0}_{-1.7}$	571^{+334}_{-480}	$2.6^{+11.3}_{-0.9}$	$0.10^{+0.60}_{-0.10}$	$-20.0^{+0.8}_{-0.7}$
plckg287+32-698	$6.8^{+0.2}_{-0.2}$	$4.3^{+0.7}_{-0.8}$	$0.6^{+0.5}_{-0.4}$	$5.3^{+6.0}_{-2.1}$	161^{+243}_{-135}	$8.2^{+34.7}_{-4.7}$	$0.05^{+0.05}_{-0.05}$	$-22.0^{+0.8}_{-0.7}$
plckg287+32-777	$7.0^{+0.2}_{-0.1}$	$4.0^{+0.7}_{-0.4}$	$0.5^{+0.4}_{-0.3}$	$5.5^{+5.8}_{-2.5}$	102^{+185}_{-84}	$12.5^{+50.8}_{-7.6}$	$0.05^{+0.05}_{-0.05}$	$-21.8^{+0.8}_{-0.7}$
plckg287+32-2013	$7.3^{+0.3}_{-0.3}$	$4.0^{+0.5}_{-0.5}$	$1.5^{+0.6}_{-0.5}$	$6.0^{+4.7}_{-1.0}$	360^{+280}_{-232}	$4.0^{+6.2}_{-1.6}$	$0.05^{+0.05}_{-0.00}$	$-22.2^{+0.8}_{-0.7}$
rxc0600-20-178	$7.1^{+0.2}_{-0.3}$	14^{+26}_{-4}	$1.4^{+0.8}_{-0.8}$	$16.1^{+15.8}_{-7.1}$	114^{+207}_{-95}	$11.3^{+46.5}_{-6.9}$	$0.10^{+0.05}_{-0.05}$	$-22.6^{+0.7}_{-0.8}$
rxc0911+17-143	$8.1^{+0.4}_{-0.6}$	$1.5^{+0.2}_{-0.1}$	$1.2^{+0.8}_{-0.6}$	$4.6^{+3.5}_{-1.7}$	571^{+70}_{-480}	$2.6^{+11.3}_{-0.3}$	$0.05^{+0.05}_{-0.05}$	$-20.7^{+0.7}_{-0.8}$

[1] Median redshift and 68% CL in PDF described in Section 3.2

[2] Magnification factor: we use the mean of median magnifications for each available lens model. μ is assumed in SFR, M$_{\rm stellar}$, and M$_{(1600)}$ calculations.

[3] Intrinsic stellar mass and SFR, assuming $\mu = \mu_{\rm med}$. Uncertainties include statistical 68% CLs from photometry and redshift. To use a different magnification value, multiply the quantity by $1/f_\mu$, where $f_\mu \equiv \mu/\mu_{\rm med}$.

[4] Time since the onset of star formation assuming a constant SFR

[5] Specific SFR, sSFR $\equiv M_{stellar}/{\rm SFR}$

[6] Dust color excess of stellar emission. SMC dust law assumed.

[7] Rest-frame 1600 Å magnitude assuming $\mu_{\rm med}$, derived from the observed F160W mag including a small template-based k-correction. Uncertainties include statistical 68% CLs from photometry and redshift. To use a different magnification value, use M$_{(1600)} - 2.5\log({\rm f}_\mu)$.

noise, and other image artifacts (see Salmon et al., 2020 for more details).

We were able to successfully extract fluxes or flux upper limits in magnitude for 207 galaxies from *Spitzer*/IRAC observations using the process described in Section 4.2.2.2. The remaining 114 galaxies were too crowded by bright neighboring sources, usually cluster members. Most objects for which we could not extract a *Spitzer*/IRAC flux were within ∼1" of a cluster member or other bright (¡17 AB mag) galaxy. For a flux to be considered reliable, we require that the residual (model - image) pixels be centered close to zero with the exception of artifacts from bright objects. The galaxies which were rejected generally showed a large over-subtraction or an obvious artifact in the residual.

Of the objects rejected from the sample, their apparent magnitudes, luminosities, and magnifications span a similar range as that of the entire sample. From this, we conclude that we are not biasing our sample by removing these galaxies.

Of the objects with reliable photometry, 96 have at least one IRAC detection of S/N > 1. The overall redshift distribution did not change significantly from the *HST*-only distribution (Figure 6 in Salmon et al., 2020), though 23 galaxies now have significant peaks in redshift at $z < 4$. In our analyses, we focus mostly on our final high redshift candidate sample, but discuss the demoted objects further below.

4.5.2 Construction of Catalog

In the catalog[9], we present the photometry of the 207 objects for which we successfully extracted *Spitzer* photometry, including *HST* fluxes and covariance indices from T-PHOT which acts as a flag for possible blending with neighboring sources (galaxies with $R_{[3.6],[4.5]} > 1$ should be treated with caution, see Section 4.2 for the exact definitions). Along with photometry and covariance indices, we include median magnifications from and 68% confidence limits from each lens model available on MAST, and the mean of those for any clusters with more than one model. In addition to photometry and magnification, we include the median values and upper and lower 68% confidence limits on redshift, SFR, stellar mass, sSFR, and age from our Method A and B described in Section 4.3. Units are described in the header of the catalog. We note that objects MACS0553-33-1014 and MACS0553-33-1016 were considered separate objects in Salmon et al. (2020), but here we consider them the same galaxy, as

---

[9] victoriastrait.github.io/relics

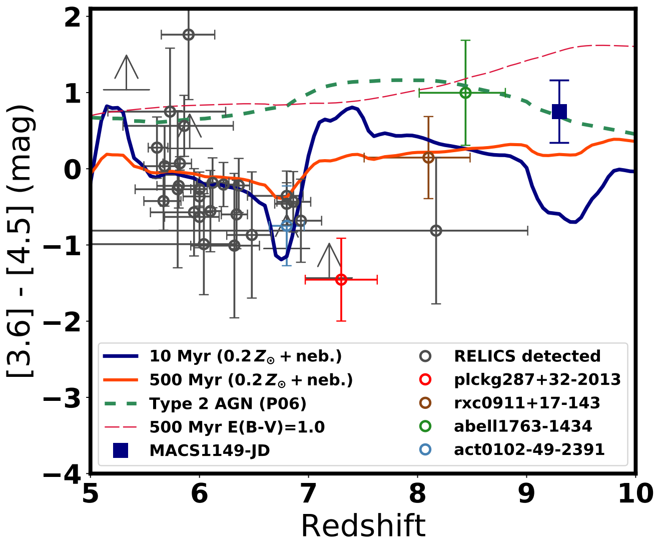

Figure 4.7: IRAC [3.6]−[4.5] color vs. redshift for the galaxies in our sample with at least one IRAC S/N > 3 detection (open circles with error bars). In red, brown, green, and blue open circles are PLCKG287+32-2013, RXC0911+14-143, Abell1763-1434, and ACT0102-49-2391, respectively, the objects we highlight later in §4.5. The dark blue filled square is MACS1149-JD from Hashimoto et al. (2018), an object with evidence for an evolved stellar population at $z = 9.11$. Lines are tracks from various models from BC03, showing the predicted colors for that model. Redshifts are calculated independently from these models (see Section 4.3). PLCKG287+32-2013 and ACT0102-49-2391 have colors consistent with the $z = 6.6 - 6.9$ color bump due to [OIII]+H-β emission in [3.6]. Abell1763-1434 aligns well with older, dustier and AGN models.

their *Spitzer*/IRAC fluxes are blended and they are ∼ 0.6” apart. In the catalog, they are listed as object MACS0553-33-1014. All other objects have the same ID and coordinates as in Salmon et al. (2020).

4.5.3 Properties of the Sample

In this Section, we will first discuss the physical properties of the sample as a whole, presenting distributions of stellar mass, SFR, and age, and then later individual galaxies. Unless otherwise stated, we have used Method A for estimating the stellar properties presented here.

The quantity $\mathrm{L_{UV}/L^*_{UV}}$, the intrinsic luminosity of a source normalized by the characteristic luminosity for its redshift, informs the intrinsic brightness of our sample relative to that of the broader galaxy population. We calculate this by using $\mathrm{M_{UV} = H160 + 2.5log_{10}(1 + z) - 5 \times log_{10}(d_{pc}) + 5}$, where H160 is the observed F160W flux in AB magnitudes (chosen because all objects are detected significantly in this band, and K-corrections using this band are negligible), and d_{pc} is distance of the object in parsecs. Characteristic magnitude is $\mathrm{M}^*_{\mathrm{UV}} = (-20.95 \pm 0.10) + (0.01 \pm 0.06) \times (\mathrm{z}_{\mathrm{peak}} - 6)$ (the relation from Bouwens et al., 2015b). We then correct for magnification in M_{UV} and convert both M_{UV} and $\mathrm{M}^*_{\mathrm{UV}}$ to luminosity. In Figure 4.5 we present the distribution of L_{UV}/L^*_{UV} for our sample, splitting the sample into those twice detected by IRAC, at least once detected, and the entire sample. $\sim 95\%$ of our sample falls at or below $1 L_{UV}/L^*_{UV}$, with a few objects are $\sim 2 L_{UV}/L^*_{UV}$, suggesting that we are probing a combination of galaxies characteristic for their redshifts as well as bright, perhaps unusual ones. The galaxies which are detected in both IRAC channels are, unsurprisingly, a larger percentage of intrinsically bright galaxies (the median value of L_{UV}/L^*_{UV} for galaxies detected in both IRAC channels is 1.4, or -23.2 mag), however we do detect several $< 0.5 L_{UV}/L^*_{UV}$ galaxies.

In Figure 4.6, we show distributions of best-fit age of formation (t_{form}), stellar mass and SFR, using assumptions from Method A in Section 4.3. In each subplot, we again distinguish between the galaxies that are detected twice in IRAC, at least once in IRAC, and the entire sample. It is clear that galaxies in our sample with IRAC detections tend to take on a higher stellar mass, SFR, and formation age, possibly pointing to an observational bias. These are the same galaxies which tend towards intrisically brighter ($L_{UV}/L^*_{UV} > 1$) in Figure 4.5. We note that for a constant SFH, which we assume in our Method A SED fitting method, it is expected for at least some of these properties to be intrinsically correlated, as it will take a longer amount of time for a galaxy to build up a certain amount of mass at a given constant SFR. Notably, the overall distributions for the sample (and those of individual objects) between Methods A and B do not change appreciably, with the exception of formation age.

As mentioned above, a possible effect at play in the sample distributions is an observational one: the galaxies with the brightest IRAC fluxes are the ones with detections, which will either be old galaxies with a strong Balmer break or young galaxies with strong emission lines. This is reflected in the age of formation distributions of each object in Figures 4.3 and 4.4. Within the sample of high-z candidates that received ∼30 hours of *Spitzer* imaging, there are several examples of upper limits in flux constraining young galaxies (i.e., reaching depths of ~ 27 mag without seeing a detection and thus revealing a very blue spectral shape and pointing to a young stellar population absent of dust). However, a large majority of the time (because the majority of our sample contains relatively shallow, ~ 5 hour IRAC data), the comparison between detected and undetected galaxies is not necessarily a fair one. There could be galaxies with bright IRAC fluxes in clusters with shallow data that we are missing. Hence, the distributions in Figure 4.6 show a combination of the variety of stellar populations we are probing with our sample and our observational limits.

In Figure 4.7, we show the *Spitzer*/IRAC [3.6]-[4.5] color as a function of redshift for a variety of models, including a young (10Myr) and dust-free template, and an evolved (500Myr) dust-free template, as well as an evolved template with E(B-V)=1.00. For comparison, we also include a Type 2 AGN model. These tracks were created from our set of BC03 + nebular continuum and emission templates described in Section 4.3 (Method A). Plotted over these models, we show the objects in our data which have at least one IRAC detection of S/N<3, highlighting select objects discussed below. Generally, we find that the IRAC colors in our sample trace the 10 Myr and 500 Myr models without dust, with some notable exceptions which we discuss in Sections 4.5.4.1 and 4.5.4.3.

4.5.4 Detected Objects $z \geq 6.5$

RELICS was designed to find and characterize galaxy populations at high-redshift, apparently bright galaxies in a variety of fields that would be particularly good candidates for spectroscopic follow-up. For this reason, we highlight the objects we find to have the most informative data and be best candidates for follow-up. In Figure 4.2, we show the best-fit Method A SEDs for the 11 galaxies in our sample that have at least one $S/N > 3$ IRAC detection and a best-fit redshift of $z \geq 6.5$. In blue, we show the best-fit high redshift ($z > 4$) template and in red, the best-fit low redshift template ($z < 4$) using the Method A assumptions described in Section 4.3. The posteriors of stellar mass, formation age, star formation rate, specific star formation rate, and formation time for individual objects from Method A are shown in Figures 4.3 and 4.4. In yellow/tan filled histograms, we show the results from Method A (BC03 templates, constant SFH), and in open dark green histograms, we show the results of Method B (BPASS, rising/declining SFH defined by Equation 4.1, extra birth cloud dust).

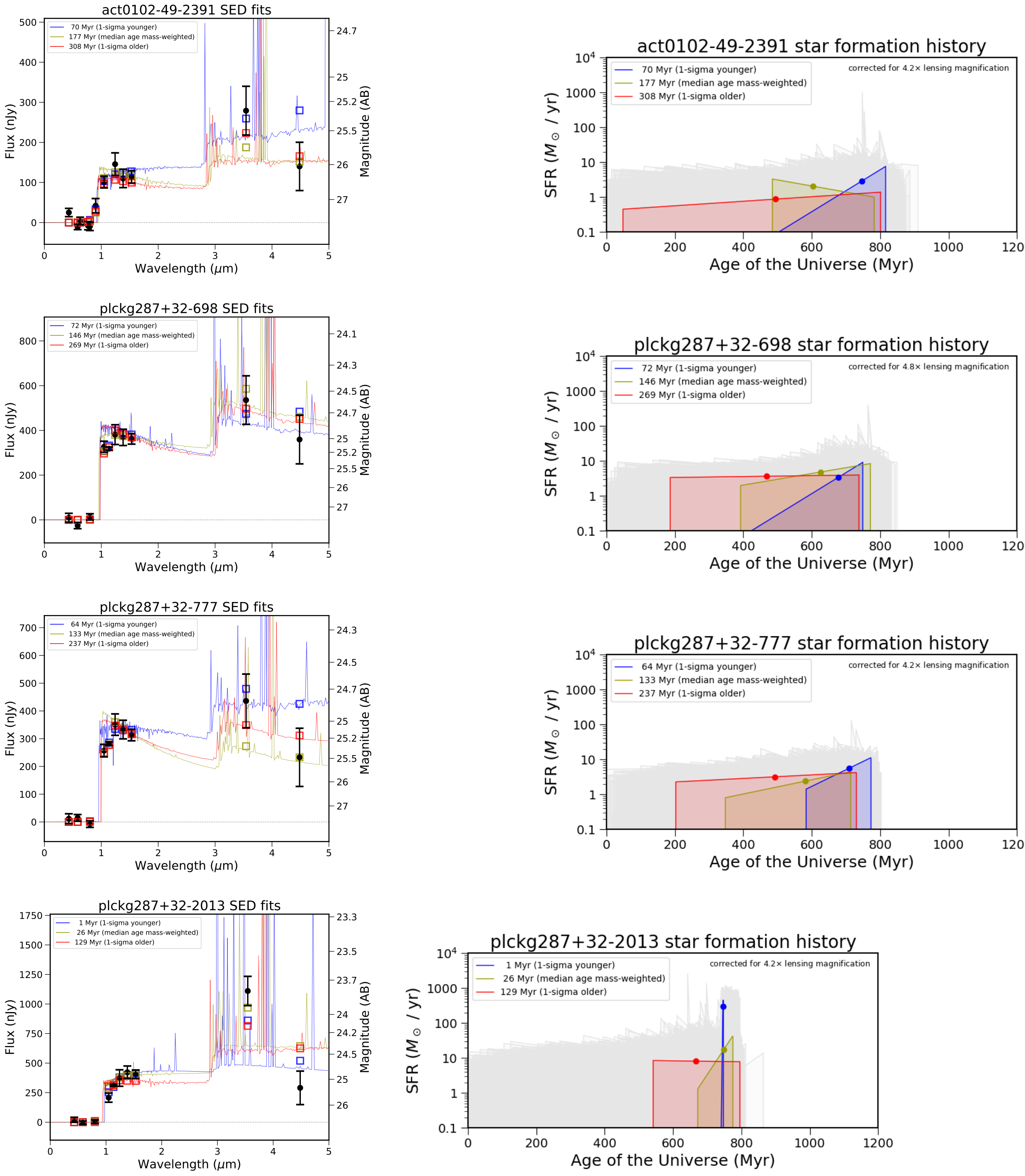

Figure 4.8: Left: Observed photometry (black), model photometry (open squares), and SEDs of the four objects discussed in Section 4.5.4.1 from Method B using BAGPIPES. Yellow template is an SED with the median mass-weighted age, blue is 1-σ younger, and red is 1-σ older. See Section 4.3.3 for distinction between formation age and mass-weighted age. **Right:** SFHs of the templates on the left, in corresponding colors. Circles denote times of mass-weighted ages. In gray are all SFH realizations.

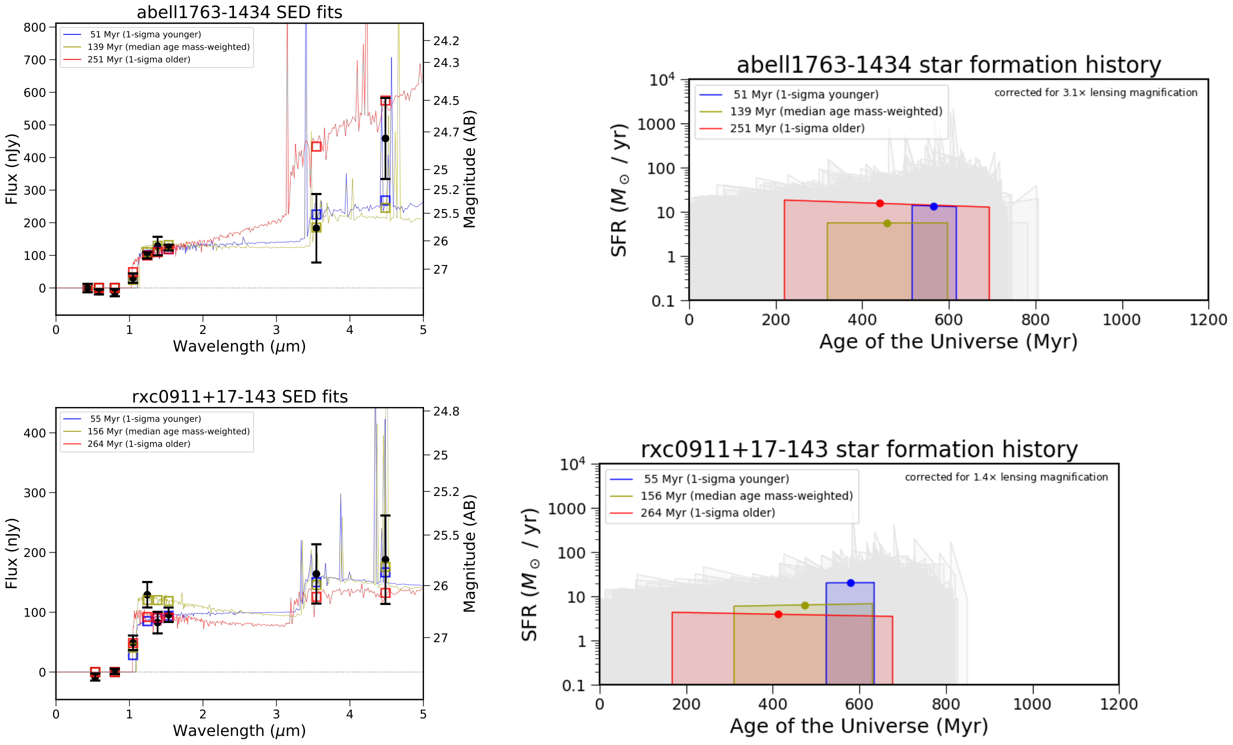

Figure 4.9: SEDs and SFHs as in Figure 4.8 for the two galaxies discussed in Section 4.5.4.3.

Of note in this sample is that several of the objects have likely redshifts around $z \sim 6.6 - 7$, because of an elevated [3.6] magnitude, which indicates a strong [OIII]+H-β emission line falling in ch1 at those redshifts. Additionally, we also see several objects which prefer a nearly maximally old formation age; that is, the galaxies would have started forming < 100 Myr after the Big Bang.

4.5.4.1 Objects With Potentially Strong Emission Lines

Of the objects highlighted in this work, the ones with blue IRAC [3.6]-[4.5] colors at $z = 6.8 - 7.0$ include ACT0102-49-2391, Abell1758-1942, PLCKG287+32-698, PLCKG287+32-777, and PLCKG287+32-2013. Of these, we focus on three objects in PLCKG287+32: 2013, 698, and 777, as well as ACT0102-40-2391.

We show our analysis of these objects with BAGPIPES in Figure 4.8: SEDs fit to the median and $\pm 1\sigma$ in mass-weighted age template (note that we are now using mass-weighted age, defined in Equation 4.3 instead of formation age as it is more easily constrained), and the median $\pm 1\sigma$ in mass-weighted age SFHs in corresponding colors, as well as all allowed SFHs in gray. In PLCKG287+32-2013, one can see that the youngest (blue line) template shows a very recent, steeply rising burst of star formation. With a lower S/N detection, the range of solutions and SFHs for ACT0102-49-2391 are much dramatic.

Additionally, we highlight these objects in Figure 4.7. Of the four galaxies, PLCKG287+32-2013 has the highest S/N [3.6] detection ($\sim 9\sigma$). EAzY yields $z = 7.3 \pm 0.3$, while BAGPIPES finds $z = 6.8^{+0.2}_{-0.1}$. As can be seen in Figure 4.7, both objects show more extreme (blue) IRAC colors than most of the sample. In combination with the fact that they are consistent with the expected color decrease at $z \sim 6.6 - 6.9$ for young, star-forming galaxies, we believe these are potentially strong [OIII]+H-β emitters. The PLCKG287+32-2013 IRAC color corresponds to rest-frame equivalent widths of ~ 1000Å. Compared to galaxies observed at $z = 0.2 - 0.9$ where [OIII]+H-β equivalent widths are commonly observed to be < 100Å and extreme emission line galaxies (EELGs) are defined to be anything above that (Mainali et al., 2020; Amorín et al., 2014), this is a relatively high EW, and in line with the extreme emitters discovered by Endsley et al. (2020a) (1000-4000Å at $z \sim 7$) and those discovered by Mainali et al. (2020) (500-2000Å at $z \sim 2 - 3$). These high EWs suggest a high value of the ionization parameter log(U), which corresponds to a hard spectrum and an ISM or even circumgalactic medium (CGM) replete with energetic ionizing photons. One possible consequence of this suggestion is the presence of an ionized bubble carved out by star formation (see, e.g., Tilvi et al., 2020) as a result of an ongoing burst of star formation (consistent with the youngest SFH for PLCKG287+32-2013 in Figure 4.8). Endsley et al. (2020a) argue that while galaxies with extreme [OIII]+H-β may be experiencing a short-lived burst of star formation that, based on similarities to Lyman-continuum leakers (galaxies that “leak” Lyman-continuum photons) at $z \sim 3$, these objects tend to have very high escape fractions at least for the duration of the burst. Additionally, since these galaxies seem to make up $\sim 20\%$ of the $z \sim 7$ population (though with large uncertainties), together they might be among the most effective objects at ionizing the IGM.

Two of these objects (PLCKG287+32-698 and 777) are multiple images in a quadruply imaged system, first discovered by Zitrin et al. (2017). In addition to finding the same redshift for both images analyzed here, we find convincingly similar physical properties with both Methods, as can be seen in Figures 4.3 and 4.4 ($M_* \sim 10^{8-9} M_\odot$, sSFR ~ 10Gyr^{-1}). We note the third lensed image in this system, PLCKG287+32-2235, is included in our catalog but is not significantly detected in *Spitzer*. The fourth lensed image PLCKG287+32-2977 was discovered in WFC3/IR F110W imaging but lands outside RELICS imaging in other WFC3/IR filters and was thus excluded from the Salmon et al. (2018) selection and this work.

The last object we focus on in this section, PLCKG287+32-2013, yields some similarities to two galaxies confirmed by ALMA with [CII] by (Smit et al., 2018). They are of similar observed brightness (apparent magnitude ~ 24.9), similar SFRs (within the uncertainties), and have similar IRAC colors. Smit et al. (2018) argue that an elevated [OIII]+H-β EW suggests a higher [CII] EW, potentially meaning that there are chances with ALMA follow-up for these objects to be able to place them on the infrared excess-UV slope (IRX-β) relation. Additionally, such extreme EWs are indicative of potential Ly-α emission (Roberts-Borsani et al., 2016; Oesch et al., 2015; Zitrin et al., 2015; Stark, 2016), and CIII] (e.g., Hutchison et al., 2019) presenting opportunities for ground-based infrared spectroscopy.

4.5.4.2 Gemini Observations of PLCKG287+32-777

We take this opportunity to note that PLCKG287+32-777 was spectroscopically observed with Gemini South (GS-2018A-Q-901; PI: Zitrin), and we publish here the first results from these observations. It was first observed for 2 hrs with Flamingos-2 (R3000 Grism + J-band filter). A 4-pixel ($0.72''$) wide longslit was used, leading to an average resolving power of $R \sim 1300$, with a nod size of $\pm 1.5''$. These observations were designed to detect potential CIV emission, although the detection limit is quite high (e.g., a 3σ limit per spectral pixel of $\simeq 1 - 1.5 \times 10^{-16}\mathrm{erg/cm^2/\AA}$ for a spectral line width of 100-300 km/s).

The object was also observed with Gemini Multi-Object Spectrograph (GMOS) in longslit Nod & Shuffle mode, with a 1" wide slit and a $\pm 2.5''$ nod size. Observations took place using the R400 grism + z-band filter, and two different central wavelengths (760 nm, 795 nm), for $\simeq 4.3$ hrs. These observations were aimed to detect Ly-α, and have a nominal 3σ depth per spectral pixel of $4.5 \times 10^{-17}\mathrm{erg/cm^2/\AA}$ for a 500 km/s Ly-α line at $z = 6.8$. At higher redshifts, the sensitivity drops, reaching half the SNR for Ly-α at $z \simeq 7.3$.

Both the F-2 and GMOS longslits also covered a second image of the lensed galaxy (2977), however the nod size in the GMOS observations only allowed for a credible search around the first object. No prominent emission line was detected in either observation for either image, suggesting that Ly-α may not be easily escaping this galaxy and the presence of extremely strong CIV emission is likely ruled out. However, we note that the data merit a more careful inspection, and we leave a more quantitative examination of these data for future work.

4.5.4.3 Objects Preferring Maximally Old Formation Age

In addition to galaxies with potentially strong nebular emission, there are a subset of galaxies in our sample show a strong preference with Method A and some preference with Method B, for a maximally old solution, with the earliest possible formation time, including ACT0102-49-2551, RXC0911+17-143, MACS0553-33-219, and Abell1763-1434. Here we focus on Abell1763-1434 and RXC0911+17-143, both of which were initially introduced by Strait et al. (2020b). The former has since received deeper data (~30 hours, from ~5 hours in Strait et al., 2020b).

As has been noted previously in this work, formation age is a difficult parameter to constrain, since the beginning of SFHs tend not to leave an imprint on a photometric SED. The results tend to be reliant on the implicit prior of the assumed SFH, which in the case of our Method A is constant. In Method B, we report mass-weighted age instead, since this quantity can be more reliably fit for. We will discuss both here.

In the top panel of Figure 4.9, we show our analysis with BAGPIPES of Abell1763-1434, where we plot again median $\pm 1\sigma$ mass-weighted age templates. In all cases, these templates represent relatively evolved stellar populations, reflected by the SFHs on the right panel which "turn on" relatively early. The oldest solution prefers a gently declining SFH, while the others are relatively constant. There are some solutions that prefer a high [OIII]+H-β EW (i.e., a young, high sSFR template rather than an evolved one with a Balmer break), which falls in IRAC ch2 at the redshift of this galaxy ($z \sim 8.4$), but overwhelmingly, an evolved stellar population is preferred.

A similar story can be told for RXC0911+17-143, shown on the bottom panel of Figure 4.9: this time with both IRAC fluxes elevated, there is evidence of a Balmer break, although the detections are lower S/N compared to Abell1763. The SFHs reflect a similar preference for a declining or constant, but relatively stagnant SFH for this object. When these objects are compared to the rest of our sample in Figure 4.7, both are consistent with an evolved and/or dusty solution. The red IRAC colors make these objects stand out from the rest of our sample as being closer in color-redshift space to MACS1149-JD, a spectroscopically confirmed galaxy with evidence for an early formation time (Hashimoto et al., 2018).

As argued by Strait et al. (2020b) and Roberts-Borsani et al. (2020), IRAC excess in [4.5], while often attributed to high values of [OIII]+H-β (which fall in ch2 at $z > 7$), can be equally (and sometimes more favorably) explained by a strong Balmer break, suggesting an evolved stellar population and/or dust. Roberts-Borsani et al. (2020) (and previously Hashimoto et al., 2018) goes on to suggest ways of distinguishing these solutions, including the use of the ALMA to detect the [OIII] 88μm line, whose strength is related to the [OIII] 5007Å line.

4.5.5 Demoted Objects

Of the 207 galaxies for which we could extract reliable *Spitzer* fluxes, 23 have non-trivial peaks in redshift at $z < 2$, revealing a $\sim 10\%$ contamination rate for *HST*-selected Lyman-break galaxies. Notably, the bright $z \sim 6$ galaxies behind RXS0603+42 (both north and south HST pointings) had a high “failure” rate. Of the 13 high-redshift candidates behind this cluster, we were able to extract *Spitzer* fluxes for 8. Of those, only 2 remain likely at high redshift. The rest are likely $z \sim 1$ galaxies or brown dwarfs.

4.6 Future Data

Ultimately, spectroscopic followup will be necessary to place strong constraints on properties of these galaxies, such as dust content, metal enrichment, and ionization field. There are a number of existing and future telescopes that will be well-suited to this task:

Ground-based infrared spectroscopy with telescopes such as Keck will allow for a search of rest-frame UV emission lines such as Lyman-α and CIII]. There are a number of studies detailing how such observations can aid in constraining SFR, metallicities, AGN activity, and ionization with these emission lines (e.g., Finkelstein et al., 2013; Stark, 2016; Nakajima et al., 2018; Hutchison et al., 2019; Le Fèvre et al., 2019). As discussed above, the presence of strong [OIII]+H-β emission makes detection of Lyman-α and CIII] more likely.

A millimeter/sub-millimeter telescope such as ALMA could be used to determine the presence of [OIII]88μm or [CII]158μm, which would lead to insight on the dust and metal content (e.g., Roberts-Borsani et al., 2020; Bradač et al., 2017), constraints on the strength of [OIII]5007Å (Hashimoto et al., 2018; Roberts-Borsani et al., 2020), and even kinematics (e.g., Smit et al., 2018). Placing high-redshift galaxies on the IRX-β relation is valuable for understanding typical dust properties relative to the shape of the UV continuum. We calculate the UV slopes[10] of PLCKG287+32-2013 and ACT0102-49-2391 from the photometry to be -1.7 ± 1.1 and -1.7 ± 1.3, respectively. For β slopes of these values, following the Meurer et al. (1999) relation for local galaxies, one would expect values of IRX ($\log(L_{IR}/L_{UV})$) of around $\sim 0-1$. However, there has been high scatter observed in this relation, and in fact the $z > 5$ galaxies studied by, e.g., Willott et al. (2015); Capak et al. (2015); Knudsen et al. (2017); Smit et al. (2018); Fudamoto et al. (2020) are found to have lower-than-expected IRX. This decrement is still present even when assuming a steep attenuation law such as SMC, perhaps explained by a higher dust temperature at high redshift.

With capabilities out to 28 microns, *JWST* will revolutionize high-redshift galaxy spectroscopy and imaging and allow us to do detailed analyses of the rest-frame UV and optical spectrum for galaxies in the $z \gtrsim 6$ regime. Notably, spectroscopic (and inferred photometric) measurements of [OIII]+H-β and their strength relative to other rest-frame UV and rest-frame optical emission lines will aid in our understanding of ionization field, ionizing photon production, oxygen abundance and sSFR.

4.7 Conclusions

We present an analysis of new *Spitzer*/IRAC imaging for the high-z candidates in the RELICS survey, providing a full *HST* and *Spitzer* catalog, with galaxy properties, redshifts, and magnifications for 207 galaxies likely at $z \geq 5.5$. We present the distributions of stellar properties of the sample using templates from BC03 and BPASS + nebular emission, and highlight 11 galaxies that have the highest redshifts ($z \geq 6.5$) and at least one S/N detection > 3 in IRAC. We go into further detail for six of those objects. Our main conclusions are as follows:

- While $\sim 95\%$ of our sample are characteristic for their redshift ($L_{UV}/L^{*}_{UV} < 1$), there

---

[10] We calculated beta slopes from the photometry, excluding F105W for PLCKG287+32-2013, which has the potential to for contamination from Lyman-α absorption (if included, the β slope for PLCKG287+32-2013 is -0.4 ± 1.2).

are a few that are intrinsically brighter ($\sim 2L_{UV}/L^{*}_{UV}$). Within our sample, we see a variety of stellar populations, from very small at 2.1×10^5M$_*$ to very massive at 4.2×10^9M$_*$, and from very young (forming $>$ 800Myr after the Big Bang) to very old (forming $<$ 100Myr after the Big Bang).

- Along with this paper, we are releasing our full *HST* + *Spitzer*/IRAC photometric catalog, as well as results from both methods of SED fitting described in this work and magnifications from publicly available lens models.

- We find that PLCKG287+32-2013, one of the brightest $z \sim 7$ candidates known (F160W mag 24.9), has strong evidence for strong [OIII]+H-β emission (EW $\sim$ 1000Å), as suggested by its elevated *Spitzer* [3.6] flux. We believe that this galaxy is experiencing an ongoing burst of star formation.

- We find a similar object, ACT0102-49-2391, which although less luminous, also reveals an elevated [3.6] flux, and falls around $z \sim 6.6 - 6.9$, again suggesting strong nebular emission.

- We find two objects, Abell1763-1434 and RXC0911+17-143, that show evidence for an evolved stellar population, i.e., that they formed very early ($<$ 100 Myr after the Big Bang). We believe that these galaxies show good evidence of Balmer breaks, and their IRAC colors are consistent with evolved (500 Myr) or dusty (E(B-V)=1.00) galaxy models.

- While several of our $z \geq 6.5$ galaxies which are detected in IRAC prefer a nearly maximally old solution, there may be other explanations for their bright *Spitzer* fluxes, such as dust or extreme line emission. Disentangling these degeneracies will only be possible with, e.g., *JWST*, Keck, Thirty Meter Telescope, and/or ALMA observations.

- Through the exploration of SFHs, we find that formation age, which is commonly used as the measure of age in high-redshift galaxy studies, is difficult to constrain. We report it here for comparison with other works, but also present mass-weighted age, a more easily constrained property.

The galaxies presented in this work will be excellent targets for follow-up existing telescopes like Keck and ALMA, as well as with future telescopes such as *James Webb*, Thirty Meter Telescope and Giant Magellan Telescope, as they are apparently bright but intrinsically faint, and likely the dominant galaxy population at these epochs.

Acknowledgements

Based on observations made with the *Spitzer* Space Telescope, which is operated by the Jet Propulsion Laboratory, California Institute of Technology under a contract with NASA. Also based on observations made with the NASA/ESA Hubble Space Telescope, obtained at the Space Telescope Science Institute, which is operated by the Association of Universities for Research in Astronomy, Inc., under NASA contract NAS 5-26555. Support for this work was provided by NASA through ADAP grant 80NSSC18K0945, NSF grant AST 1815458, NASA/HST grant *HST*-GO-14096, and through an award issued by JPL/Caltech. VS also acknowledges support through Heising-Simons Foundation Grant #2018-1140.

This work also refers to observations obtained at the international Gemini Observatory, a program of NSF's OIR Lab, which is managed by the Association of Universities for Research in Astronomy (AURA) under a cooperative agreement with the National Science Foundation on behalf of the Gemini Observatory partnership: the National Science Foundation (United States), National Research Council (Canada), Agencia Nacional de Investigación y Desarrollo (Chile), Ministerio de Ciencia, Tecnología e Innovación (Argentina), Ministério da Ciência, Tecnologia, Inovações e Comunicações (Brazil), and Korea Astronomy and Space Science Institute (Republic of Korea). The guaranteed observations used here were obtained through Ben-Gurion University's (BGU; Israel) time on Gemini, following a MoU between BGU and Gemini/AURA.

Chapter 5

The Dichromatic Primevel Galaxy at $z \sim 7$

This chapter was originally published with the title *RELICS-DP7: Spectroscopic Confirmation of a Dichromatic Primeval Galaxy at $z \sim 7$* in Volume 908 of *The Astrophysical Journal*. As second author, I was responsible for observing the source with Keck/LRIS. I performed the SED fitting and UV β slope analyses, and was responsible for a large part of writing the discussion and analysis of the results.

We report the discovery of a spectroscopically-confirmed strong Lyman-α emitter at $z = 7.0281 \pm 0.0003$, observed as part of the Reionization Cluster Lensing Survey (RELICS). This galaxy, dubbed "Dichromatic Primeval Galaxy" at $z \sim 7$ (DP7), shows two distinct components. While fairly unremarkable in terms of its ultraviolet (UV) luminosity ($\sim 0.3L^*_{UV}$, where L^*_{UV} is the characteristic luminosity), DP7 has one of the highest observed Lyman-α equivalent widths (EWs) among Lyman-α emitters at $z > 6$ (> 200Å in the rest frame). The strong Lyman-α emission generally suggests a young metal-poor, low-dust galaxy; however, we find that the UV slope β of the galaxy as a whole is redder than typical star-forming galaxies at these redshifts, -1.13 ± 0.84, likely indicating, on average, a considerable amount of dust obscuration, or an older stellar population. When we measure β for the two components separately, however, we find evidence of differing UV colors, suggesting two separate stellar populations. Also, we find that Lyman-α is spatially extended and likely larger than the galaxy size, hinting to the possible existence of a Lyman-α halo. Rejuvenation or merging events could explain these results. Either scenario requires an extreme stellar population, possibly including a component of Population III stars, or an obscured Active Galactic Nucleus. DP7, with its low UV luminosity and high Lyman-α EW, represents the typical galaxies that are thought to be the major contribution to the reionization of the Universe, and for this reason DP7 is an excellent target for follow-up with the *James Webb Space Telescope*.

5.1 Introduction

Spectroscopic observations of distant galaxies ($z > 6$) allow us to constrain early galaxy formation and the epoch of reionization. In particular, the λ1215.7Å Lyman-α line is both the strongest recombination line of hydrogen intrinsically and resonantly scattered by neutral hydrogen, making its strength a sensitive gauge of the amount of neutral hydrogen in this epoch. The study of Lyman-α emission in galaxies is commonly used to constrain the neutral fraction of the InterGalactic Medium (IGM) and, hence, different reionization timelines (e.g., Robertson et al., 2015; Mason et al., 2019). Identifying ionized and neutral regions of the IGM not only characterizes the topology of reionization but also allows for the identification of the type of sources that likely drove reionization and the properties of their corresponding ionized bubbles (e.g., Malhotra & Rhoads, 2006; Mason & Gronke, 2020).

Spectroscopic redshift confirmation based on Lyman-α detections has proven increasingly difficult beyond $z > 7$ (e.g., Stark et al., 2010; Pentericci et al., 2014; Schenker et al., 2014; Hoag et al., 2019; Jung et al., 2020). The reason is likely in part due to Lyman-α being scattered away from the line of sight by a patchy neutral medium before reionization was complete (e.g., Treu et al., 2013; Mason et al., 2018b). The exceptions are typically galaxies which have carved out large enough ionized bubbles for Lyman-α emission to escape, allowing it to be observed (e.g., Finkelstein et al., 2013; Zitrin et al., 2015; Oesch et al., 2015; Roberts-Borsani et al., 2016). In addition to adding constraining power to the timing of the epoch of reionization (e.g., Mason et al., 2019; Hoag et al., 2019; Jung et al., 2020), some recent studies have used measurements of Lyman-α strengths and spatial extent to estimate the sizes of these ionized bubbles (e.g., Tilvi et al., 2020), measure ionization parameters (e.g., Matthee et al., 2017b), identify extremely young, metal-poor stellar populations (e.g., Ouchi et al., 2013; Sobral et al., 2015; Matthee et al., 2019, 2020), and identify possible candidates that contain Population III (PopIII) stars (e.g., Sobral et al., 2015; Vanzella et al., 2020). With spectrally-resolved Lyman-α emission, some studies have shown that it is possible to measure the residual neutral fraction within the bubble, the bubble size, as well as physical conditions in galaxies that incite the formation of such bubbles (e.g., Verhamme et al., 2015; Mason & Gronke, 2020).

A large fraction of $z \sim 7$ galaxies with extreme Lyman-α emission consist of multiple components in the rest-frame UV (e.g, Ouchi et al., 2013; Sobral et al., 2015), which makes it difficult to interpret spatially unresolved Lyman-α emission. However, the high incidence of such multi-component systems suggests that mergers or accretion events (e.g, Ouchi et al., 2013; Matthee et al., 2020), which are believed to cause an increase or rejuvenation in star formation, are perhaps a common, if not necessary, condition for such extreme Lyman-α emission. Additionally, most of these galaxies are comparatively more luminous than the characteristic galaxy for their redshift ($L > L^*_{UV}$, where L^*_{UV} is the characteristic luminosity, see, e.g., Matthee et al. 2020), which may be a consequence of clustering effects or an effect of selection.

In this Letter, we present the Dichromatic Primeval Galaxy at $z \sim 7$ (DP7), a UV-faint galaxy ($0.3L/L^*_{UV}$) with multiple components, detected with extreme Lyman-α emission from Keck. In Section 5.2 we describe available data, in Section 5.3 we show the resulting spectrum and analysis of the stellar population in DP7 and we conclude in Section 5.4. Throughout the manuscript, we adopt a Chabrier (2003) initial mass function and a ΛCDM cosmology with $\mathrm{H}_0 = 70$ km s^{-1}, $\Omega_\Lambda = 0.7$, and $\Omega_\mathrm{M} = 0.3$. Magnitudes are given in the AB system. Distances are quoted as proper distances.

5.2 Data

This study is based on data taken from the Reionization Lensing Cluster Survey (RELICS, Coe et al., 2019). RELICS is a 188-orbit *Hubble Space Telescope* (*HST*) Treasury Program targeting 41 massive galaxy clusters at $0.182 \leq z \leq 0.972$. RELICS clusters were observed with the Advanced Camera for Surveys (ACS) and the infrared Wide Field Camera 3 (WFC3/IR) spanning $0.4 - 1.7\mu m$. Details on the survey can be found in Coe et al. (2019). Every RELICS cluster was also observed with *Spitzer*/IRAC by a combination of

RELICS programs (PI Soifer, PI Bradač) and archival ones.

The primary aim of RELICS is to systematically search for lensed high-redshift galaxies in the epoch of reionization. More than 300 candidate galaxies have being discovered with photometric redshifts $z_{phot} > 5.5$, using *HST* and *Spitzer* data (see Salmon et al., 2020, for details about the selection criteria). In this work we focus on one of the high-redshift candidates form the Salmon et al. catalog, namely MS1008-12-427, which we dubbed RELICS-DP7 (i.e., RELICS Dichromatic Primeval galaxy at $z \sim 7$). This object is located behind the $z = 0.306$ MS 1008.1-1224 cluster. We followed this object up with additional *Spitzer*/IRAC data and Keck spectroscopy, which allowed us to better characterize the properties of this galaxy at the epoch of reionization.

5.2.1 HST and Spitzer Data and Photometry

We made use of the *HST* reduced images publicly available via the Mikulski Archive for Space Telescopes (MAST[1]). These were obtained combining all the RELICS and archival ACS (F435W, F606W, F814W) and WFC3/IR (F105W, F125W, F140W, F160W) images available in the MS 1008.1-1224 field of view. Details on the data reduction can be found in Coe et al. (2019). While DP7 was selected for spectroscopy follow-up by using the original Salmon et al. catalog, we have reanalyzed the imaging data for this study.

We run `SExtractor` on the drizzled images with $0.03''$ resolution to produce a photometric catalogs of our galaxy. In addition, we re-run `SExtractor` to deblend the two components that we can clearly see in the F105W image (see Figure 5.1), by setting the deblending parameters to the following: `DEBLEND_MINCONT = 0.00005, DEBLEND_NTHRESH=3`. The WFC3/IR photometry for the two individual components was used, along with the photometry for the entire galaxy, to investigate the stellar properties (see Section 5.3.4).

To derive realistic uncertainties on the fluxes, we accounted for the correlated pixel noise by re-scaling the RMS map that we input in `SExtractor` following the procedure described by Trenti et al. (2011). The re-scaling factor is computed for each *HST* image, and it is such that the median error quoted by `SExtractor` for the photometry in empty sky apertures, of size comparable to our galaxy, is equal to the RMS of the measured flux in the same aperture.

---

[1] https://archive.stsci.edu/prepds/relics/

Following the methodology described in Fuller et al. (2020) (see their Eq.4), we used the F160W apparent magnitude and the k-correction adopted by Fuller et al. to estimate the UV absolute magnitude M_{UV}. This resulted in an $M_{UV} = -19.5 \pm 0.2$ mag for the whole galaxy, corresponding to $0.26L^*_{UV}$, where L^* is the characteristic UV luminosity of a typical galaxy at $z = 7$ from Bouwens et al. (2015a). When we consider the two components separately, M_{UV} is equal to -18.22 ± 0.42 mag for the northern component, and -19.1 ± 0.22 mag for the southern component, corresponding to 0.08 and $0.18L^*_{UV}$, respectively. All the reported values are corrected for magnification (see Section 5.3.1 and Table 5.3.1).

Spitzer/Infrared Array Camera (IRAC) images come from a combination of S-RELICS (PI Bradač, #12005, #14017) and Director's Discretionary Time (PI Soifer, #12123). The MS 1008.1-1224 cluster reached a total of 28 hours of exposure time in each IRAC channel (3.6μm and 4.5μm, [3.6] and [4.5]). To reduce and mosaic Spitzer images, we closely follow the process described by Bradač et al. (2014). We create the mosaic images using the MOsaicker and Point source EXtractor (MOPEX) command-line tools and largely follow the process described in the IRAC Cookbook[2] for the COSMOS medium-deep data.

We extract *Spitzer* fluxes following Strait et al. (2020a). Briefly, we use T-PHOT which was designed to use a high resolution image (in our case, *HST* F160W image and WFC3IR total segmentation) as a prior for reconstructing a model of a low resolution image (in our case, IRAC [3.6] and [4.5]). For field images, T-PHOT is normally run on an entire image at once. However, because background and intracluster light (ICL) varies in a cluster environment, we run T-PHOT individually for each object on a small FOV of 20″. T-PHOT requires a PSF of the low resolution image in order to be convolved with the high resolution image. To create a *Spitzer* PSF for this field, we stack point sources from the field, identified with the stellar locus of a flux radius vs. magnitude plot. We require that there are at least 40 point sources in the making of the PSF (see Strait et al., 2020a, for more detail).

The components of DP7 are too close to separate in *Spitzer*/IRAC, so we only report the fluxes of the combined object.

---

[2] http://irsa.ipac.caltech.edu/data/SPITZER/docs/dataanalysistools/cookbook/

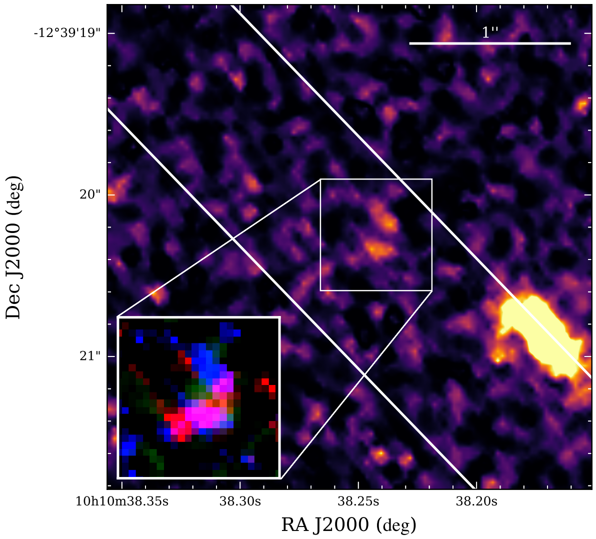

Figure 5.1: *HST* F105W postage stamp (3″×3″) centered on DP7 with superimposed in white the LRIS slit. **Inset:** *HST* color (F105W + F140W + F160W) postage stamp (0.7″×0.7″) showing a southern red component and a northern blue component.

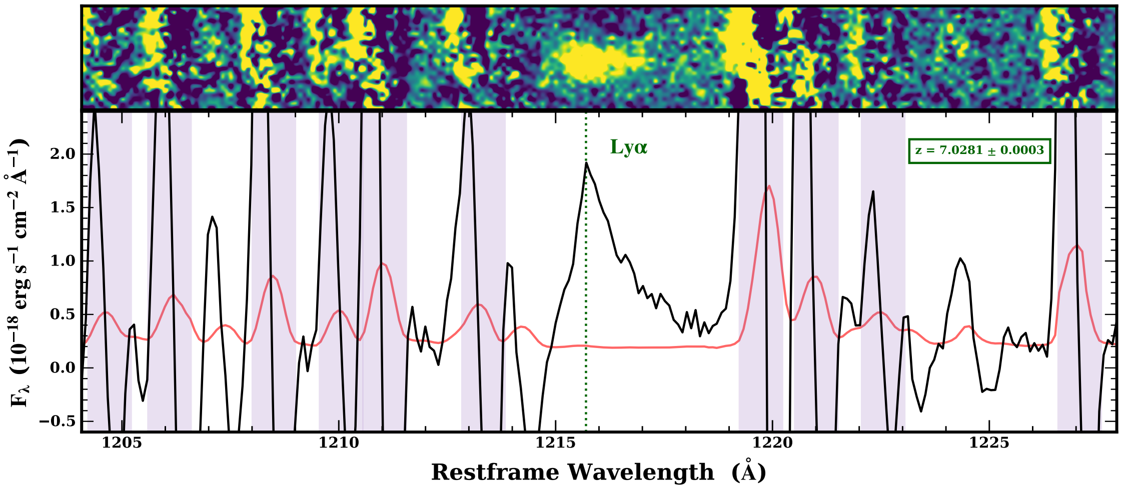

Figure 5.2: DP7's 2D (top) and 1D (bottom) spectrum cutout centered at Lyman-α. The black and red lines show the flux and the noise rest-frame spectrum, respectively. The shaded regions identify the location of the sky lines. For display reasons, we apply a 3 pixel boxcar smoothing filter to the 1D spectrum and noise, and we use a Gaussian interpolation for the 2D spectrum.

5.2.2 Spectroscopy

Spectroscopic follow up of DP7 was carried out with the Low Resolution Imaging Spectrometer (LRIS) on Keck I telescope. Multi-object observations were obtained using $1''$ wide slits over the course of three nights (April 7-9, 2019) for a total of seven hours of integration time (21 frames of 1200s). We used the d680 dichroic, the 300/5000 grism on the blue side covering a range of $\sim 4000 - 7000\,\text{Å}$, and the 600/10000 grating on the red side with a typical wavelength coverage of $\sim 7000 - 10000\,\text{Å}$. Because high-redshift galaxies show spectral features mostly at longer wavelengths (e.g., Lyman-α at $z \geq 6$ has $\lambda_{obs} \geq 8500\,\text{Å}$), we focus here on the data obtained by the red arm of the spectrograph, which provided 2D spectra with an image scale of $0.135''\text{pixel}^{-1}$, a spectral scale of $0.8\text{Å}\,\text{pixel}^{-1}$, and full width at half-maximum (FWHM) spectral resolution of $\sim$4.7Å.

Data reduction was performed using the newly developed open source Python Spectroscopic Data Reduction Pipeline (`PypeIt`; Prochaska et al., 2020). `PypeIt` applies standard reduction techniques to each observed frame: slit's edges tracing, wavelength calibration using arc frames, flat-field correction, and sky subtraction. These steps produce a 2D and 1D spectrum for each frame. The 1D spectra are extracted using the optimal spectrum extraction technique, and then flux calibrated using the standard star Feige 34 observed during the same nights of our science frames. Finally, we stacked all the flux calibrated 1D spectra, as well as the 2D spectra.

We estimated the seeing integrated over the entire exposure time, by identifying a star in our observed mask and determined the FWHM, by fitting a Gaussian function to its spatial profile. We selected our star by searching amongst the most likely point sources from the Probabilistic Classifications of Unresolved Point Sources in PanSTARRS1 (Tachibana & Miller, 2018). We found that the seeing amounted to $0.92'' \pm 0.01''$. We chose not to apply a correction for slit loss due to the possible difference in UV vs. Lyman-α size (see Section 5.3.3). However, it is likely to be fairly small ($\sim$15%, see Lemaux et al. 2009), and any slit loss correction would only serve to increase the estimated line strength and would not meaningfully affect our results.

Inspecting our spectra we found that DP7 shows a prominent Lyman-α emission at $\lambda = 9759.5 \pm 0.4\,\text{Å}$, placing this galaxy at $z = 7.0281 \pm 0.0003$. We determined the redshift by using a χ^2 fitting technique that employed empirical models of lower-redshift ($z \sim 1$) emission line galaxies and high-resolution empirical Lyman-α templates from Lemaux et al. (2009). The spectrum was fit over the wavelength range 9200Å to 10000Å and the redshift was allowed to float over the range $6.5 \leq z \leq 7.1$. Note that limiting the redshift range such that the observed line was forced to be the [OII] λ3726,3729Å doublet resulted in a worse χ^2 (2.95 vs 1.10 for [OII] and Lyman-α, respectively). As an additional check, we estimated the asymmetry of the line profile following the prescription described in Lemaux et al. (2009) and found a value of $1/a_\lambda = 0.28$, where a_λ is the asymmetry parameter. The above tests strongly indicate that the identity of the observed line is Lyman-α. Figure 5.2 shows a cutout of the final reduced 2D and 1D spectrum for DP7 centered at Lyman-α.

From Figure 5.1, which shows the position of the slit on the F105W image, we can see a brighter galaxy to the SW, just at the edge of the slit. Our inspection of the 2D spectrum reveled that this galaxy shows, indeed, a faint but clear Hβ+[OIII] emission at $z = 0.79$. This emission appears to be at $1.01'' \pm 0.08''$ from the Lyman-α emission, which is consistent with the expected distance from the *HST* image, after taking into account an additional uncertainty of $\sim 0.43''$ (approximate major axis of the bright galaxy) on the exact location of the emission within the galaxy.

5.3 Analysis

We describe here the analysis performed to investigate the nature of this high redshift galaxy. A summary of all DP7 properties is reported in Table 5.3.1.

5.3.1 SED Fitting and Lensing Model

To calculate stellar properties of the whole galaxy, we use a set of ∼2000 BC03 stellar population synthesis templates with emission lines. We assume a Chabrier initial mass function between 0.1 and 100 $M_\odot$, a metallicity of $0.2\,Z_\odot$, a constant star formation history, a Small Magellenic Cloud dust law with $\mathrm{E}_*(\mathrm{B\text{-}V}) = \mathrm{E}_{\mathrm{gas}}(\mathrm{E(B\text{-}V)})$ with step sizes of ΔE(B-V)=0.05 for 0-0.5 mag and 0.1 for 0.5-1 mag. We allow age to range from 10 Myr to the age of the universe at the redshift of the source (∼750 Myr). Because nebular emission and continuum can have a non-trivial effect on broadband fluxes (e.g., Smit et al., 2014), we add them by first calculating the hydrogen recombination line strength following the relation from Leitherer & Heckman (1995), scaling from integrated Lyman-continuum flux, and then following the strengths determined with nebular line ratios by Anders & Fritze-v. Alvensleben (2003). In addition to nebular emission, we add Lyman-α to the templates; we calculate expected strengths using the ratio with Hα and assuming a Case B recombination with a Lyman-α escape of 20%.

To correct for the effects of gravitational lensing on the object, we use a lens model of the cluster MS 1008.1-1224 provided by the RELICS team for public use on MAST[3]. This lens model was created using `Lenstool`. The process closely follows that of Cerny et al. (2018) and Sharon et al. (2020). The model uses as constraints four families of multiply-imaged lensed galaxies, two of which are spectroscopically confirmed. We estimated that DP7 is affected by a magnification $\mu = 1.15 \pm 0.02$. The statistical uncertainties on μ are estimated from the magnifications derived from 100 lens models that were sampled from the MCMC chain; the 68% confidence limits are quoted.

5.3.2 Lyα Flux and Equivalent Width

We estimated Lyman-α line flux by inspecting the 1D spectrum and selecting a number of bandpasses. We selected a "feature" bandpass defined to include the spectral line, and four "continuum" bandpasses, two blueward and two redward of the emission line, which are used to estimate the background (since the spectrum doesn't show any stellar continuum emission) across the spectral feature. The "continuum" bandpasses were chosen to be free of sky lines and as close to the emission line in the wavelength direction as the data would allow. We perform a polynomial (order=1) fit to the "continuum" regions to estimate the background across the emission line, and subtracted it from the flux in the "feature" bandpass. The total Lyman-α (Lyα) line flux was measured as:

$$\mathrm{F}_{\mathrm{Ly}\alpha} = \frac{1}{\mu}\sum_{i=0}^{n}(f_{\lambda,i} - b_{\lambda,i})\delta\lambda_i \tag{5.1}$$

where μ is the magnification (Section 5.3.1), $f_{\lambda,i}$, $b_{\lambda,i}$, and $\delta\lambda_i$ are the values of flux, background level and pixel scale (Å pixel^{-1}), respectively, in the ith spectral pixel in the "feature" bandpass. We estimated $\mathrm{F}_{\mathrm{Ly}\alpha}$ to be equal to $1.74 \pm 0.17 \times 10^{-17} \mathrm{erg\,s^{-1}\,cm^{-2}}$, which corresponds to a luminosity $\mathrm{L}_{\mathrm{Ly}\alpha} = 1.0 \pm 0.1 \times 10^{43} \mathrm{erg\,s^{-1}}$.

---

[3] https://archive.stsci.edu/prepds/relics/

Table 5.1. Summary of DP7 Properties

Property	Value
RA (Deg.)	152.6593385
Dec (Deg.)	-12.6556351
z	7.0281 ± 0.0003
μ	1.15 ± 0.2
$\mathrm{M_{stellar}}$ ($10^9 M_\odot$)	$4.9^{+3.8}_{-3.2}$
SFR ($M_\odot \mathrm{yr}^{-1}$)	$11.2^{+10.3}_{-7.2}$
sSFR (Gyr^{-1})	$2.1^{+5.2}_{-2.4}$
E(B-V) (mag)	0.15 ± 0.10
$\mathrm{M_{UV}}$ (mag)	-19.5 ± 0.2
L(Lyα)($\mathrm{erg\,s^{-1}}$)	$1.0 \pm 0.1 \times 10^{43}$
Lyα $\mathrm{EW_{F105W}}$ (Å)	237.12 ± 57.78
Lyα $\mathrm{EW_{F140W}}$ (Å)	341.55 ± 93.78
Lyα FWHM (km $\mathrm{s^{-1}}$)	$285.3^{+23.9}_{-76.4}$
Lyα size (kpc)	2.09 ± 0.88
F160W size (kpc)	0.56 ± 0.20

$^*\mu$ is the magnification factor: median magnification and 68% confidence limits from the MCMC lens model uncertainties. $\mu = \mu_{\mathrm{med}}$ is assumed in SFR, $\mathrm{M_{stellar}}$, and $\mathrm{M_{UV}}$ calculations. Uncertainties include statistical 68% CLs from photometry and redshift. To use a different magnification value, multiply the quantity by $1/f_\mu$, where $f_\mu \equiv \mu/\mu_{\mathrm{med}}$. $\mathrm{M_{stellar}}$ is the intrinsic stellar. sSFR is the specific SFR, sSFR $\equiv M_{stellar}$/SFR. E(B-V) is dust color excess of stellar emission. SMC dust law assumed. $\mathrm{M_{UV}}$ is rest-frame UV magnitude assuming μ_{med}, derived from the observed F160W magnitude including a small template-based k-correction. To use a different magnification value, use $\mathrm{M_{UV}} - 2.5\log(\mathrm{f}_\mu)$. Ly$\alpha$ FWHM is measured non-parametrically by estimating the wavelength at which the line drops to 50% of the peak on the blue and red side. The FWHM error is estimated by a Monte-Carlo technique.

Without a detection of the continuum flux in the spectrum of DP7, we measured the rest-frame equivalent width (EW) for the Lyman-α line in the following way:

$$\mathrm{EW}(\mathrm{Ly}\alpha) = \frac{\mathrm{F}_{\mathrm{Ly}\alpha}}{\mathrm{F}_{\lambda}(1+z)} \tag{5.2}$$

where F_{λ} is the value of the flux density redward of Lyman-α from broad band photometry. We measured EW using both F105W and F140W flux densities for the entire galaxy. Because Lyman-α falls in the F105W band, we subtracted the Lyman-α flux from the broad band flux density. Moreover, we corrected the F105W flux density for the absorption blueward of Lyman-α. When using F105W, we find that EW(Lyα)=237.12 ± 57.78 Å, while if using F140W, EW(Lyα)=341.55 ± 93.78 Å. For completeness, we also measured the EW using the monochromatic flux density from the best-fit SED template just redward of Lyman-α and found a consistent value (∼230Å). These values are to be considered lower limits since we did not integrate to the continuum. Moreover, we did not make a correction for the IGM absorption; therefore, the intrinsic EW is likely be to higher.

5.3.3 Lyα versus F160W spatial extension

We estimated the spatial extent of the Lyman-α emission by collapsing along the spectral direction a portion of the spectrum centered at the emission wavelength, and fitted a Gaussian function to the spatial profile. We determined the intrinsic FWHM of the Lyman-α emission, by subtracting in quadrature the seeing (see 5.2.2), and found a value of 2.09 ± 0.88 kpc.

As a comparison, we determined the galaxy size from the *HST* F160W image. To this end, we obtained the 1D spatial profile of the galaxy along the direction of the slit (see Figure 5.1), and determined the FWHM by fitting a Gaussian function to this profile. After accounting for the F160W point spread function, we found that the galaxy size is 0.56 ± 0.20 kpc. Both sizes are corrected for magnification by multiplying their values by $1/\sqrt{\mu}$.

5.3.4 UV colors and β Slope

From the *HST* color image showed in Figure 5.1 we can clearly see that DP7 constitutes of two components: a southern red component and a northern blue component. This is confirmed by the measured F105W-F160W colors, which are -0.40 ± 0.47 and 0.27 ± 0.30 for

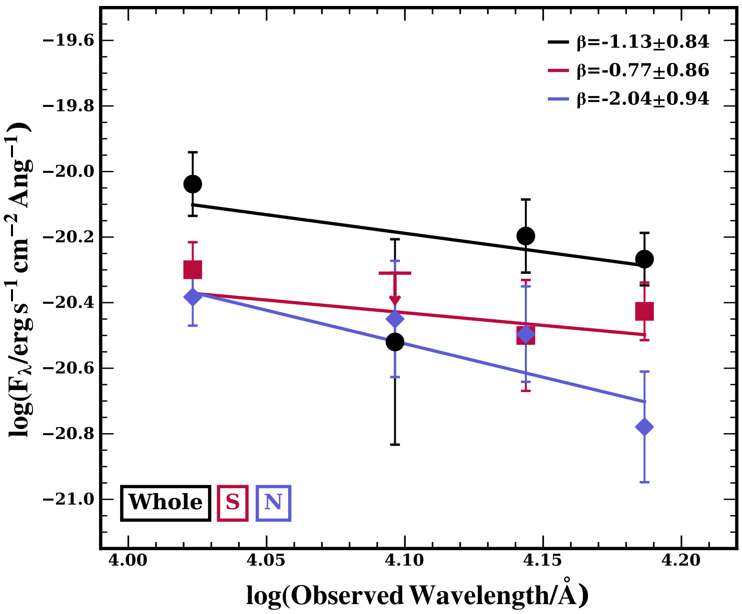

Figure 5.3: UV β slope fits to photometry for the whole (black), southern (red), and northern (blue) components of DP7.

the northern and southern components, respectively. Because F105W flux density is affected by the Lyman-α emission, we also measured F140W-F160W colors, which are -0.48 ± 0.56 and 0.41 ± 0.48, for northern and southern components, respectively.

Another way of characterizing the UV colors is by investigating the slope β of the power-law ($f_\lambda \propto \lambda^\beta$) commonly used to parametrize the galaxy's rest-frame UV continuum. Increasing values of β corresponds to redder galaxies. We measured β for our whole galaxy, as well as for the two individual components identified in the *HST* image, using the values of the flux densities in F105W, F125W, F140W, F160W bands. As done in Section 5.3.2 we corrected the F105W flux density from the whole galaxy for the presence of the Lyman-α, and assuming that the Lyman-α is originated from both northern and southern components, we accordingly scaled F105W flux density from both components. This assumption likely does not represent the reality, but the current Lyman-α spatial resolution does not allow us to determine if it originate solely from one of the two components. We fit a power-law function between flux density and wavelength, although we show it in Figure 5.3 in the logarithmic phase space for better visualization, adopting a least-squares approach that accounts for the uncertainties on the flux density. The uncertainty on β is computed from the covariance matrix. We find that for the whole galaxy $\beta = -1.13 \pm 0.84$. However, when we measure the β slope for the two individual components we find that the northern component has $\beta = -2.04 \pm 0.94$, while the southern component has $\beta = -0.77 \pm 0.86$. Note that both for the calculation of the colors and β slopes, we did not explicitly PSF match the various WFC3 images, though the relative difference of the components remains unchanged if we make this correction. The above β values are consistent, though with a slightly reduced significance (1σ), with the measured color difference, implying the existence of a bluer and redder component in DP7 that have different properties in their stellar populations and/or their dust content (see, e.g., Bouwens et al., 2009; Fudamoto et al., 2020).

5.4 Discussion and Conclusions

We report the discovery of DP7, a Dichromatic Primeval galaxy within the RELICS survey, spectroscopically confirmed at $z = 7.0281 \pm 0.0003$ using observations carried out with Keck/LRIS. We detect a strong Lyman-α emission with rest-frame EW~ 300Å, depending on the assumed continuum. The EWs measured here are to be considered lower limits since we did not integrate to the continuum in our observations, and we did not correct for IGM absorption, which is likely to be very severe for an average galaxy at these redshifts.

We find that Lyman-α is spatially extended (2.09 ± 0.88 kpc) and likely larger than the galaxy size (0.56 ± 0.20 kpc, from the *HST*/F160W image), hinting to the possible existence of a Lyman-α halo. However, we cannot determine if the center of the Lyman-α emission coincides with the center of the UV continuum emission, due to the spatial resolution of the ground-based data used to measure the Lyman-α emission.

Moreover, DP7 appears dichromatic, since it is comprised of two components (see Figure 5.1) that likely have different stellar and/or dust properties. This difference is implied by the different UV colors of the two components and, with a smaller significance, by the β slope measurements (see Section 5.3.4), with the northern component exhibiting bluer colors ($\beta = -2.04$) and the southern component exhibits redder colors ($\beta = -0.77$).

A few recent studies have reported the spectroscopic confirmation of $z \sim 7$ galaxies with properties similar to DP7, i.e, strong Lyman-α emission (EW$\gtrsim 100$Å), spatially extended Lyman-α, and/or multiple components. Sobral et al. (2015) and Matthee et al. (2019) discuss MASOSA, a $z = 6.5$ source with Lyman-α EW> 100Å. Although MASOSA has very luminous Lyman-α, the dust continuum and [CII] $\lambda158\mu$m line are not detected in Atacama Large Millimeter/submillimeter Array (ALMA) observations, implying a likely young, metal-poor stellar population. Sobral et al. (2015) and Matthee et al. (2020) discuss CR7, a galaxy at $z = 6.6$ with strong spatially extended Lyman-α halo, surrounding at least three UV components of differing color, with the redder components dominating the mass and the bluer component dominating the Lyman-α emission. These authors argue that the Lyman-α EW for both MASOSA and CR7 can be explained by a young metal-poor starburst with a possible, but not necessary, contribution from PopIII-like stellar populations. However, Vanzella et al. (2020), who report the discovery of a highly magnified arc with intrinsic Lyman-α EW$\,>1120$Å, argue that a PopIII stellar complex is required for emission in excess of EW(Lyman-α)$\gtrsim$400Å, a value which DP7 possibly exceeds when accounting for the IGM absorption. Other examples of strong (although not so extreme) extended Lyman-α at $z \sim 7$ are presented by Ouchi et al. (2013), who discovered a Lyman-α halo surrounding a luminous star-forming galaxy ('Himiko') at $z = 6.6$. 'Himiko' is a very metal poor system and is composed by three clumps undergoing a triple merger, likely powering the Lyman-α emission. Hu et al. (2016) and Matthee et al. (2018) report on the discovery of COLA1 at $z \sim 6.6$. COLA1 is one of the brightest Lyman-α emitters at the epoch of reionization, with a Lyman-α luminosity of $L_{\mathrm{Ly}\alpha} = 4.1 \times 10^{43}$ ergs s^{-1} and a Lyman-α EW of $\sim$120Å. These extreme properties are attributed to an extremely low gas-phase metallicity, a large ionized bubble powered by COLA1, and the possible inflow of gas. Finally, Tilvi et al. (2020) presented evidence for the existence of overlapping Lyman-α ionized bubbles from a grouping of three galaxies at $z = 7.7$, however, no claims are made about the metallicity of these systems.

All of these previous works suggest that extended Lyman-α emission with strength similar to what seen in DP7 originates from galaxies that are young and very metal poor (with a possible contribution from PopIII systems), have multiple components/companions, and/or are undergoing a merger or accretion event. Interestingly, DP7 stands out from the UV bright galaxies with strong Lyman-α emission that are the subjects of the above studies in that it is one of the UV fainter galaxies spectroscopically-confirmed at these redshifts, with $L_{UV}/L^{*}_{UV} \sim 0.3$. There are only a few other examples of galaxies at these redshifts that approach the UV faintness of DP7 and have similarly extreme Lyman-α (Larson et al., 2018; Jung et al., 2020). UV faint galaxies are typically thought to be the types of galaxies that reionized the universe (e.g, Sawicki & Thompson 2006); however, recent studies (e.g., Stark et al., 2017; Mason et al., 2018a) have suggested that reionization may be accelerated around the brightest galaxies. If systems such as DP7 are common and found without brighter companions, this could provide evidence in favor of UV faint galaxies as drivers of the reionization.

Possible scenarios for DP7 include (1) an evolved, dusty galaxy experiencing rejuvenation due to new star-forming activity and (2) a merger event between an evolved, dusty component and a younger, star-forming component. In either scenario, the strong, spatially extended Lyman-α emission is likely evidence of an ionized bubble explained by metal-poor star formation, with a possible contribution from PopIII stars. Investigation of the larger scale environment would allow us to look for nearby UV bright galaxies that may have carved out a bubble (e.g., Tilvi et al., 2020). Additionally, measuring the velocity offset between Lyman-α and systemic would allow us to probe for the presence of an ionized bubble (Mason & Gronke, 2020). Unobscured AGN activity, instead, is ruled out due to the narrow width (see Table 5.3.1) of Lyman-α emission. However, other types of AGN activity cannot be ruled out from these observations, including the presence or absence of the NV λ1240Å feature (see, e.g., Mainali et al. 2018), which is predicted to be coincident with a sky line in the LRIS spectra.

The results obtained from the observations of DP7 thus far are tantalizing but, ultimately, ambiguous. More comprehensive and deeper data are needed to understand the physical processes involved in powering such a strong Lyman-α emission, and to discriminate between the proposed scenarios. Spectral observations in the near infrared to detect or constrain features such as CIV (λ1549Å), HeII (λ1640Å), and CIII] (λ1907,1909Å) would help illuminate the source powering the Lyman-α emission including the presence of certain types of AGN activity (see Nakajima et al. 2018; Le Fèvre et al. 2019). *James Webb Space Telescope* will be crucial in the study of galaxies at the epoch of reionization, in particular the IFU NIRSpec spectrograph would allow to spatially map rest-frame optical emission lines, which are very likely to be extremely strong given our lower limit on the Lyman-α intrinsic strength (though metallicity effects may reduce the strength of, e.g., the λ5007Å [OIII] emission, see, e.g., Matthee et al. 2018). These observations will provide spatial distribution of star formation, ionization parameter, metallicity, and dust. Moreover, ALMA would allow us to obtain high spatial resolution observations of, e.g., [CII] emission, which can be used to better constrain the separation between the two DP7 components and investigate merger scenarios through galaxy kinematics (see, e.g., Ginolfi et al. 2020). Fully probing the nature of sources such as DP7 with such observations is key to understanding reionization since these types of galaxies likely represent those that make the primary contribution to the reionization of the Universe.

Support for this work was provided by NASA through NSF grant AST 1815458, NASA ADAP grant 80NSSC18K0945, NASA *HST* grant *HST*-GO-14096, and through an award issued by JPL/Caltech. VS also acknowledges support through Heising-Simons Foundation Grant #2018-1140. Data presented here is part of the RELICS *Hubble* Treasury Program (GO 14096), which consists of observations obtained by the NASA/ESA *Hubble Space Telescope (HST). Hubble* is operated by the Association of Universities for Research in Astronomy, Inc. (AURA), under NASA contract NAS5-26555. Data from the NASA/ESA *Hubble Space Telescope* presented in this paper were obtained from the Mikulski Archive for Space Telescopes (MAST), operated by the Space Telescope Science Institute (STScI). STScI is operated by the Association of Universities for Research in Astronomy, Inc. (AURA) under NASA contract NAS 5-26555. The *Hubble* Advanced Camera for Surveys (ACS) was developed under NASA contract NAS 5-32864. *Spitzer Space Telescope* data presented in this paper were obtained from the NASA/IPAC Infrared Science Archive (IRSA), operated by the Jet Propulsion Laboratory, California Institute of Technology. Spitzer and IRSA are operated by the Jet Propulsion Laboratory, California Institute of Technology under contract with NASA. The spectroscopic data presented herein were obtained at the W.M. Keck Observatory, which is operated as a scientific partnership among the California Institute of Technology, the University of California, and the National Aeronautics and Space Administration. The Observatory was made possible by the generous financial support of the W.M. Keck Foundation. We thank the indigenous Hawaiian community for allowing us to be guests on their sacred mountain, a privilege, without which, this work would not have

been possible. We are most fortunate to be able to conduct observations from this site.

Chapter 6

Summary and Future Directions

In this dissertation, I have discussed my contributions to the field of high-redshift galaxy evolution and the study of the Epoch of Reionization. Because faint galaxies are likely the drivers of reionization of the universe, galaxy cluster-scale lensing is an excellent tool to select for faint galaxies that would otherwise be below the detection limits of current facilities. I discuss the nuances, uncertainties, and strengths of gravitational lensing models, and outline the process of creating one for the Hubble Frontier Fields cluster, Abell 370. In the subsequent chapters, I discuss the results from another lensing survey, RELICS. In Chapters 3 and 4, I detail the process of galaxy discovery in lensing fields and the process of constraining physical properties of galaxies using imaging and SED fitting, and identify several interesting galaxies, including extreme line emitters and candidate evolved populations at high redshift. In Chapter 5, I detail a detection of extreme Lyα emission in a $z \sim 7$ galaxy.

6.1 Future of the Field

The work in this dissertation, like so much of the work done in the field of EoR galaxy science, is focused on preparing for the upcoming flight of the *James Webb Space Telescope*. The launch date is currently set for November 2021, and the Guaranteed Time Observations, Early Release Science programs, and Cycle 1 programs have been set. The galaxy-centric programs are generally focused on a combination of deep spectroscopic observations and wide photometric observations of well-studied fields, with the goal of high redshift galaxy discovery and characterization. The *Hubble Space Telescope* and *Spitzer Space Telescope* have given us some glimpses of the ultra-high-redshift universe with detections of galaxies at $z \sim 10-11$, but *JWST* will quickly surpass the observational limits of *Hubble* and *Spitzer* by many magnitudes, allowing for galaxy discovery beyond $z \sim 12$. The first *JWST* programs, which include observations of blank fields (e.g., CEERS, PI Steve Finkelstein) and lensed fields (e.g., GLASS, PI Tommaso Treu and CANUCS, PI Willott), will make strides forward in some of the main goals of Epoch of Reionization galaxy science. They will increase galaxy number counts out to $z \sim 12$ in order to construct luminosity functions, study stellar mass buildup of galaxies as far back as 300 Myr after the Big Bang, and study a plethora of characteristics of galaxies, including but certainly not limited to: quenching processes, morphologies, chemical enrichment, feedback processes, ionizing photon production, age, and dust growth.

One of the main advantages of a large, cold telescope in space is its capability to observe in the infrared, opening up the Balmer/4000Å break section of $z \sim 6$ galaxies and allowing for accurate measurements of stellar populations of galaxies. Measurements of stellar mass, star formation rate, age, dust, etc. of high-redshift galaxies will be much more precise with *JWST*. In the same way that I have performed SED fitting in Chapters 3 and 4 of this dissertation using *HST* and *Spitzer* fluxes, SED fitting with imaging from *JWST* will be done. *JWST* imaging alone will improve upon these sorts of measurements by an order of magnitude reduction in uncertainties. While much of the work in this dissertation is based on imaging data, future spectroscopic observations will improve on current results: imaging is vital and necessary for an initial glance at a large number of candidate high redshift galaxies, but without spectroscopy, we can decidedly not make robust scientific claims. *JWST*'s spectroscopic capabilities will allow, for the first time, direct measurements of nebular emission in high-redshift galaxies, and measurements of ionization, metallicity, and dust. The Integral Field Unit on *JWST*'s NIRSpec will even allow for sub-galaxy scale measurements of these quantities.

In short, *JWST* will alter the field as we know it, answering so much of what we would like to know about the Epoch of Reionization, including the timeline, what sources are responsible, when the first stars formed, and the detailed properties of galaxies in that period of time. We will undoubtedly also be presented with new questions and challenges that are impossible to predict.

6.2 Future Plans

After my PhD work which focuses mainly on imaging data, I have become interested in doing detailed case studies on single galaxies with the goal of exploring the nature of ionizing sources, Lyα emission, and star formation. In this vein, I have proposed for *JWST* and ALMA time to gain a better understanding of DP7, the extreme Lyα emitter discussed in Chapter 5. The galaxy is interesting because in spite of its strong Lyα emission, it is intrinsically faint, and also shows evidence of a red UV β slope and possibly two separate UV components. With spatially-resolved rest-optical data with *JWST*, we will be able to understand the Lyα emission mechanisms in the galaxy, measure the system's kinematics, and robustly constrain properties of the ionizing source in DP7 itself and its immediate environment. With a detection of [CII] using the Atacama Large Millimeter Array (ALMA), we can explore the physics of the interstellar medium of DP7, studying the mechanism of star formation from a different angle. I am excited about these types of studies with *JWST* and ALMA for both unique and characteristic galaxies, both with my own proposed data, and with the exciting *JWST* Early Release Science programs that will target high-z galaxies in both blank fields and lensing fields, starting in 2022.

I have also come to appreciate the many uncertainties, both statistical and systematic, but especially the latter, associated with the process of SED fitting. This has led to an existential crisis or two about whether we actually know anything at all about high-redshift galaxies. As many scientists have done in the past, I have come to accept these large and unknowable (for now) systematic uncertainties (associated with, e.g., choice of Initial Mass Function). However, with the imminent flight of *JWST*, there is going to be a large increase in the ability to constrain one uncertainty in particular: the star formation histories of early galaxies.

One of the most unconstrained parameters in galaxy modeling is the galaxy's star formation history. There have been several studies of SFH at low-z (e.g., Tolstoy et al., 2009; Weisz et al., 2014; Pacifici et al., 2016; Carnall et al., 2019; Lower et al., 2020; Estrada-Carpenter et al., 2020), but very few that focus on galaxies in the EoR (e.g., Laporte et al., 2021). This is likely due to the paucity of data at high-z and the short period of time that high redshift galaxies have to evolve (for example, at $z \sim 8$ the universe is only 400 Myr old). However, with the upcoming flight of *JWST*, we will see a great increase in both quality and quantity of data for high redshift galaxies.

To prepare for these data, I am executing a set of experiments with simulated galaxies to test which data, and of what quality, will be necessary to constrain a galaxy's star formation history at high redshift. Armed with information about the burstiness, general shape, and sometimes detailed SFH of a galaxy, we will be able to understand the mass buildup of galaxies at the earliest times in the universe; past even the detection limit of future telescopes in some cases. I am currently using two distinct types of simulated galaxies: one set from the high-z suite of the FIRE simulations (Ma et al., 2019, 2020a,b) and another set from the Renaissance Simulations (Barrow et al., 2018).

I will be starting as a Dawn Fellow at the Niels Bohr Institute in September, and am excited for the possibilities for collaboration that this opportunity offers. I am excited to continue working with people that have been a part of this dissertation, and I am excited to see what the future of this field will bring.

REFERENCES

Acebron, A. et al. 2019a, ApJ, 874, 132, _eprint: 1810.08122

——. 2018, ApJ, 858, 42, _eprint: 1803.00560

——. 2019b, arXiv e-prints, arXiv:1912.02702, _eprint: 1912.02702

Amorín, R. et al. 2014, A&A, 568, L8, _eprint: 1403.3692

Anders, P., & Fritze-v. Alvensleben, U. 2003, A&A, 401, 1063, _eprint: astro-ph/0302146

Bahcall, N. A., & Kulier, A. 2014, MNRAS, 439, 2505, _eprint: 1310.0022

Bakx, T. J. L. C. et al. 2020, MNRAS, 493, 4294, _eprint: 2001.02812

Barrow, K. S. S., Aykutalp, A., & Wise, J. H. 2018, Nature Astronomy, 2, 987, _eprint: 1809.03526

Beardsley, A. P. et al. 2016, ApJ, 833, 102, 1608.06281

Becker, G. D., Bolton, J. S., & Lidz, A. 2015, Publications of the Astronomical Society of Australia, 32, e045

Bell, E. F., McIntosh, D. H., Katz, N., & Weinberg, M. D. 2003, ApJS, 149, 289, _eprint: astro-ph/0302543

Bertin, E., & Arnouts, S. 1996, A&AS, 117, 393

Bouwens, R. J. et al. 2014, ApJ, 795, 126, _eprint: 1211.2230

——. 2009, ApJ, 705, 936, _eprint: 0909.4074

Bouwens, R. J., Illingworth, G. D., Oesch, P. A., Caruana, J., Holwerda, B., Smit, R., & Wilkins, S. 2015a, ApJ, 811, 140, _eprint: 1503.08228

Bouwens, R. J. et al. 2015b, ApJ, 803, 34, _eprint: 1403.4295

Bouwens, R. J., Oesch, P. A., Illingworth, G. D., Ellis, R. S., & Stefanon, M. 2017, ApJ, 843, 129, _eprint: 1610.00283

Bouwens, R. J. et al. 2016, ApJ, 830, 67, _eprint: 1506.01035

Bouwens, R. J., Stefanon, M., Oesch, P. A., Illingworth, G. D., Nanayakkara, T., Roberts-Borsani, G., Labbe', I., & Smit, R. 2019, arXiv e-prints, _eprint: 1905.05202

Bowman, J. D., Rogers, A. E. E., Monsalve, R. A., Mozdzen, T. J., & Mahesh, N. 2018, Nature, 555, 67, _eprint: 1810.05912

Bradač, M. 2020, Nature Astronomy, 4, 478, _eprint: 2005.07248

Bradač, M. et al. 2005, A&A, 437, 49

——. 2017, ApJ, 836, L2, _eprint: 1610.02099

——. 2019, MNRAS, 489, 99, _eprint: 1906.01725

——. 2014, ApJ, 785, 108, _eprint: 1402.2352

——. 2009, ApJ, 706, 1201, _eprint: 0910.2708

Bradley, L. D. et al. 2014, ApJ, 792, 76, _eprint: 1308.1692

Brammer, G. B. et al. 2016, ApJS, 226, 6, _eprint: 1606.07450

Brammer, G. B., van Dokkum, P. G., & Coppi, P. 2008, ApJ, 686, 1503, _eprint: 0807.1533

Bridge, J. S. et al. 2019, ApJ, 882, 42, _eprint: 1907.05512

Brocklehurst, M. 1971, MNRAS, 153, 471

Bruzual, G., & Charlot, S. 2003, MNRAS, 344, 1000, _eprint: astro-ph/0309134

Burke, C., Hilton, M., & Collins, C. 2015, MNRAS, 449, 2353, _eprint: 1503.04321

Calzetti, D., Armus, L., Bohlin, R. C., Kinney, A. L., Koornneef, J., & Storchi-Bergmann, T. 2000, ApJ, 533, 682, _eprint: astro-ph/9911459

Capak, P. L. et al. 2015, Nature, 522, 455, _eprint: 1503.07596

Caputi, K. I. et al. 2017, ApJ, 849, 45, _eprint: 1705.06179

Carnall, A. C., Leja, J., Johnson, B. D., McLure, R. J., Dunlop, J. S., & Conroy, C. 2019, ApJ, 873, 44, _eprint: 1811.03635

Carnall, A. C., McLure, R. J., Dunlop, J. S., & Davé, R. 2018, MNRAS, 480, 4379, _eprint: 1712.04452

Casey, C. M., Narayanan, D., & Cooray, A. 2014, Phys. Rep., 541, 45, 1402.1456

Castellano, M. et al. 2016a, A&A, 590, A31, _eprint: 1603.02461

——. 2016b, ApJ, 823, L40, _eprint: 1605.01524

Cerny, C. et al. 2018, ApJ, 859, 159, _eprint: 1710.09329

Chabrier, G. 2003, PASP, 115, 763, _eprint: astro-ph/0304382

Chisholm, J., Prochaska, J. X., Schaerer, D., Gazagnes, S., & Henry, A. 2020, MNRAS, 498, 2554, _eprint: 2008.06059

Christensen, L. et al. 2012, MNRAS, 427, 1973, _eprint: 1209.0775

Cibirka, N. et al. 2018, ApJ, 863, 145, _eprint: 1803.09557

Coe, D. et al. 2019, ApJ, 884, 85, _eprint: 1903.02002

Cuby, J. G., Hibon, P., Lidman, C., Le Fèvre, O., Gilmozzi, R., Moorwood, A., & van der Werf, P. 2007, A&A, 461, 911, astro-ph/0611272

Dahlen, T. et al. 2013, ApJ, 775, 93, _eprint: 1308.5353

Dayal, P., & Ferrara, A. 2018, Phys. Rep., 780, 1, _eprint: 1809.09136

De Barros, S., Oesch, P. A., Labbé, I., Stefanon, M., González, V., Smit, R., Bouwens, R. J., & Illingworth, G. D. 2019, MNRAS, 489, 2355, _eprint: 1903.09649

DeBoer, D. R. et al. 2017, PASP, 129, 045001, 1606.07473

Di Criscienzo, M. et al. 2017, A&A, 607, A30, _eprint: 1706.03790

Diego, J. M. et al. 2018, MNRAS, 473, 4279, _eprint: 1609.04822

Duncan, K. J., Shivaei, I., Shapley, A. E., Reddy, N. A., Mobasher, B., Coil, A. L., Kriek, M., & Siana, B. 2020, arXiv e-prints, arXiv:2008.04329, _eprint: 2008.04329

Ebeling, H., Qi, J., & Richard, J. 2017, MNRAS, 471, 3305, _eprint: 1706.03535

Egami, E. et al. 2005, ApJ, 618, L5, _eprint: astro-ph/0411117

Eldridge, J. J., Izzard, R. G., & Tout, C. A. 2008, MNRAS, 384, 1109, _eprint: 0711.3079

Eldridge, J. J., & Stanway, E. R. 2009, MNRAS, 400, 1019, _eprint: 0908.1386

Endsley, R., Stark, D. P., Chevallard, J., & Charlot, S. 2020a, arXiv e-prints, arXiv:2005.02402, _eprint: 2005.02402

Endsley, R., Stark, D. P., Chevallard, J., Charlot, S., Robertson, B., Bouwens, R. J., & Stefanon, M. 2020b, arXiv e-prints, 2010, arXiv:2010.03566

Erben, T., Van Waerbeke, L., Bertin, E., Mellier, Y., & Schneider, P. 2001, A&A, 366, 717, _eprint: astro-ph/0007021

Estrada-Carpenter, V. et al. 2020, The Astrophysical Journal, 898, 171

Eyles, L. P., Bunker, A. J., Stanway, E. R., Lacy, M., Ellis, R. S., & Doherty, M. 2005, MNRAS, 364, 443, _eprint: astro-ph/0502385

Faisst, A. L. et al. 2016, ApJ, 821, 122, _eprint: 1601.07173

Faisst, A. L., Capak, P. L., Emami, N., Tacchella, S., & Larson, K. L. 2019, ApJ, 884, 133, _eprint: 1909.03076

Fan, X., Carilli, C. L., & Keating, B. 2006, ARA&A, 44, 415, _eprint: astro-ph/0602375

Ferland, G. J. et al. 2017, Revista Mexicana de Astronomía y Astrofísica, 53, 385, _eprint: 1705.10877

Feroz, F., & Hobson, M. P. 2008, MNRAS, 384, 449, _eprint: 0704.3704

Feroz, F., Hobson, M. P., & Bridges, M. 2009, MNRAS, 398, 1601, _eprint: 0809.3437

Feroz, F., & Skilling, J. 2013, in American Institute of Physics Conference Series, Vol. 1553, American Institute of Physics Conference Series, ed. U. von Toussaint, 106–113, _eprint: 1312.5638

Finkelstein, S. L. et al. 2019, The Astrophysical Journal, 879, 36

——. 2013, Nature, 502, 524, _eprint: 1310.6031

——. 2015, ApJ, 810, 71, _eprint: 1410.5439

Finney, E. Q. et al. 2018, ApJ, 859, 58

Fletcher, T. J., Tang, M., Robertson, B. E., Nakajima, K., Ellis, R. S., Stark, D. P., & Inoue, A. 2019, The Astrophysical Journal, 878, 87

Franx, M., Illingworth, G. D., Kelson, D. D., van Dokkum, P. G., & Tran, K.-V. 1997, ApJ, 486, L75, astro-ph/9704090

Fudamoto, Y. et al. 2020, arXiv e-prints, arXiv:2004.10760, _eprint: 2004.10760

Fuller, S. et al. 2020, ApJ, 896, 156, _eprint: 2002.08952

Furlanetto, S. R., McQuinn, M., & Hernquist, L. 2006, Monthly Notices of the Royal Astronomical Society, 365, 115

Ginolfi, M. et al. 2020, A&A, 633, A90, _eprint: 1910.04770

Girard, M., Dessauges-Zavadsky, M., Schaerer, D., Richard, J., Nakajima, K., & Cava, A. 2018, A&A, 619, A15, _eprint: 1809.01162

Gonzalez, A. H., Sivanandam, S., Zabludoff, A. I., & Zaritsky, D. 2013, ApJ, 778, 14, _eprint: 1309.3565

González, V., Labbé, I., Bouwens, R. J., Illingworth, G., Franx, M., & Kriek, M. 2011, ApJ, 735, L34, _eprint: 1008.3901

Gunn, J. E., & Peterson, B. A. 1965, The Astrophysical Journal, 142, 1633

Hammer, F. 1987, in High Redshift and Primeval Galaxies, ed. J. Bergeron, D. Kunth, B. Rocca-Volmerange, & J. Tran Thanh Van, 467–473

Hammer, F., & Rigaut, F. 1989, A&A, 226, 45

Hashimoto, T. et al. 2018, Nature, 557, 392, _eprint: 1805.05966

Hayes, M. et al. 2010, Nature, 464, 562, _eprint: 1002.4876

Hoag, A. et al. 2018, ApJ, 854, 39, _eprint: 1709.03992

——. 2019, ApJ, 878, 12, _eprint: 1901.09001

——. 2016, ApJ, 831, 182, _eprint: 1603.00505

Hoekstra, H., Franx, M., Kuijken, K., & Squires, G. 1998, ApJ, 504, 636

Hu, E. M., Cowie, L. L., Songaila, A., Barger, A. J., Rosenwasser, B., & Wold, I. G. B. 2016, ApJ, 825, L7, _eprint: 1606.03526

Huang, K.-H. et al. 2016a, ApJ, 817, 11, _eprint: 1504.02099

——. 2016b, ApJ, 823, L14, _eprint: 1605.05771

Hutchison, T. A. et al. 2019, ApJ, 879, 70, _eprint: 1905.08812

Ishigaki, M., Kawamata, R., Ouchi, M., Oguri, M., Shimasaku, K., & Ono, Y. 2018, ApJ, 854, 73, _eprint: 1702.04867

Izotov, Y. I., Guseva, N. G., Fricke, K. J., Henkel, C., Schaerer, D., & Thuan, T. X. 2021, Astronomy and Astrophysics, 646, A138

Izotov, Y. I., Orlitová, I., Schaerer, D., Thuan, T. X., Verhamme, A., Guseva, N. G., & Worseck, G. 2016a, Nature, 529, 178

Izotov, Y. I., Schaerer, D., Thuan, T. X., Worseck, G., Guseva, N. G., Orlitová, I., & Verhamme, A. 2016b, Monthly Notices of the Royal Astronomical Society, 461, 3683

Izotov, Y. I., Schaerer, D., Worseck, G., Guseva, N. G., Thuan, T. X., Verhamme, A., Orlitová, I., & Fricke, K. J. 2018a, Monthly Notices of the Royal Astronomical Society, 474, 4514

Izotov, Y. I., Worseck, G., Schaerer, D., Guseva, N. G., Thuan, T. X., Fricke, Verhamme, A., & Orlitová, I. 2018b, MNRAS, 478, 4851, _eprint: 1805.09865

Jauzac, M. et al. 2016, MNRAS, 457, 2029, _eprint: 1509.08914

Johnson, T. L., & Sharon, K. 2016, ApJ, 832, 82, _eprint: 1608.08713

Johnson, T. L., Sharon, K., Bayliss, M. B., Gladders, M. D., Coe, D., & Ebeling, H. 2014, ApJ, 797, 48, _eprint: 1405.0222

Jones, T., Sanders, R., Roberts-Borsani, G., Ellis, R. S., Laporte, N., Treu, T., & Harikane, Y. 2020, arXiv e-prints, arXiv:2006.02447, _eprint: 2006.02447

Jones, T. et al. 2015, AJ, 149, 107, _eprint: 1410.0967

Jullo, E., & Kneib, J.-P. 2009, MNRAS, 395, 1319, _eprint: 0901.3792

Jung, I. et al. 2020, arXiv e-prints, arXiv:2009.10092, _eprint: 2009.10092

Kaiser, N., Squires, G., & Broadhurst, T. 1995, ApJ, 449, 460, _eprint: astro-ph/9411005

Kauffmann, G., & Charlot, S. 1998, MNRAS, 297, L23, _eprint: astro-ph/9802233

Kawamata, R., Ishigaki, M., Shimasaku, K., Oguri, M., Ouchi, M., & Tanigawa, S. 2018, ApJ, 855, 4, _eprint: 1710.07301

Kneib, J. P., Mellier, Y., Fort, B., & Mathez, G. 1993, A&A, 273, 367

Knudsen, K. K., Watson, D., Frayer, D., Christensen, L., Gallazzi, A., Michalowski, M. J., Richard, J., & Zavala, J. 2017, MNRAS, 466, 138, _eprint: 1603.03222

Koester, B. P. et al. 2007, ApJ, 660, 239, _eprint: astro-ph/0701265

Labbé, I. et al. 2010, ApJ, 708, L26, _eprint: 0910.0838

——. 2013, ApJ, 777, L19, _eprint: 1209.3037

Lagattuta, D. J. et al. 2017, MNRAS, 469, 3946, _eprint: 1611.01513

Laidler, V. G. et al. 2007, PASP, 119, 1325

Laporte, N., Meyer, R. A., Ellis, R. S., Robertson, B. E., Chisholm, J., & Roberts-Borsani, G. W. 2021, arXiv e-prints, 2104, arXiv:2104.08168

Laporte, N. et al. 2014, A&A, 562, L8, _eprint: 1401.8263

Larson, R. L. et al. 2018, ApJ, 858, 94, _eprint: 1712.05807

Le Fèvre, O. et al. 2019, arXiv e-prints, arXiv:1910.09517, _eprint: 1910.09517

Lee, S.-K., Idzi, R., Ferguson, H. C., Somerville, R. S., Wiklind, T., & Giavalisco, M. 2009, ApJS, 184, 100, _eprint: 0812.5111

Leethochawalit, N., Jones, T. A., Ellis, R. S., Stark, D. P., Richard, J., Zitrin, A., & Auger, M. 2016, ApJ, 820, 84, _eprint: 1509.01279

Leitherer, C., & Heckman, T. M. 1995, ApJS, 96, 9

Leja, J., Carnall, A. C., Johnson, B. D., Conroy, C., & Speagle, J. S. 2019, ApJ, 876, 3, _eprint: 1811.03637

Lemaux, B. C. et al. 2009, ApJ, 700, 20, _eprint: 0905.2233

Livermore, R. C., Finkelstein, S. L., & Lotz, J. M. 2017, ApJ, 835, 113, _eprint: 1604.06799

Lotz, J. M. et al. 2017, ApJ, 837, 97, _eprint: 1605.06567

Lower, S., Narayanan, D., Leja, J., Johnson, B. D., Conroy, C., & Davé, R. 2020, arXiv e-prints, arXiv:2006.03599, _eprint: 2006.03599

Luppino, G. A., & Kaiser, N. 1997, ApJ, 475, 20, _eprint: astro-ph/9601194

Lynds, R., & Petrosian, V. 1986, in BAAS, Vol. 18, Bulletin of the American Astronomical Society, 1014

Lynds, R., & Petrosian, V. 1989, ApJ, 336, 1

Ma, X. et al. 2020a, MNRAS, 493, 4315, _eprint: 1906.11261

——. 2019, MNRAS, 487, 1844, _eprint: 1902.10152

Ma, X., Quataert, E., Wetzel, A., Hopkins, P. F., Faucher-Giguère, C.-A., & Kereš, D. 2020b, MNRAS, 498, 2001, _eprint: 2003.05945

Mahler, G. et al. 2019, ApJ, 873, 96, _eprint: 1810.13439

Mainali, R. et al. 2020, MNRAS, 494, 719, _eprint: 1909.09212

——. 2018, MNRAS, 479, 1180, _eprint: 1804.00041

Malhotra, S., & Rhoads, J. E. 2006, ApJ, 647, L95, _eprint: astro-ph/0511196

Maseda, M. V. et al. 2017, A&A, 608, A4, _eprint: 1710.06432

Mason, C. A., & Gronke, M. 2020, MNRAS, 499, 1395, _eprint: 2004.13065

Mason, C. A., Naidu, R. P., Tacchella, S., & Leja, J. 2019, MNRAS, 489, 2669, _eprint: 1907.11332

Mason, C. A., Trenti, M., & Treu, T. 2015, ApJ, 813, 21, _eprint: 1508.01204

Mason, C. A. et al. 2018a, ApJ, 857, L11, _eprint: 1801.01891

Mason, C. A., Treu, T., Dijkstra, M., Mesinger, A., Trenti, M., Pentericci, L., de Barros, S., & Vanzella, E. 2018b, ApJ, 856, 2, _eprint: 1709.05356

Mason, C. A. et al. 2017, ApJ, 838, 14, _eprint: 1610.03075

Massey, R. et al. 2014, MNRAS, 439, 887, _eprint: 1401.1151

Matthee, J. et al. 2020, MNRAS, 498, 3043, _eprint: 2008.01731

——. 2019, ApJ, 881, 124, _eprint: 1903.08171

——. 2017a, ApJ, 851, 145, _eprint: 1709.06569

Matthee, J., Sobral, D., Darvish, B., Santos, S., Mobasher, B., Paulino-Afonso, A., Röttgering, H., & Alegre, L. 2017b, MNRAS, 472, 772, _eprint: 1706.06591

Matthee, J., Sobral, D., Gronke, M., Paulino-Afonso, A., Stefanon, M., & Röttgering, H. 2018, A&A, 619, A136, _eprint: 1805.11621

Mawatari, K. et al. 2020, ApJ, 889, 137, _eprint: 1912.10954

McQuinn, M., Lidz, A., Zahn, O., Dutta, S., Hernquist, L., & Zaldarriaga, M. 2007, Monthly Notices of the Royal Astronomical Society, 377, 1043

Medezinski, E., Broadhurst, T., Umetsu, K., Benítez, N., & Taylor, A. 2011, MNRAS, 414, 1840, _eprint: 1101.1955

Mellema, G. et al. 2013, Experimental Astronomy, 36, 235, 1210.0197

Meneghetti, M. et al. 2017, MNRAS, 472, 3177, _eprint: 1606.04548

Merlin, E. et al. 2016, A&A, 590, A30, _eprint: 1603.02460

——. 2015, A&A, 582, A15, _eprint: 1505.02516

Meurer, G. R., Heckman, T. M., & Calzetti, D. 1999, ApJ, 521, 64, _eprint: astro-ph/9903054

Mirocha, J., Mebane, R. H., Furlanetto, S. R., Singal, K., & Trinh, D. 2018, Monthly Notices of the Royal Astronomical Society, 478, 5591

Montes, M., & Trujillo, I. 2018, MNRAS, 474, 917, _eprint: 1710.03240

Morishita, T. et al. 2018, ApJ, 867, 150, _eprint: 1809.07604

Nakajima, K. et al. 2018, A&A, 612, A94, _eprint: 1709.03990

Nilsson, K. K., Orsi, A., Lacey, C. G., Baugh, C. M., & Thommes, E. 2007, A&A, 474, 385, 0709.0298

Oesch, P. A. et al. 2016, ApJ, 819, 129, _eprint: 1603.00461

——. 2015, ApJ, 804, L30, _eprint: 1502.05399

Oguri, M. 2010, PASJ, 62, 1017, _eprint: 1005.3103

Okabe, T. et al. 2020, MNRAS, 496, 2591, _eprint: 2005.11469

Oke, J. B. 1974, ApJS, 27, 21

Ouchi, M. et al. 2013, ApJ, 778, 102, _eprint: 1306.3572

Pacifici, C. et al. 2016, ApJ, 832, 79, _eprint: 1609.03572

Paciga, G. et al. 2013, MNRAS, 433, 639, 1301.5906

Papovich, C., Dickinson, M., & Ferguson, H. C. 2001, ApJ, 559, 620, _eprint: astro-ph/0105087

Parsa, S., Dunlop, J. S., & McLure, R. J. 2018, Monthly Notices of the Royal Astronomical Society, 474, 2904

Parsons, A. R. et al. 2010, AJ, 139, 1468, 0904.2334

Paterno-Mahler, R. et al. 2018, ApJ, 863, 154, _eprint: 1805.09834

Patil, A. H. et al. 2017, ApJ, 838, 65, 1702.08679

Pelliccia, D. et al. 2020, arXiv e-prints, arXiv:2011.08857, _eprint: 2011.08857

Pentericci, L. et al. 2018, A&A, 619, A147, _eprint: 1808.01847

——. 2014, ApJ, 793, 113, _eprint: 1403.5466

Planck Collaboration et al. 2016, A&A, 594, A1, _eprint: 1502.01582

Postman, M. et al. 2012, ApJS, 199, 25, _eprint: 1106.3328

Prevot, M. L., Lequeux, J., Maurice, E., Prevot, L., & Rocca-Volmerange, B. 1984, A&A, 132, 389

Prochaska, J. X., Hennawi, J. F., Westfall, K. B., Cooke, R. J., Wang, F., Hsyu, T., Davies, F. B., & Farina, E. P. 2020, arXiv e-prints, arXiv:2005.06505, _eprint: 2005.06505

Richard, J. et al. 2014, MNRAS, 444, 268, _eprint: 1405.3303

Richard, J., Kneib, J.-P., Ebeling, H., Stark, D. P., Egami, E., & Fiedler, A. K. 2011, MNRAS, 414, L31, _eprint: 1102.5092

Richard, J., Kneib, J.-P., Limousin, M., Edge, A., & Jullo, E. 2010, MNRAS, 402, L44, _eprint: 0910.5553

Rivera-Thorsen, T. E. et al. 2019, Science, 366, 738

Roberts-Borsani, G. W. et al. 2016, ApJ, 823, 143, _eprint: 1506.00854

Roberts-Borsani, G. W., Ellis, R. S., & Laporte, N. 2020, MNRAS, _eprint: 2002.02968

Robertson, B. E., Ellis, R. S., Furlanetto, S. R., & Dunlop, J. S. 2015, ApJ, 802, L19, _eprint: 1502.02024

Ryan, Jr., R. E. et al. 2014, ApJ, 786, L4, _eprint: 1404.0316

Salmon, B. et al. 2020, ApJ, 889, 189, _eprint: 1710.08930

——. 2018, ApJ, 864, L22, _eprint: 1801.03103

——. 2015, ApJ, 799, 183, _eprint: 1407.6012

Sanders, R. L. et al. 2020, MNRAS, 491, 1427, _eprint: 1907.00013

Santini, P. et al. 2017, ApJ, 847, 76, _eprint: 1706.07059

Sawicki, M., & Thompson, D. 2006, ApJ, 648, 299, _eprint: astro-ph/0605406

Schaerer, D., & de Barros, S. 2010, A&A, 515, A73, _eprint: 1002.1090

Schenker, M. A., Ellis, R. S., Konidaris, N. P., & Stark, D. P. 2014, ApJ, 795, 20, _eprint: 1404.4632

Schmidt, K. B. et al. 2014, ApJ, 786, 57, _eprint: 1402.4129

Schrabback, T. et al. 2007, A&A, 468, 823, _eprint: astro-ph/0606611

——. 2010, A&A, 516, A63, _eprint: 0911.0053

——. 2018, A&A, 610, A85, _eprint: 1711.00475

Senchyna, P. et al. 2017, MNRAS, 472, 2608, _eprint: 1706.00881

Shapley, A. E., Steidel, C. C., Adelberger, K. L., Dickinson, M., Giavalisco, M., & Pettini, M. 2001, ApJ, 562, 95, _eprint: astro-ph/0107324

Sharon, K. et al. 2020, ApJS, 247, 12, _eprint: 1904.05940

Shim, H., Chary, R.-R., Dickinson, M., Lin, L., Spinrad, H., Stern, D., & Yan, C.-H. 2011, ApJ, 738, 69, _eprint: 1103.4124

Shipley, H. V. et al. 2018, ApJS, 235, 14, _eprint: 1801.09734

Smit, R. et al. 2018, Nature, 553, 178, _eprint: 1706.04614

——. 2015, ApJ, 801, 122, _eprint: 1412.0663

——. 2014, ApJ, 784, 58, _eprint: 1307.5847

Sobral, D., & Matthee, J. 2019, A&A, 623, A157, _eprint: 1803.08923

Sobral, D., Matthee, J., Darvish, B., Schaerer, D., Mobasher, B., Röttgering, H. J. A., Santos, S., & Hemmati, S. 2015, ApJ, 808, 139, _eprint: 1504.01734

Sobral, D. et al. 2018, Monthly Notices of the Royal Astronomical Society, 477, 2817

Soucail, G. 1987, The Messenger, 48, 43

Stark, D. P. 2016, Annual Review of Astronomy and Astrophysics, 54, 761

Stark, D. P. et al. 2017, MNRAS, 464, 469, _eprint: 1606.01304

Stark, D. P., Ellis, R. S., Chiu, K., Ouchi, M., & Bunker, A. 2010, MNRAS, 408, 1628

Stark, D. P., Schenker, M. A., Ellis, R., Robertson, B., McLure, R., & Dunlop, J. 2013, ApJ, 763, 129, _eprint: 1208.3529

Stefanon, M. et al. 2019, arXiv e-prints, _eprint: 1902.10713

Steidel, C. C., Giavalisco, M., Pettini, M., Dickinson, M., & Adelberger, K. L. 1996, The Astrophysical Journal Letters, 462, L17

Strait, V. et al. 2020a, arXiv e-prints, arXiv:2009.00020, _eprint: 2009.00020

——. 2018, The Astrophysical Journal, 868, 129, arXiv: 1805.08789

——. 2020b, The Astrophysical Journal, 888, 124

Tachibana, Y., & Miller, A. A. 2018, PASP, 130, 128001, _eprint: 1902.01935

Tamura, Y. et al. 2019, The Astrophysical Journal, 874, 27

Tang, M., Stark, D. P., Chevallard, J., & Charlot, S. 2019, Monthly Notices of the Royal Astronomical Society, 489, 2572

Tilvi, V. et al. 2020, ApJ, 891, L10, _eprint: 2001.00873

Tolstoy, E., Hill, V., & Tosi, M. 2009, Annual Review of Astronomy and Astrophysics, 47, 371

Totani, T., Aoki, K., Hattori, T., & Kawai, N. 2016, PASJ, 68, 15, 1508.05067

Trenti, M. et al. 2011, ApJ, 727, L39, _eprint: 1011.4075

Treu, T. et al. 2015, ApJ, 812, 114, _eprint: 1509.00475

Treu, T., Schmidt, K. B., Trenti, M., Bradley, L. D., & Stiavelli, M. 2013, ApJ, 775, L29, _eprint: 1308.5985

Umetsu, K., Broadhurst, T., Zitrin, A., Medezinski, E., & Hsu, L.-Y. 2011, ApJ, 729, 127, _eprint: 1011.3044

Vanzella, E. et al. 2020, MNRAS, 491, 1093, _eprint: 1904.07941

——. 2016, The Astrophysical Journal, 825, 41

Verhamme, A., Orlitová, I., Schaerer, D., & Hayes, M. 2015, A&A, 578, A7, _eprint: 1404.2958

Vulcani, B. et al. 2016, ApJ, 833, 178, _eprint: 1610.04621

Wang, B., Heckman, T. M., Leitherer, C., Alexandroff, R., Borthakur, S., & Overzier, R. A. 2019, The Astrophysical Journal, 885, 57

Wang, F. et al. 2020, ApJ, 896, 23, 2004.10877

Wang, X. et al. 2015, ApJ, 811, 29, _eprint: 1504.02405

Weinberger, L. H., Kulkarni, G., Haehnelt, M. G., Choudhury, T. R., & Puchwein, E. 2018, Monthly Notices of the Royal Astronomical Society, 479, 2564

Weisz, D. R., Dolphin, A. E., Skillman, E. D., Holtzman, J., Gilbert, K. M., Dalcanton, J. J., & Williams, B. F. 2014, The Astrophysical Journal, 789, 148

Whitaker, K. E. et al. 2011, ApJ, 735, 86, _eprint: 1105.4609

Willott, C. J., Carilli, C. L., Wagg, J., & Wang, R. 2015, ApJ, 807, 180, _eprint: 1504.05875

Yan, H. et al. 2005, ApJ, 634, 109, _eprint: astro-ph/0507673

Yang, L., Birrer, S., & Treu, T. 2020, MNRAS, 496, 2648, _eprint: 2001.07719

Zheng, W. et al. 2012, Nature, 489, 406, _eprint: 1204.2305

Zheng, Z.-Y. et al. 2019, PASP, 131, 074502, 1903.09045

Zitrin, A., Broadhurst, T., Bartelmann, M., Rephaeli, Y., Oguri, M., Benítez, N., Hao, J., & Umetsu, K. 2012, MNRAS, 423, 2308, _eprint: 1105.2295

Zitrin, A. et al. 2015, ApJ, 801, 44, _eprint: 1411.1414

——. 2013, ApJ, 762, L30, _eprint: 1211.2797

——. 2017, ApJ, 839, L11, _eprint: 1702.05090